

INVITATION

to the defense of my thesis

January 18th, 2010
16.15 pm

Academiegebouw
Domplein 29, Utrecht

Ahmet Faik Demirörs

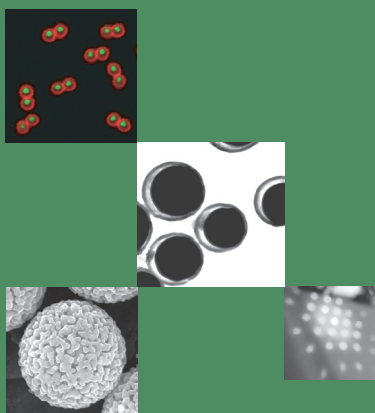
a.f.demirors@uu.nl
0628207065

Reception to follow in
Lokaal de Reunie
't Wed 3a

Paranimfs

Johan Stiefelhagen
j.c.p.stiefelhagen@gmail.com

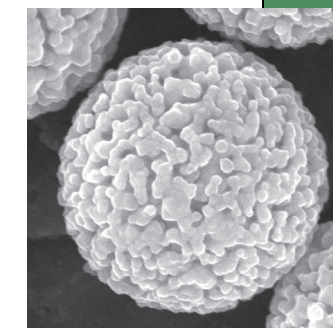
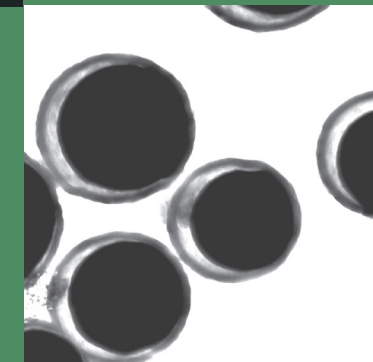
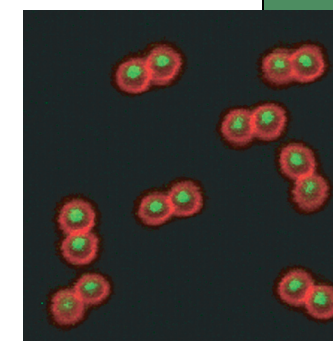
Menduh Hasdemir
menduh@hasdemir.nl



There is a growing interest in the fabrication of anisotropic colloids made by using colloidal spheres, recently, because it may lead to a better control over a wide range of materials properties. The research described in this thesis focuses on synthesis and phase behavior of anisotropic colloids prepared through different synthetic strategies. Namely, eccentric core-shell particles, dimers, string-like particles and core-shell particles are systems investigated throughout this book. The synthesis routes are described for these colloidal systems and their physical/chemical properties are extensively characterized. Furthermore, potential applications of these colloidal systems in fields such as size-selective catalysis, colloidal crystallization, optical tweezing are investigated. One important aspect in this thesis is the combination of soft interactions with the anisotropy of the colloid. This results in a system in which the rotational order of particles can be controlled, and which may find interesting applications.

Universal Press

ANISOTROPIC COLLOIDS: SYNTHESIS AND PHASE BEHAVIOR OF ECCENTRIC, DIMER AND STRING-LIKE COLLOIDS



AHMET FAİK DEMİRÖRS

ANISOTROPIC COLLOIDS: SYNTHESIS AND PHASE BEHAVIOR OF ECCENTRIC, DIMER AND STRING-LIKE COLLOIDS AHMET F. DEMİRÖRS 2010

Anisotropic Colloids:

Synthesis and Phase Behavior of Eccentric,
Dimer and String-like Colloids



Universiteit Utrecht

A digital (color) version of this thesis is available at [http:// www. colloid. nl](http://www.colloid.nl)

Anisotropic Colloids:

**Synthesis and Phase Behavior of Eccentric,
Dimer and String-like Colloids**

Anisotrope Colloïden:

**Synthese en Fasegedrag van Excentrische, Dimere en
Ketenvormige Colloïden**

(met een samenvatting in het Nederlands)

Proefschrift

ter verkrijging van de graad van doctor aan de Universiteit Utrecht
op gezag van de rector magnificus, prof.dr. J.C. Stoof, ingevolge het
besluit van het college voor promoties in het openbaar te verdedigen op

maandag 18 Januari 2010 des middags te 4.15 uur

door

Ahmet Faik Demirörs

geboren op 20 mei 1981 te Kulu, Turkije

Promotor: Prof. dr. A. van Blaaderen
Co-promotor: Dr. A. Imhof

"Annem'le Babama..."

Contents

1	Introduction	1
1.1	Colloids?	2
1.2	Anisotropic Colloids and Colloidal Molecules	2
1.3	This Thesis	4
	References	5
2	Synthesis of Eccentric Titania-Silica Core-Shell and Composite Particles	7
2.1	Introduction	8
2.2	Experimental details	9
2.3	Results and discussion	10
2.4	Conclusions & outlook	17
	References	19
3	BaTiO₃, SrTiO₃, CaTiO₃ and Ba_xSr_{1-x}TiO₃ particles: A General Approach for Colloidal Perovskites	23
3.1	Introduction	24
3.2	Experimental details	25
3.3	Results and discussion	26
3.4	Conclusions & outlook	35
	References	37
4	Anatase Core, Titania Shell Colloidal Particles for Optical Tweezing	39
4.1	Introduction	40
4.2	Experimental details	41
4.3	Results and discussion	43
4.3.1	<i>Synthesis and Characterization</i>	43
4.3.2	<i>Particles as Tools for Optical Tweezing</i>	49
4.4	Conclusions & outlook	50
	References	52
5	A General Method to Coat Colloidal Particles with Titania	55
5.1	Introduction	56
5.2	Experimental details	57
5.3	Results and discussion	60
5.4	Conclusions & outlook	66
	References	68
6	Soft Colloidal Dumbbells and Switching of Their Solid States	71
6.1	Introduction	72

6.2	Experimental details	75
6.3	Results and discussion	76
6.3.1	<i>Laser diffraction of soft dumbbell solids</i>	84
6.4	Conclusions & outlook	85
	References	87
7	Phase Behavior of Colloidal Dumbbells in an Electric Field	89
7.1	Introduction	90
7.2	Experimental details	92
7.3	Results and discussion	93
7.4	Conclusions & outlook	103
	References	105
8	Chains of Colloidal Beads	109
8.1	Introduction	110
8.2	Experimental details	112
8.3	Results and discussion	114
8.3.1	<i>Chains of Emulsion Droplets</i>	114
8.3.2	<i>Chains of Silica Particles</i>	119
8.3.3	<i>Chains of PS Particles</i>	119
8.4	Conclusions & outlook	120
	References	121
	Selected Figures in Color	123
	Summary	126
	Samenvatting	128
	Acknowledgement	130
	Curriculum Vitae	132
	List of Publications	133

1

Introduction

In this introductory chapter we describe what colloids are and what are their possible applications in colloidal and materials science. Anisotropic colloidal particles are defined and their functional advantages and fundamental importance as model systems with respect to isotropic particles is discussed. We also give an outline of our experimental work described throughout the thesis. A more specialized introduction to each of the different topics can be found in the separate chapters.

1.1 Colloids?

Colloids are generally defined as particles dispersed in a solvent, which have at least in one direction a dimension between 1 nm and 1 μm . Colloids are small compared to macroscopic objects but they are also large when compared with atoms and molecules. A characteristic property of particles in this size range is that they undergo Brownian motion as a consequence of the size-range difference of the colloids and the size-range of the dispersing atomic or molecular medium. A colloid is constantly banged by solvent molecules, however at an instant the number of collisions is in general not completely equal from all sides, which leads to a net momentum transfer to the particle that is significant for a particle of colloidal size to translate. Displacements due to Brownian motion are only of a short range and the fluctuations in collisions with fluid-molecules are completely uncorrelated such that the net trajectory of the particle is a "random walk". As a result of Brownian motion, colloids exhibit similar phase behavior to atoms and molecules, but their length-scale offers important advantages: direct visualization by optical microscopy, tunability of interactions and slowness of diffusion make colloids ideal tools and model systems for fundamental investigations [1]. Colloids, which offer the possibility of physico-chemical manipulations by modifying the properties of the colloid (e.g. surface modification of the colloids) or the suspended medium (e.g. refractive index matching, density matching and adjusting the interactions by changing solvent properties), also offer ways of manipulation by external forces (e.g. electrical, magnetic, centrifugal), which find use in separation technology, in electrorheological and magnetorheological fluids with industrial applications as hydraulic valves, clutches, brakes [2] and displays [6].

Optical microscopy for colloid science is a very powerful technique, as it gives a direct visualization of the local structure including aspects like defects and dislocations that are only visible in an averaged way in scattering techniques. For molecular systems direct observation of a molecular length-scale is possible with for instance atomic force microscopy (AFM) or scanning tunneling microscopy (STM), but this is experimentally much more difficult and expensive. Furthermore, techniques like AFM and STM only probe surface structure, while with various light microscopy techniques it is possible to acquire quantitative 3D data on colloidal systems [7–9].

1.2 Anisotropic Colloids and Colloidal Molecules

To date, most studies of colloids have used spherical particles or particles with simple shapes, such as rods and plates. Phase behavior of spheres is well established computationally and experimentally, such that they form face-centered-cubic (fcc) crystals, when assembled. Phase behavior of rods and plates are also well established both experimentally and theoretically. Rods and plates are known

to form liquid crystals and they may exhibit isotropic, nematic, smectic or crystalline phases depending on the volume fraction and polydispersity of the system [3–5]. It is now known that the functional use of *fcc* crystals of spheres is limited for materials science, for example from photonics point of view and it is hypothesized that non-spherical and anisotropic building blocks may lead to better optical properties [10]. For extending the spectrum of colloidal particles, considerable effort has been devoted to the design and controlled fabrication of colloidal particles with complex shapes in recent years. The interest in colloids with complex shapes and functionality for materials stems from the fact that the optical, electrical, and chemical properties that vary with size, composition, structural order and "patchyness". All these properties are attractive with many functional properties for materials science. Van Blaaderen recently introduced the term of "colloidal molecules", [11] which makes analogy to the atomic structures as colloidal spheres resembling atoms and super structures of the colloids to be "molecules". These colloidal molecules are important as a model system for exploring the phase behavior of their molecular counterparts. The first experimental results for "colloidal molecules" was the work of Manoharan et al. [12], where they used the evaporation of emulsion droplets, encapsulating the particles, to assemble the spheres into molecule-like structures. This was followed by the work of Johnson et al. [13] where emphasis was only on the "colloidal dumbbells" with higher particle yields. Here the term dumbbell stands for overlapped dimer particles with aspect ratios equal or smaller than that of two touching spheres. Inspiring experimental work done in recent years including "ellipsoids", "ice-cream cone" structures, "patchy particles" and "Janus" particles was summarized in a review by Yang et al. [14]. One notable recent work by Ravaine et al. introduced "binary colloidal molecules" similar to binuclear molecules such as BeCl_2 , BF_3 , CH_4 and PCl_5 from oppositely charged particles [15]. Furthermore the principle of Manoharan et al. extended to many type of particles like titania, PS, silica and also for binary particles of different sizes, which yielded a very rich family of anisotropic structures [16]. The yield of these syntheses are not yet high enough for studying self assembly but these particles with different surface properties at different "patches" are certainly very interesting for directed self assembly processes.

Complex colloids with anisotropic properties are desirable for many fields, including sensors [17] and photonic band gap materials [18, 19]. Anisotropic particles are mostly produced by using spherical colloids as for dumbbells [13, 20–24], ellipsoids [19], colloidal molecules and clusters of particles [12, 16]. One recent and notable work reported synthesis of patchy particles by using spherical colloids with surface modification in a dry colloid crystal state [25]. In this method colloidal crystals were calcined after drying such that the particles physically touch each other. Then the dry crystal was surface modified where modification only took place on particle surfaces with no contact to other particles. Further particle growth took place only at the points where particles were touching inside the crystal, yielding particles with nodules. Although numbers of patches here is re-

stricted with the number of surrounding colloids, which is 12 for *fcc* phase, smart ways of decreasing this number may be found in the future.

1.3 This Thesis

The work presented in this thesis focuses on the preparation of colloidal particles with the aim of achieving new routes of synthesis for functional colloidal particles as well as phase behavior, applications and characterizations of these particles. A significant part of the colloids fabricated within this work has symmetries different than of a sphere and are so called anisotropic. In chapter 2 we describe a new route to synthesize eccentric core-shell particles of titania-core and silica shell, where the core is located not in the center of the particles but eccentrically. We describe possible applications of these particles and also present the mechanism of the particle formation, which also opens a way of synthesizing composite particles. Based on the findings and understanding of chapter 2 we hypothesize that the composite particle synthesis is a general method for making titania based composite particles. We explore this hypothesis in chapter 3, where we describe a general method for fabricating colloidal perovskites based on titania particles. In chapter 4 synthesis of colloidal titania with core-shell morphology with a crystalline-titania core and amorphous-titania shell is presented. This provides tunability of the refractive index over a wide range. The superior optical tweezing properties of these specially designed spheres are discussed. Based on the knowledge we obtained from the titania coating procedure in chapter 4 we found a new general route for coating colloidal particles with a titania shell, which we describe in chapter 5. In chapter 6 we turn back to anisotropic particles where we explore the self-assembly of colloidal silica dumbbells with soft particle interactions. Colloidal dumbbells with soft interactions exhibit a plastic solid phase, which was predicted computationally but was not shown for a three-dimensional colloidal system, experimentally. We investigate the behavior of soft plastic solids with or without applying an external electric field. In chapter 7 we present the phase behavior of colloidal dumbbells with different aspect ratios and an external electric field to direct their assembly. New crystal phases of colloidal dumbbells are found, which could have interesting photonic applications. In chapter 8 we present our preliminary work for fabricating highly anisotropic colloidal particles by stringing particles together with an electric field and permanently sticking them with an extra layer of silica or titania into a "chain of beads".

References

- [1] Vrij, A.; Tuinier, R.; Structure of concentrated colloidal dispersions. In J. Lyklema, editor, *Fundamentals of Interface and Colloid Science*, volume IV, pages 5.1-5.103. Elsevier, Amsterdam, 2005.
- [2] Parthasarathy, M.; Klingenberg, D. *Mater. Sci. Eng.*, **1996** R. 17, 57.
- [3] Bolhuis, P.; Frenkel D. *J. Chem. Phys.*, **1997**, 106, 666.
- [4] Bates, M. A.; Frenkel D. *J. Chem. Phys.*, **2000**, 112, 10034.
- [5] van der Kooij F. M., Kassapidou K., Lekkerkerker H. N. W. *Nature*, **2000**, 406, 868.
- [6] Wen, W. J.; Weisbuch, C.; Phuong, D. M.; Lu, G.; Ge, W.; Chan, C. T.; Sheng, P. *Nanotechnology*, **2005**, 16, 598.
- [7] van Blaaderen, A. *Prog. in Colloid Polym. Sci.*, **1997**, 104, 59.
- [8] Dinsmore, A. D.; Weeks, E. R.; Prasad, V.; Levitt, A. C.; Weitz, D. A. *Appl. Optics* , **2001**, 40, 4152.
- [9] Elliot, M. S.; Poon, W. C. K. *Adv. Colloid Interface Sci.*, **2001**, 92, 133.
- [10] Li, Z. Y.; Wang, J.; Gu, B. Y. *J. Phys. Soc. of Jpn*, **1998**, 67, 9, 3288.
- [11] van Blaaderen, A. *Science*, **2003**, 301, 470.
- [12] Manoharan, V. N.; Elsesser, M. T.; Pine, D. J. *Science*, **2003**, 301, 483.
- [13] Johnson, P. M.; van Kats, C. M.; van Blaaderen, A. *Langmuir*, **2005**, 21, 11510.
- [14] Yang, S. M.; Kim, S. H.; Lima, J. M.; Yi, G. R. *J. Mater. Chem.*, **2008**, 18, 2177.
- [15] Perro, A.; Duguet, E.; Lambert, O.; Taveau, J. C.; Bourgeat-Lami, E.; Ravaine, S. *Angew. Chem. Int. Ed.*, **2009**, 48, 361.
- [16] Cho, Y. S. et al. *J. Am. Chem. Soc.*, **2005**, 127, 15968.
- [17] Perez, J. M.; Simeone, F. J.; Saeki, Y.; Josephson, L.; Weissleder, R. *J. Am. Chem. Soc.*, **2003**, 125, 10192.
- [18] van Blaaderen, A. *Nature*, **2006**, 439, 545.
- [19] Lu, Y.; Yin, Y. D.; Xia, Y. N. *Adv. Mater.* **2001**, 13, 415.
- [20] Skjeltorp, A. T.; Ugelstad, J.; Ellingsen, T. *J. Colloid Interface Sci.*, **1986**, 113, 577.
- [21] Sheu, H. R.; El-Aasser, M. S.; Vanderhoff, J. W. *J. Polym. Sci. Part A*, **1990**, 28, 653.
- [22] Kim, J. W.; Larsen, R. J.; Weitz, D. A. *J. Am. Chem. Soc.*, **2006**, 128, 14374.
- [23] Mock, E. B.; DeBruyn, H.; Hawke, B. S.; Gilbert, R. G.; Zukoski, C. F.; *Langmuir*, **2006**, 22, 4037.
- [24] Lu, Y.; Xiong, H.; Jiang, X. C.; Xia, Y. N.; Prentiss, M.; Whitesides, G. M. *J. Am. Chem. Soc.*, **2003**, 125, 12724.
- [25] Wang, L.; Xia, L.; Li, G.; Ravaine, S.; Zhao, X. S. *Angew. Chem. Int. Ed.*, **2008**, 47, 4725.

2

Synthesis of Eccentric Titania-Silica Core-Shell and Composite Particles

We describe a novel method to synthesize colloidal particles with an eccentric core-shell structure. Titania-silica core-shell particles were synthesized by silica coating of porous titania particles under Stöber [1] conditions. We can control access of silica to the pores in the titania, allowing us to produce either core-shell or composite particles. Calcination of the core-shell particles gives unique eccentric core-shell structures, due to extensive shrinkage of the highly porous titania core with respect to the silica shell. However, when the titania particles are silica treated prior to drying they result in composite titania-silica spheres, where two materials are mixed uniformly. These spheres are interesting for catalysis, (switchable) photonic crystal applications, optical tweezing and new titania based materials. We demonstrate photocatalytic activity of the eccentric spheres where the silica layer acts as a size selective membrane.

2.1 Introduction

The fabrication of functional hollow colloidal particles is of great scientific and technological interest with a wide range of applications, including drug delivery, coatings, photonic devices, and nanoscale reaction vessels [2–8]. Various methods, including approaches such as spray drying [9], emulsion templating techniques [10, 11], and self assembly processes [12] have been described to prepare hollow spheres out of latex, metal and inorganic materials [13–18]. Recently, much research has been undertaken to functionalize the interior of the hollow spheres by encapsulation of metal nanoparticles [19–23]. Such an approach leads to the fabrication of unique catalytic systems. In particular Arnal et al. [13] and Lee et al. [24] have shown that 'rattle-like' core-shell particles have a much better catalytic performance compared to metal nanoparticles supported on the same material without a void in between. It was found that in the case of eccentric core-shell particles, the core is effectively separated from other particles and also accessible to the gas molecules whereas in the no-void case mass transfer is limited within the microporous structure of the shell due to touching solid-solid interfaces. Eccentric particles also have the advantage of easier heat treatment without causing any aggregation of the encapsulated ingredient even under harsh reaction conditions. This feasibly leads to high catalytic activity because aggregation, usually caused by coalescence of the particles or Ostwald ripening, is known to result in loss of catalytic activity [25].

Hollow particles equipped with functional microparticles also offer an opportunity for size-selective catalysis. Ikeda et al. demonstrated that titania encapsulated by a silica shell can be used for size-selective photocatalytic decomposition of organics [26, 27]. The pore sizes in the silica shell determines the size selectivity: molecules larger than the silica pore size are filtered out and not catalyzed while smaller molecules are. This approach may lead to important applications combined with the knowledge that the silica pore size can be finely tuned from mesoporous (2-50 nm) to microporous (< 2 nm) by modifying the synthesis conditions of silica [28, 29].

Monodisperse eccentric particles with movable cores have been suggested for photonic crystals tunable by an external field [30]. Such particles due to their monodisperse spherical outer shell can form ordered crystals but because of the random distribution of the core particles will not have a photonic band gap. Camargo et al. [30] demonstrated by computation that an external field that aligns particles along field lines can cause a band gap to open due to the induced long range order. This approach brings also the chance of tuning the gap position by changing an external field strength [31].

Reports for the preparation of eccentric particles are mostly based on successive two step coating of the core particle and sacrificial removal of the middle shell [8, 13, 30, 32]. Here we report a novel and shorter way of fabricating eccentric core-shell particles by taking advantage of porous titania particles that upon

sintering shrink much more than the silica shell enclosing them. We also show that control over the access of silica to the pores can be used to produce either core-shell or composite particles. We believe that our approach constitutes a new way of manipulating the morphology of composite particles and can be used to synthesize new types of composite particles based on titania.

2.2 Experimental details

Particles

Synthesis of the titania particles was done according to the procedure of Eiden-Assmann et al. [33]. In a typical synthesis 250 ml ethanol with 17.0 ml $\text{Ti}(\text{OC}_2\text{H}_5)_4$ was mixed with 750 ml of ethanol with 4.0 ml of 0.1 M aqueous Lutensol ON50 (BASF) solution. This gives monodisperse titania particles with a size between 900-1200 nm depending on the reaction temperature and the amount of the titania precursor. The titania particles are then collected by centrifugation.

After being dried in an oven at 50 °C for 2 hours the particles are coated with silica under Stöber conditions. Typically 0.082 g of titania was dispersed in 50 ml of ethanol and 0.55 ml of ammonia was added to the dispersion. It was followed by 0.8 ml of tetraethoxysilane (TEOS) and, if desired, a suitable amount of [3-aminopropyl]trimethoxysilane (APS) coupled to rhodamine isothiocyanate (RITC) for fluorescent labeling the silica (0.02 g APS and 0.005 RITC for 1 ml of TEOS) [34]. The particles were then coated with extra silica (without dye) in 100 ml ethanol with 5 ml of ammonia and 2 ml of TEOS. Silica coating of the dried titania results in *cs*- $\text{TiO}_2@SiO_2$ particles. Upon calcination at 600-625 °C for 15-60 minutes the *cs*- $\text{TiO}_2@SiO_2$ particles gives rise to *ecc*- $\text{TiO}_2@SiO_2$ particles. Exactly the same procedure, except for the drying step at 50 °C was followed to produce the *comp*- $\text{TiO}_2@SiO_2$ particles.

Static Light Scattering

Static Light Scattering was performed with home-built equipment using a He-Ne laser as a light source (632.8 nm, 10 mW). The logarithm of scattering intensity data were plotted against the scattering vector $k=4\pi n\sin(\theta/2)/\lambda$, where n is the solvent refractive index, θ is the scattering angle, and λ the wavelength in vacuum.

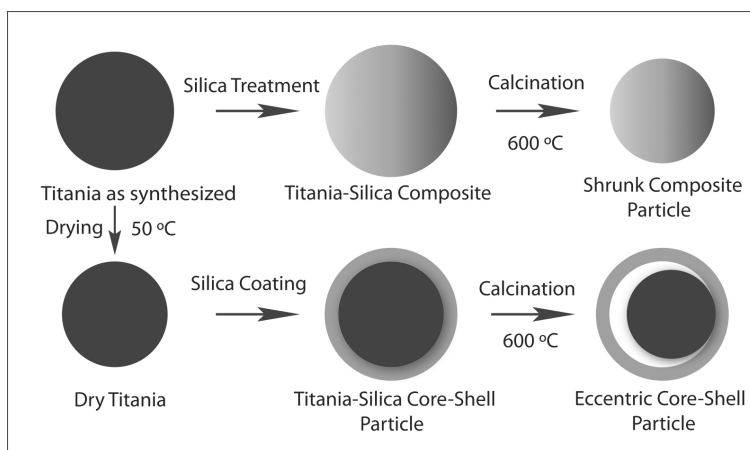
X-ray Diffraction

The powder XRD measurements were performed with a Philips PW 1820 diffractometer with a Philips PW 1729 X-ray generator (Cu K_α radiation). In the photocatalysis experiments a 6W Hg UV lamp with a wavelength of 251 nm was used. Uncapped scintillation vials were used with 15 mg of titania dispersed in 10 ml

of aqueous solution containing 0.61 μmol Methylene Blue (MB), 0.34 μmol RITC or 0.20 μmol RITC in RITC-PAH sample. RITC was coupled to poly(allylamine hydro-chloride) (PAH) according to the procedure of Donath et al. [35].

2.3 Results and discussion

The route for the fabrication of composite ($\text{comp-TiO}_2@SiO_2$), core-shell ($\text{cs-TiO}_2@SiO_2$) and eccentric core-shell ($\text{ecc-TiO}_2@SiO_2$) titania-silica particles is given in Scheme 1. After being dried in an oven at 50 $^\circ\text{C}$ for 2 hours titania particles can be coated with silica under Stöber conditions [1]. We also couple the fluorescent dye rhodamine isothiocyanate (RITC) to silica [34]. Silica coating of the dried titania results in $\text{cs-TiO}_2@SiO_2$ particles. Upon calcination at 600-625 $^\circ\text{C}$ for 15-60 minutes the titania cores of $\text{cs-TiO}_2@SiO_2$ particles shrink more due to higher porosity of the titania compared to silica giving rise to $\text{ecc-TiO}_2@SiO_2$ particles. On the other hand, it was observed that the titania particles are very sensitive to the drying step. If the drying step was omitted the as-synthesized particles upon silica treatment form homogeneously mixed $\text{comp-TiO}_2@SiO_2$ particles.



Scheme 2.1. Schematic representation of the procedure for fabrication of $\text{comp-TiO}_2@SiO_2$, $\text{cs-TiO}_2@SiO_2$ and $\text{ecc-TiO}_2@SiO_2$ particles.

The striking influence of the drying step can be appreciated by comparing the confocal fluorescence microscopy images. For the $\text{cs-TiO}_2@SiO_2$ particles we observe a ring-like structure which demonstrates the core-shell structure of the particle where only the fluorescently labeled silica coating is visible in Fig. 2.1a. However, in the case of $\text{comp-TiO}_2@SiO_2$ particles in Fig. 2.1b the image shows a fully dyed structure, which means that RITC dye (coupled to silica) is dispersed throughout the particle on a nm scale. The insets show line profiles on a single particle and show the properties of core-shell and fully dyed structures.

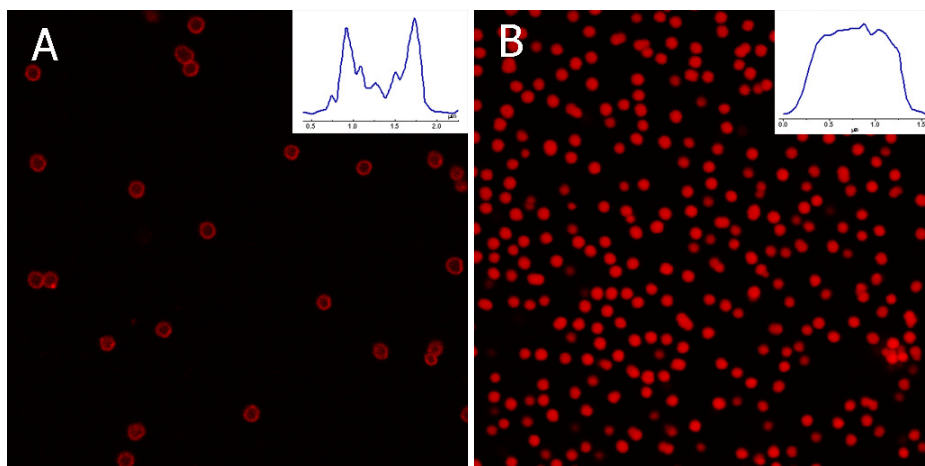


Figure 2.1: Confocal fluorescence microscopy images of titania-silica particles, (a) $cs\text{-TiO}_2@SiO_2$ produced by drying in an oven for 2 hours at 50 °C followed by silica coating (image size 37.5 $\mu\text{m} \times 37.5 \mu\text{m}$), (b) the same titania particles without drying which forms $comp\text{-TiO}_2@SiO_2$ particles upon silica treatment. Insets are line profiles through single particles. (image size 47.25 $\mu\text{m} \times 47.25 \mu\text{m}$).

A TEM micrograph of the bare titania particles is given in Fig. 2.2a. The $ecc\text{-TiO}_2@SiO_2$ particles shown in Fig. 2.2b were synthesized by taking advantage of the high porosity of the core titania particles. The core titania particles shrunk upon calcination and formed $ecc\text{-TiO}_2@SiO_2$ particles. For the case shown in Fig. 2.2b we found the size of the eccentric particles to be 850 nm (5% polydispersity) and the shell thickness to be 70 nm, where the inner core was 630 nm. The void between the shrunk core and the silica shell was around 40-120 nm depending on the particle size and the calcination time.

As further support for our interpretation of the particle structure we performed Energy Dispersive X-Ray (EDX) analysis for the $comp\text{-TiO}_2@SiO_2$ and $ecc\text{-TiO}_2@SiO_2$ particles. Fig. 2.3a shows the EDX line graph of a $comp\text{-TiO}_2@SiO_2$ particle obtained in STEM mode by performing the scan shown in Fig. 2.3b. It is observed that both the silicon and titanium peaks start at the same radial position and have the same profile across the particle, which corresponds to that of a spherical object. This verifies that silica is dispersed throughout the particle homogeneously. In the case of $ecc\text{-TiO}_2@SiO_2$ particles the EDX line graph in Fig. 2.3c clearly demonstrates the eccentric core-shell structure with silicon showing the characteristic shell peaks on the ends.[36] Note that titanium shows up after silicon and exists only in the inner part of the particle. Importantly, there is a 45 nm gap between the silicon peak and the point where titanium ends, which is due to the space between the titania core and the silica shell.

Silica coating of the particles increases their size, as for dried titania the silica only coats the surface of the particle and thus particle growth is mainly on the

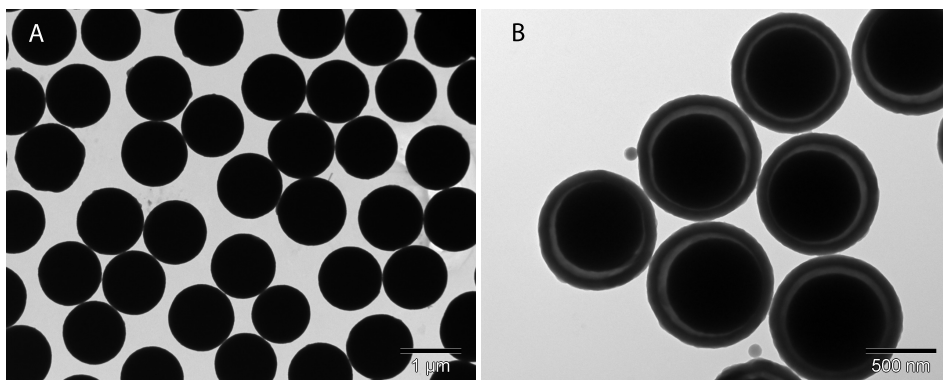


Figure 2.2: The TEM images of the titania particles (a) titania particles as synthesized, (b) eccentric titania-silica core-shell particles after calcination.

surface. However, we observed larger particle sizes ($1.3 \mu\text{m}$) for the silica treated particles without drying compared to dried ones ($1.1 \mu\text{m}$ where bare particle were $1.0 \mu\text{m}$), although we otherwise applied the same treatment to both batches. We believe that prior to drying the particles are in a swollen state and, upon silica treatment, are filled with the added silica. In other words, the swollen particles upon drying shrink to a less porous state, but silica filling of the pores prevents this shrinkage. The dried particles shrink further upon calcination due to the still high porosity of the particles with a specific surface area of $300 \text{ m}^2/\text{g}$ [33]. We have shown the large effect of drying and sintering on the titania particles size by Static Light scattering (SLS).

Fig. 2.4 shows the data compared to the Mie scattering calculations for a uniform sphere [37]. The locations of the minima and maxima on the k -axis depend sensitively on the particle size and refractive index, whereas the depth of the minima gives an estimate of the polydispersity [38]. Curve *a* in Fig. 2.4 is the SLS curve for the as-synthesized titania particles fitted to the full Mie solutions of the form factor with radius and refractive index of 900 nm and 1.63 respectively. The SLS curves *b* and *c* belong to the dried and $650 \text{ }^\circ\text{C}$ sintered titania (bare) particles. The Mie fitting for these samples give 675 nm and 525 nm for radius and 1.8 [39] and 2.3 for the refractive indices respectively. The SLS curves clearly show the extensive shrinkage of the particle through the drying and calcination steps even by mere inspection of the number of the minima in the curves, which decreases from 7 ($1.8 \mu\text{m}$, as synthesized) to 6 ($1.35 \mu\text{m}$, dried) to 4 ($1.05 \mu\text{m}$, calcined). The large size difference between the non-dried and dried particles explains why we get two different types of particles upon silica treatment. Titania particles as-synthesized have a tenuous structure and not fully condensed, so before drying they clearly have a very open network which is accessible to the silica precursors (even to silica oligomers). We expect that due to this property the non-

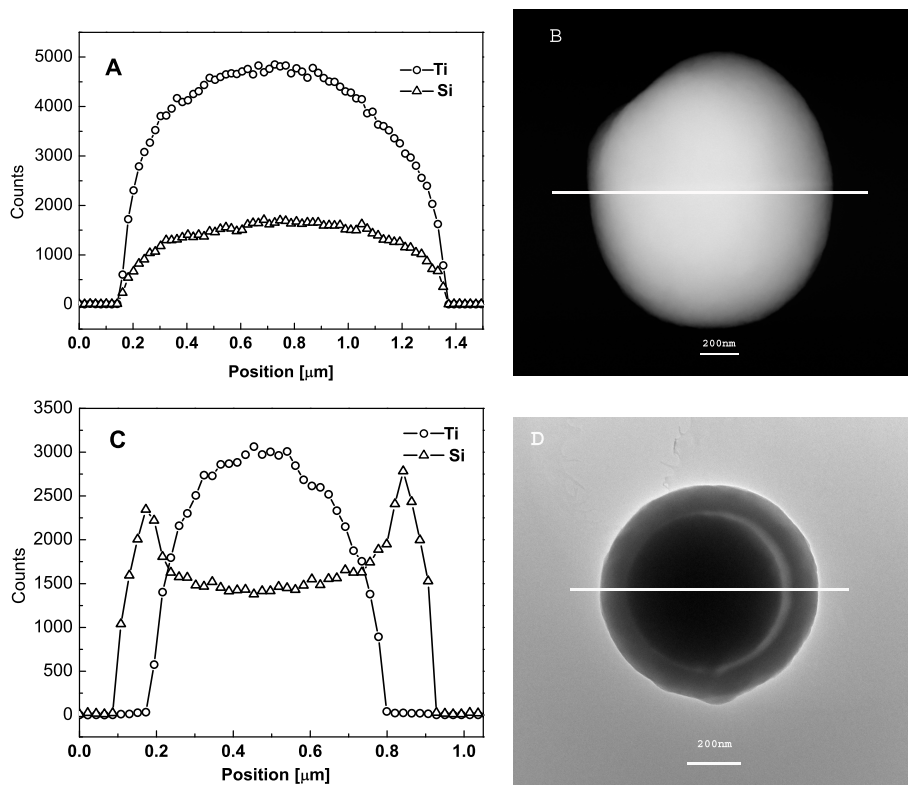


Figure 2.3: (a) EDX line graph of a composite titania-silica particle obtained in STEM mode by performing the scan shown in b, (b) TEM dark-field image showing the EDX line-scan through the composite particle (Scan was performed from left to right). (c) EDX line graph of an eccentric titania-silica core-shell particle obtained in STEM mode by performing the scan shown in d, (d) TEM image showing the EDX line-scan through the eccentric core-shell particle.

dried particles are accessible to many types of chemicals, which opens a way to synthesize mixed composite particles by adding other precursors. On the other hand, drying closes up the titania network and densifies the matrix, such that silica can no longer penetrate into the particles but accumulates on their surfaces.

Amorphous titania synthesized with the sol-gel method is known to exhibit phase transitions upon heating. X-ray diffraction (XRD, Fig. 2.5) measurements show that the particles become anatase in crystal structure even upon short heat treatments, like 15-20 minutes at 600 °C. The structure turns to rutile upon longer calcinations at 1000 °C. The crystallite size of the samples was estimated with the Debye-Scherrer equation $t = 0.9 \lambda / B \cos \theta_B$ where t is the average size of the crystalline domains, λ is the wavelength of the X-ray source, 1.5403 Å, B is the Full Width Half Maximum of the XRD line in radians and θ_B is half the

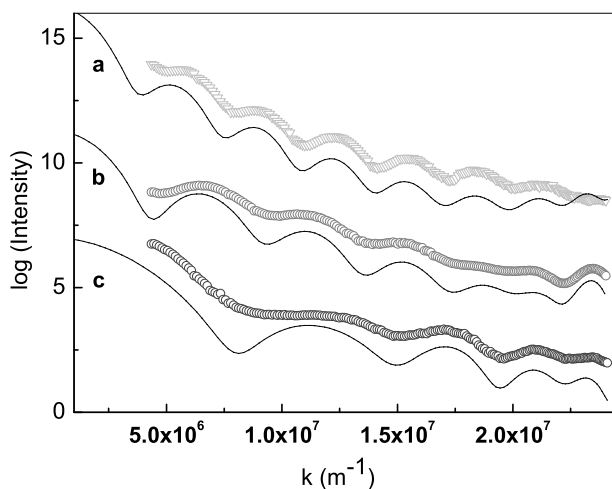


Figure 2.4: SLS experimental curves of the titania particles (symbols) in ethanol fitted to theoretical calculations of the full Mie solutions to the form factor (lines, offset for clarity) (a) titania particles as synthesized, radius 900 nm, refractive index 1.63, (b) titania particles after drying, radius 675 nm, refractive index 1.8, (c) titania particles after calcination at 650 °C, radius 525 nm, refractive index 2.3, all curves are fitted for 4 % polydispersity (k = scattering vector).

angle of the XRD peak. The composite particles had a significantly smaller crystallite size than core-shell particles. Apparently, the presence of silica in the pores of the titania prevents crystallite domain growth. This also suggests that silica is well dispersed in the particle at the nm level. We found a crystallite size for the core-shell particles of 5 nm after 25 minutes of calcination at 620 °C and 3 nm for the composite particles after 60 minutes of calcination at the same temperature. Considering that crystallite size increases with calcination time, this difference is significant. When the calcination time was increased to 12 hours, the crystallite sizes grew to 9 nm and 5 nm for core-shell and composite particles, respectively.

The crystallite size for bare titania grew even faster, after calcination at 620 °C for 25 minutes a size of 11 nm was found. We think that this difference is because of the silica shell which slows down the burning process of residual organic material in the titania and increases the time for crystal growth. It should also be noted that we have observed longer calcination times for thicker silica coated particles.

Nitrogen adsorption/desorption isotherms of the particles were measured to further investigate the porosity of the particles. They were of type I (microporous) except for pure silica colloids which was type II (nonporous). Brunauer-Emmett-Teller (BET) surface area, Barret-Joyner-Halenda (BJH) adsorption average pore diameter and total pore volume of the samples before calcination are tabulated in

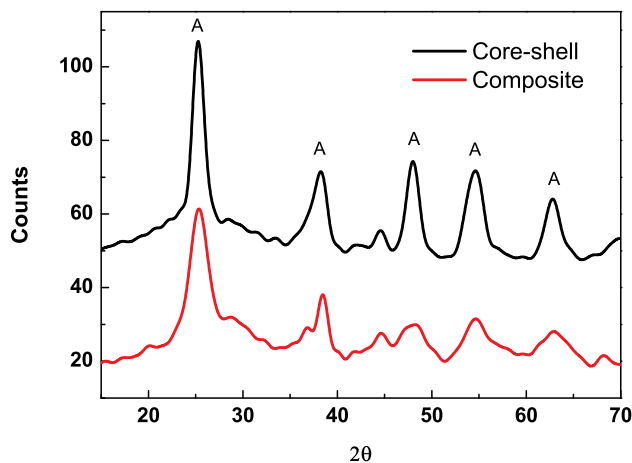


Figure 2.5: The XRD pattern of the calcined $cs\text{-TiO}_2@SiO_2$ particles (upper, 620 °C for 25 minutes) and the calcined titania-silica composite particles (lower, 620 °C for 60 minutes). Typical anatase peaks are denoted with "A".

Table 2.1: BET surface area, the BJH pore size and total pore volumes of the titania particles before calcination

Sample	N ₂ BET (m ² /g)	BJH pore size (nm)	Pore Vol. (cm ³ /g)
<i>comp</i> _TiO ₂ @SiO ₂	273	1.68	0.151
<i>cs</i> _TiO ₂ @SiO ₂	202	1.93	0.117
<i>bare</i> _TiO ₂	232	1.76	0.128
silica	3	4.9	0.0062

Table 2.1. For comparison data on silica colloids prepared by the Stöber method are also included. The particles were all degassed at 150 °C prior to the adsorption measurements, unfortunately making it impossible to do an independent measurement on non-dried titania. Surprisingly, the *comp*-TiO₂@SiO₂ particles had a much higher surface area and pore volume than both the bare titania and the core-shell particles. We believe that this is due to the presence of the silica dispersed throughout the particle, which cements the titania together allowing it to preserve its porosity during the drying step.

High surface area is a crucial parameter for catalytic applications of titania which is well known for its photocatalytic properties. Although inorganic sup-

Table 2.2: Photocatalytic degradation of MB and RITC with bare, eccentric and composite titania particles.

Sample	Exposure time /hour	MB or RITC decomposed
TiO ₂	20	0.61 μmol MB
Ecc-TiO ₂	20	0.29 μmol MB
^a Commercial TiO ₂	1	0.65 μmol MB
^a SiO ₂ /void/TiO ₂	1	0.34 μmol MB
TiO ₂	18	0.34 μmol RITC
Ecc-TiO ₂	18	0.19 μmol RITC
TiO ₂	20	0.21 μmol RITC-PAH
Ecc-TiO ₂	20	0.03 μmol RITC-PAH

^a data is taken from reference 27 for comparison.

ports have been used for size-selective photocatalytic purposes they have always faced the difficulty of preserving the activity of the initially active photocatalyst [25]. Recently, it was shown that a catalyst with a void between the core and shell catalytically may perform better than their no-void core-shell counterparts as they are able to retain the catalytic activity of the starting catalyst [13, 27]. Our *ecc*-TiO₂@SiO₂ particles have similar structure and can be suitable for size-selective catalysis. In order to demonstrate the size-selectivity the photocatalytic activity was evaluated by degradation of various substrates with different sizes in aqueous suspensions. Typical results are summarized in Table 2.2. In the degradation of methylene blue (MB) and RITC which are relatively large (MB is 1.43 nm × 0.61 nm × 0.4 nm) [41] eccentric particles show mildly lower activity compared to the bare particles. However the degradation of the large substrate Poly(allylamine hydrochloride) (PAH; Mw = 15000) coupled to RITC is almost completely suppressed by the silica shell. Additionally, in a mixture of ethanol and RITC-PAH we observed no change at all in the absorbance of the RITC which means that only ethanol was selectively degraded and the silica shell blocked the degradation of the large RITC-PAH. The suppression of photocatalytic activity for the degradation of relatively large molecules compared to the activity of bare titania indicates that these particles are promising for designing photocatalysts with molecular size-selectivity.

Another point of interest for the *ecc*-TiO₂@SiO₂ particles is their regular shape with a sphericity factor of 1.03 and low polydispersity or around 5% (measured by image analysis on TEM images), which gives them the ability to form colloidal crystals. The confocal microscopy image in Fig. 2.6 of *cs*-TiO₂@SiO₂ particles dried from a drop of suspension on a glass microscope slide exhibit 2D hexagonal

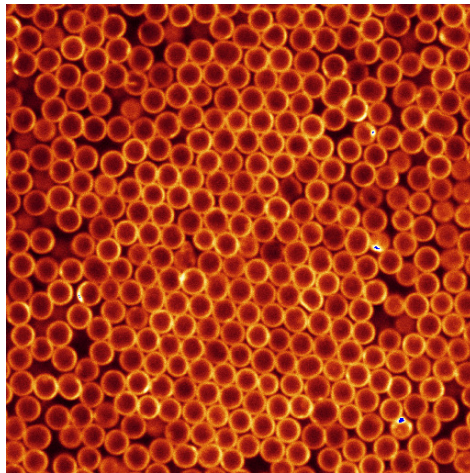


Figure 2.6: The Confocal microscopy images of $cs\text{-TiO}_2@SiO_2$ particles labeled with RITC dried on a glass microscope slide [Image size $37.5\ \mu\text{m} \times 37.5\ \mu\text{m}$]

order and together with the SLS curves in Fig. 2.4 suggest that our system should be monodisperse enough for photonic crystal applications. In a colloidal crystal of eccentric particles the cores will be randomly oriented in the absence of an external field. However an external field may be used to rotate the particles into alignment with the field lines leading to tunability of the band gap [30, 31].

2.4 Conclusions & outlook

We have reported an easy self-templated way of fabricating colloidal eccentric particles and composite particles. This approach produces eccentric particles directly from titania microspheres coated with silica, eliminating the need for costly and time-consuming sacrificial shell-removing steps associated with other procedures. Controlling the access of silica to the pores in the titania offers the flexibility of obtaining various types of particles with important applications in photonic crystals and photocatalysis. Additionally, $comp\text{-TiO}_2@SiO_2$ particles give the opportunity of tuning particle properties like density and refractive index by tuning the fraction of silica added to the titania particle. Controlling pore access should be possible for other materials than silica as well and could lead to a whole range of functional composite particles. Chapter 3 shows our work on producing colloidal $BaTiO_3$ and $SrTiO_3$ particles from Ba and Sr salts using this approach.

Acknowledgements

First of all, we thank Andrew I. Campbell for introducing us the synthesis of titania particles and for fruitful discussions. J.D. Meeldijk (Electron Microscopy Utrecht) is thanked for the assistance with the EDX measurements. Mariska Wolters (Utrecht University, Inorganic Chemistry & Catalysis) is also thanked for the nitrogen adsorption measurements.

References

- [1] Stöber, W.; Fink A.; Bohn, E. *J. Colloid Interface Sci.* **1968**, *26*, 62.
- [2] Pekarek, K.J.; Jacob, J.S.; Mathiowitz, E. *Nature* **1994**, *367*, 258.
- [3] Liang, H.P.; Zhang, H.M.; Hu, J.S.; Guo, Y.G.; Wan, L.J.; Bai, C.L. *Angew. Chem. Int. Ed.* **2004**, *116*, 1566.
- [4] Zhu, Y.; Shi, J.; Shen, W.; Dong, X.; Feng, J.; Ruan, M.; Li, Y. *Angew. Chem. Int. Ed.* **2005**, *117*, 5213.
- [5] Li, J.; Zeng, H.C. *Angew. Chem. Int. Ed.* **2005**, *117*, 4416.
- [6] Chen, J.Y.; Wiley, B.; Li, Z.Y.; Campbell, D.; Saeki, F.; Cang, H.; Au, L.; Lee, J.; Li, X.D.; Xia, Y.N. *Adv. Mater.* **2005**, *17*, 2255.
- [7] Shchukin, D.G.; Sukhorukov, G.B. *Adv. Mater.* **2004**, *16*, 671.
- [8] Lou, X.W.; Yuan, C.; Archer, L.A. *Adv. Mater.* **2007**, *19*, 3328.
- [9] Lu, Y.; Fan, H.; Stump, A.; Ward, T.L.; Rieker, T.; Brinker, C.J. *Nature* **1999**, *398*, 223.
- [10] Schacht, S.; Huo, Q.; Voigt-Martin, I. G.; Stucky, G. D.; Schuth, F. *Science* **1996**, *273*, 768.
- [11] Thurmond, K.B.; Kowalewski, T.; Wooley, K.L. *J. Am. Chem. Soc.* **1997**, *119*, 6656.
- [12] Discher, B.M.; Won, Y.Y.; D.S.; Ege, J.; Lee, C.M.; Bates, F. S.; Discher, D. E.; Hammer, D. A. *Science* **1999**, *284*, 1143.
- [13] Arnal, P.M.; Comotti, M.; Schuth, F. *Angew. Chem. Int. Ed.* **2006**, *45*, 8224.
- [14] Zhong, Z.; Yin, Y.; Gates, B.; Xia, Y. *Adv. Mater.* **2000**, *12*, 206.
- [15] Wu, D.; Ge, X.; Zhang, Z.; Wang, M.; Zhang, S. *Langmuir* **2004**, *20*, 5192.
- [16] Chen, Z.; Zhan, P.; Wang, Z.; Zhang, J.; Zhang, W.; Ming, N.; Chan, C.T.; Sheng, P. *Adv. Mater.* **2004**, *16*, 417.
- [17] Pavlyuchenko, V.N.; Sorochinskaya, O.V.; Ivanchev, S.S.; Klubin, V.V.; Kreichman, G.S.; Budtov, V.P.; Skrifvars, M.; Halme, E.; Koskinen, J. *J. Polym. Sci. Polym. Chem.* **2001**, *39*, 1435.
- [18] Caruso, F.; Caruso, R. A.; Möhwald, H. *Science* **1998**, *282*, 1111.
- [19] Kim M.; Sohn, K.; Bin, Na H.; Hyeon, T. *Nano Lett.* **2002**, *12*, 1383.
- [20] Hah H.J.; Um J.I.; Han, S.H.; Koo, S.M. *Chem. Commun.* **2004**, 1012.
- [21] Cheng, D.; Zhou, X.; Xia, H.; Chan, H.S.O. *Chem. Mater.* **2005**, *17*, 3578.
- [22] Zhang, K.; Zhang, X.; Chen, H.; Chen, X.; Zheng, L.; Zhang, J.; Yang, B. *Langmuir* **2004**, *20*, 11312.
- [23] Kim, J.Y.; Yoon, S.B.; Yu, J.S. *Chem. Commun.* **2003**, 790.
- [24] Lee J.; Park J.C.; Song H. *Adv. Mater.* **2008**, *20*, 1523.
- [25] Harris, P.J.F. *Journal of Catalysis* **1986**, *97*, 527.
- [26] Ikeda, S.; Ikoma, Y.; Kobayashi, H.; Harada, T.; Torimoto, T.; Ohtani, B.; Matsumura, M. *Chem. Commun.* **2007**, 3753.
- [27] Ikeda, S.; Kobayashi, H.; Ikoma, Y.; Harada, T.; Torimoto, T.; Ohtani, B.; Matsumura, M. *Phys. Chem. Chem. Phys.* **2007**, *9*, 6319.
- [28] Behrens, P. *Adv. Mater.* **1993**, *5*, 127.
- [29] Lu, Z.; Xu, J.; Han, Y.; Song, Z.; Li, J.; Yang, W. *Colloids and Surfaces A: Physicochem. Eng. Aspects* **2007**, *303*, 207.
- [30] Camargo, P.H.C.; Lib, Z.Y.; Xia, Y. *Soft Matter*, **2007**, *3*, 1215.
- [31] Ge, J.; Hu, Y.; Yin, Y. *Angew. Chem. Int. Ed.* **2007**, *46*, 7428.
- [32] Lou X.W.; Yuan C.; Archer L.A. *Small*, **2007**, *3*, 261.
- [33] Eiden-Assmann, S.; Widoniak, J.; Maret, G. *Chem. Mater.*, **2004**, *16*, 6.
- [34] van Blaaderen, A.; Vrij, A. *Langmuir*, **1992**, *8*, 2921.
- [35] Schnackel, A.; Hiller, S.; Reibetanz, U.; Donath, E.; *Soft Matter*, **2007**, *3*, 200.
- [36] Zoldesi, C.I.; Imhof, A. *Adv. Mater.* **2005**, *17*, 924.
- [37] Bohren, C.F.; Huffman, D.R. *Absorption and Scattering of Light by Small Particles*; Wiley: New York, 1983.

- [38] Kerker, M.; Farone, W.A.; Smith, L.B.; Matijevic, E. *J. Coll. Sci.* **1964**,*19*, 193.
- [39] Lee, S.H.; Roichman, Y.; Yi, G.R.; Kim, S.H.; Yang, S.M.; van Blaaderen, A.; van Oostrum, P.; Grier, D.G. *Optics Express* **2007**,*15*, 18275.
- [40] Horikoshi S.; Satou Y.; Hidaka H.; Serpone N. *J. Photochemistry and Photobiology A-Chemistry* **2001**, *146*, 1-2, 109.
- [41] Costas, P.; Snoeyink, V.L. *Carbon* **2000**, *38*, 1423.

3

BaTiO₃, SrTiO₃, CaTiO₃ and Ba_xSr_{1-x}TiO₃ particles: A General Approach for Colloidal Perovskites

We describe a novel general method for synthesizing monodisperse colloidal perovskite particles at room temperature by post-synthesis addition of other components to amorphous titania colloids. In our previous work we used the titania particles to synthesize homogeneously mixed silica-titania composite particles by addition of silica components to the titania particles (Demirörs et al. *Chem. Mater.*, 2009, 21, 979). Here we show that the principle is general and can be used to prepare different titania based composite beads. We demonstrate the syntheses of colloidal perovskites like BaTiO₃, SrTiO₃, CaTiO₃ and mixed Ba_{0.5}Sr_{0.5}TiO₃, which have importance for the electronics industry for their dielectric properties. Mixed perovskites like Ba_xSr_{1-x}TiO₃ brings tunability in structure and properties by changing the ratio of metal cations. We also show fabrication of metal core-BaTiO₃ shell particles which could find applications in percolative capacitors and luminescence properties of Pr³⁺ doped colloidal perovskites.

3.1 Introduction

The fabrication of perovskites (oxides with the formula ABO_3) is of great scientific and technological interest for their ferroelectric, pyroelectric, piezoelectric, dielectric and catalytic properties [1–3]. Barium titanate, one of the most investigated perovskite materials, has a high dielectric constant [4–6] and ferroelectric properties [7, 8] that are essential for thin-film electronic components and electro-optical materials [3, 9–12]. It is heavily used in industry as dielectric material component of class II ceramic capacitors [13]. $BaTiO_3$ exists in various crystallographic structures, of which the tetragonal and cubic polymorphs are the most studied. Although the tetragonal polymorph is the thermodynamically stable form at room temperature, most synthesis routes result in the cubic structure, and a high temperature treatment at around 1100°C is necessary to induce phase transformation from the cubic to the tetragonal structure which persists upon cooling again to room temperature [5, 6, 14].

The tetragonal polymorph of $BaTiO_3$ is ferroelectric and the cubic polymorph is para-electric. Crystallographic structures determine the dielectric properties and one way of changing the structure is making mixed perovskites. It is well established that the Fermi level and polymorph stable at room temperature can be tuned by making mixed perovskite structures [15, 16]. For $SrTiO_3$ the thermodynamically stable form at room temperature is cubic and for $CaTiO_3$ it is orthorhombic [17]. $SrTiO_3$ has often been used as a dielectric and photoelectric material, whereas $CaTiO_3$ is recently getting attention for its biocompatibility and implant bone applications [18, 19] besides its use in electronics [20].

Reports for the preparation of micrometer-sized colloidal perovskites are mostly based on hydrothermal treatment of amorphous titania particles with metal salts [21, 22]. However these particles usually are composed of nano-sized smaller primary particulates and upon sonication the particles readily disintegrate, which is basically an outcome of the harsh conditions of the hydrothermal treatment. Recently Niederberger et al. [23] and O'Brien et al. [24] succeeded in synthesizing monodisperse and highly crystalline $BaTiO_3$ particles in organic media, however these particles are on the order of 5-10 nm. One notable method for nanometer sized perovskites was the inverse micellar synthesis of Su et al. [25] which decreased the synthesis temperature to as low as 80°C . An epitaxial self assembly method was used by Calderone et al. [26] to synthesize submicrometer sized $SrTiO_3$ cubes and spheres particles but this work was not applicable to all metal salts but to only Sr.

Here we present a new method based on a mild post-synthesis treatment to amorphous and porous titania particles. It yields monodisperse colloidal perovskites that are strong enough to withstand sonication and can thus be easily redispersed. Compared to the conventional method used in industry, which is based on solid-solid reaction of the barium salt (usually $BaCO_3$) with anatase titania at elevated temperatures, our method is advantageous in bringing the barium and

titanium into nanometer level contact, which decreases the time and the cost for the crystal formation. Especially for the industrial production where monodispersity and size is usually not the most crucial priority the synthesis of titania can be done in a more rough way in the presence of a polymer surfactant which we think will have similar properties (porosity, particle size etc.) to our titania beads. Additionally our method is facile for its availability for post-synthesis intervention like adding different types of metal salts with different ratios, which opens a way to tune the structure and the dielectric properties or to dope the structure with rare earth metals for luminescence.

3.2 Experimental details

The synthesis of colloidal perovskite particles is based on the conversion of titania particles. We synthesized the titania particles according to the procedure of Eiden-Assmann et al. [27] with slight modifications. In a typical synthesis 250 ml ethanol with 17.0 ml Ti(OC₂H₅)₄ was mixed with 750 ml of ethanol with 4.0 ml of 0.1 M aqueous Lutensol ON50 (BASF) solution. This gave monodisperse titania particles with a size between 900-1200 nm depending on the reaction temperature and the amount of the titania precursor. The titania particles collected by centrifugation were then dispersed in fresh ethanol without drying. For confocal microscopy measurements fluorescent rhodamine isothiocyanate (RITC) dye was added to the dispersion of the particles and the particles were centrifuged afterwards. Because the dye was only physisorbed to the particles the particles were not washed more than twice. Perovskites with the general formula ATiO₃ (where A= Ba, Sr, Ca or a mixture of Ba and Sr.) were achieved by adding 1:1 A/Ti mole ratio of A(OH)₂ salt, into the ethanolic dispersion of titania particles. In a typical preparation for 0.035 g of titania beads dispersed in 10 ml of ethanol we have added 0.046 g of Sr(OH)₂, 0.064g of Ba(OH)₂ or 0.021g of Ca(OH)₂. The mixed dispersions were sonicated for 20-30 minutes and collected by centrifugation, then dried in a 50 °C oven which resulted in perovskite gels. The sonication step improved contact between the insoluble particles. Perovskite gels were calcined at various temperatures between 700-1200 °C for 1 hour to obtain crystalline perovskites. Particles were redispersed in ethanol by sonication.

Ag@BaTiO₃ particles were synthesized from Ag@TiO₂ core-shell particles with an amorphous titania shell. Ba(OH)₂ salt was added to Ag@TiO₂ particles dispersed in ethanol with 1:1 Ba/Ti mole ratio and similar route to perovskites was followed. The Ag particles were prepared using the method of Tao et al. [28] and coated in a similar way to the synthesis of titania particles by using Lutensol ON 50 surfactant.

The powder XRD measurements were performed with a Philips PW 1820 diffractometer with a Philips PW 1729 X-ray generator (Cu K_α radiation). We used either a glass or an aluminum substrate for the XRD measurements.

Transmission Electron Microscopy (TEM) images were obtained with a Philips

Tecnai 12 transmission electron microscope with an accelerating voltage of 120 keV. Samples for TEM were prepared by dipping copper 300 mesh carrier grids covered with carbon-coated Formvar films into dilute suspensions.

Scanning Electron Microscopy (SEM) micrographs were obtained with a Philips XL 30 FEG scanning electron microscope, and the samples were prepared by drying a drop of particle suspension on a SEM stub.

The fluorescently labeled particles were imaged using an inverted Leica confocal scanning laser microscope (CSLM), type TCS-SP2. The microscope was operated in the fluorescence mode. The 543 nm line of a green He-Ne laser was used for excitation of the rhodamine-labeled particles and 488 nm line of Ar laser was used for the Pr doped perovskites.

Luminescence spectra was obtained with a Perkin Elmer LS 50B luminescence spectrometer.

3.3 Results and discussion

In our previous work we have found that amorphous titania particles are very sensitive to drying; particles dried in oven at 50 °C for 2 hours could be coated with silica under Stöber conditions which yielded core-shell particles [29]. However, particles treated with silica prior to drying formed homogeneously mixed composite $\text{TiO}_2\text{-SiO}_2$ particles [30]. The formation of homogeneously mixed composite particles proves that particles as-synthesized are porous and open to the access of the species added after the synthesis. The porosity difference between dried and non-dried particles could also be observed by addition of a fluorescent dye (RITC) to dispersions of either type of particle (Fig. 3.1). Although the dye molecules could reach the inner parts of the as-synthesized particles yielding fully dyed particles (Fig. 3.1a), dried particles fluoresced only on the surface, indicating that the dye could adsorb on the outer surface of the particle but no further (Fig. 3.1b).

In this article we demonstrate that this principle for making composite particles by post-synthesis addition of new components is general and can be applied to make perovskite gels by adding metal salts with 1:1 A/Ti mole ratio to the titania particles. Sonication improves nanometer level contact between metal oxides and highly porous titania. A better contact between species stimulates the formation of crystalline perovskite structures upon calcination at 700-900 °C. Fig. 3.2a, b, c shows the XRD patterns of the colloidal BaTiO_3 , SrTiO_3 , CaTiO_3 powders synthesized. The XRD patterns only include the peaks of the pure perovskite structures and have no peaks of impurities like BaCO_3 or SrCO_3 nor peaks of anatase or rutile titania. Since no washing steps were used for the XRD measurements this indicates that perovskite gel formation is close to stoichiometric and no impurities exist. These XRD patterns can be indexed to cubic BaTiO_3 (JCPDS No. 74-1968), SrTiO_3 (JCPDS No. 73-0661), and CaTiO_3 (JCPDS No. 22-153). To demonstrate the fact that the perovskite gel formation only occurs stoichiometrically if the titania is not dried, we added 1:1 A/Ti ratio metal salts to the dried

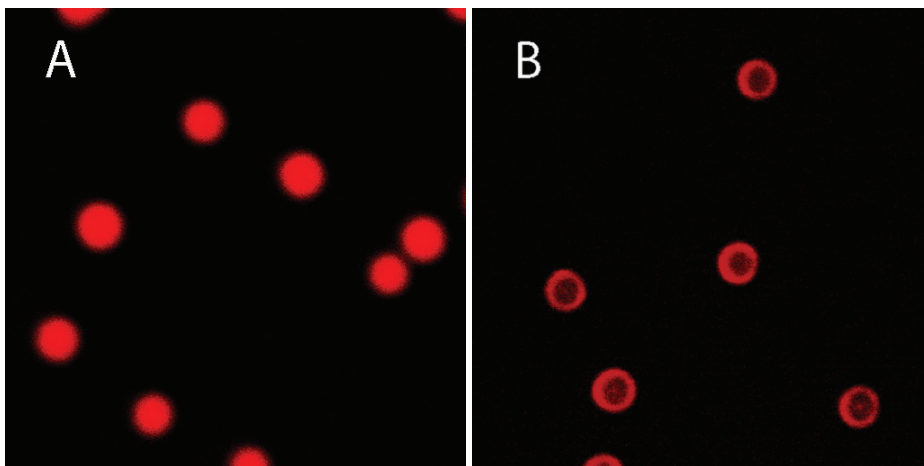


Figure 3.1: Confocal microscopy image of (a) as-synthesized titania particles after addition of fluorescent dye, (b) dried titania particles after addition of fluorescent dye. Dye adsorbs only on the surface. It should be noted that the point spread function of the confocal microscope has a width of 250 nm, close to the width of the rings in (b). (Image size of (a) = $8.38\mu\text{m} \times 8.38\mu\text{m}$, (b) = $14.68\mu\text{m} \times 14.68\mu\text{m}$).

particles and calcined the sonicated mixture. The resulting XRD patterns are given in Fig. 3.2d, e and show clear peaks of anatase, rutile and SrCO₃ impurities. This proves that drying prevents pore access of added species so that titania particles after calcination become anatase or a mix of anatase and rutile, whereas the excess Sr salt forms SrCO₃ by capturing CO₂ from air or stays as amorphous BaO in case of Ba salt. In Fig. 3.2d the (101) peak of BaTiO₃ is barely visible whereas in Fig. 3.2e the SrTiO₃ titanate peaks are more pronounced. Perovskite formation is not complete for dried particles and leaves some non-reacted free titania and metal salt, which upon calcination forms anatase, rutile or carbonate impurities.

SEM images (Fig. 3.3) show that the perovskite particles are well defined spheres. However it is also observed that the surface is very rough which indicates that the particles are porous. Crystalline domains were visible from the HR-SEM images with domain sizes of the range 70-100 nm for BaTiO₃, the domain sizes were smaller in SrTiO₃, ranging from 20-60 nm and it was intermediate for the Ba_{0.5}Sr_{0.5}TiO₃ with 50-70nm domain size. The larger domain sizes for BaTiO₃ caused a structure with macropores inside, whereas particle surfaces were smoother in SrTiO₃ particles, and the surface roughness was in between for the Ba_{0.5}Sr_{0.5}TiO₃. It should also be noted that these perovskite particles had a size of 1.5 μm whereas the initial amorphous titania particles were only 1.2 μm after drying. This difference was caused by the incorporation of the metal salts to the structure. The titania particles (in a solvent) prior to drying were much larger in size and upon drying particles shrank and densified. In our previous work we have found that amorphous titania particles prior to drying were as

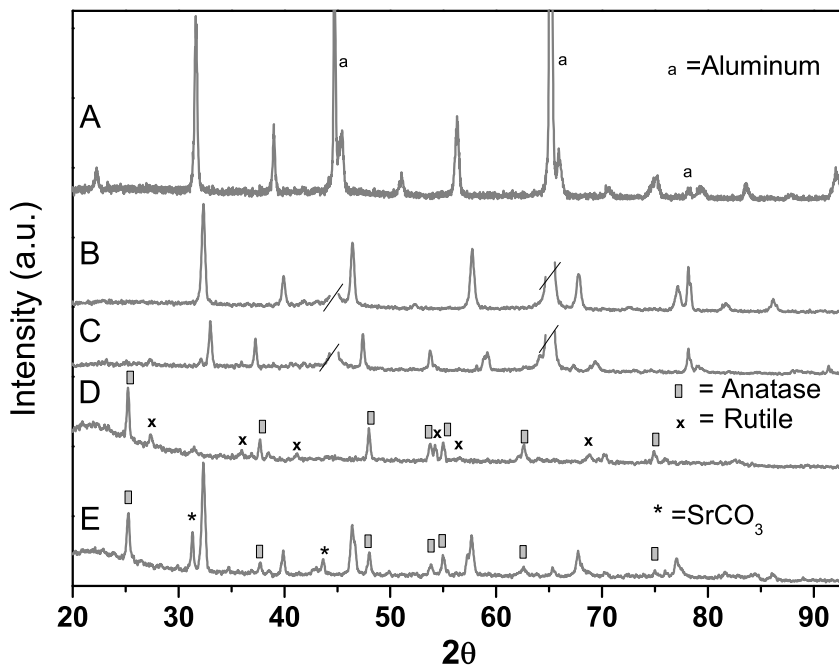


Figure 3.2: XRD patterns of colloidal perovskites (a) BaTiO_3 calcined at 900°C , (b) SrTiO_3 calcined at 900°C , (c) CaTiO_3 calcined at 1000°C , XRD pattern of (d) core-shell BaTiO_3 and (e) core-shell SrTiO_3 particles synthesized by mixing Ba and Sr salts with dried-titania particles, which include anatase, rutile and perovskite peaks all. The peaks at 44.7° and 65.3° and 78.2° at (a), (b) and (c) are due to the aluminum substrate and the broad peak around 25° at (d) and (e) belongs to the glass substrate, the aluminum lines are cut in (b) and (c).

large as $1.8\ \mu\text{m}$ and shrank to $1.3\ \mu\text{m}$ upon drying, determined by the static light scattering technique [30]. This result shows that there is enormous shrinkage of the as-synthesized particles after drying. However addition of the metal salts fills the pores and lowers the amount of shrinkage to $1.5\ \mu\text{m}$ in the fabrication of perovskites.

The microstructure of the particles were also investigated by means of TEM. Fig. 3.4a, b, c shows the TEM images of BaTiO_3 , SrTiO_3 and $\text{Ba}_{0.5}\text{Sr}_{0.5}\text{TiO}_3$ respectively. The sphericity of the titania particles was preserved during the synthesis of perovskites. It can be concluded from these images that the particles are monodisperse and do not disintegrate upon sonication. EDX spectra made on a point on the perovskite particles showed both Ti and metal peaks (Fig. 3.5b and c). The Ba and Ti peaks are closely spaced and partially overlapping so we made an energy dispersive X-ray (EDX) profile on a single particle for the SrTiO_3 which showed that Sr was homogeneously spread inside the particle (See Fig. 3.5a)

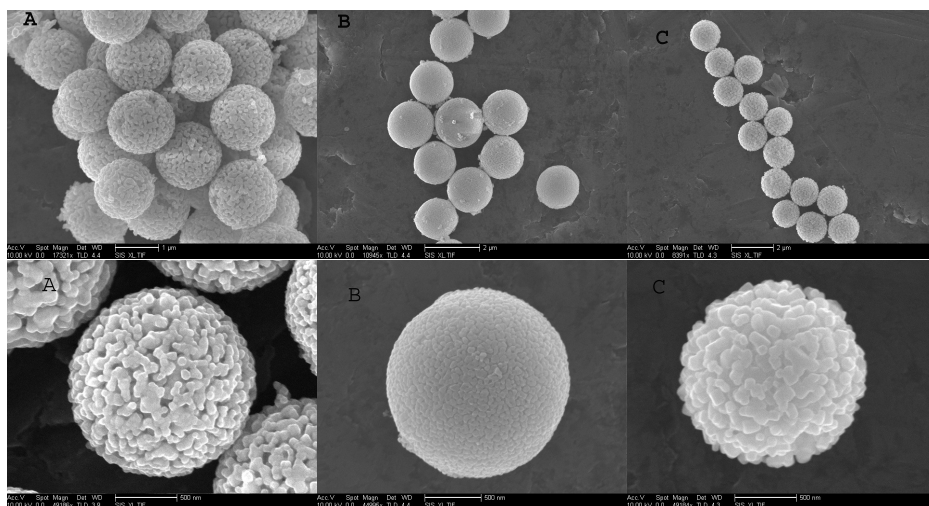


Figure 3.3: SEM images of the (a) BaTiO₃ particles calcined at 900^oC, (b) SrTiO₃ particles calcined at 850^oC, (c) Ba_{0.5}Sr_{0.5}TiO₃ particles calcined at 900^oC. The images below are magnified HR-SEM images for better visibility of the porous structure. Scale bars above images (a) 1 μm (b) and (c) 2 μm. For the images below, all scale bars are 500 nm.

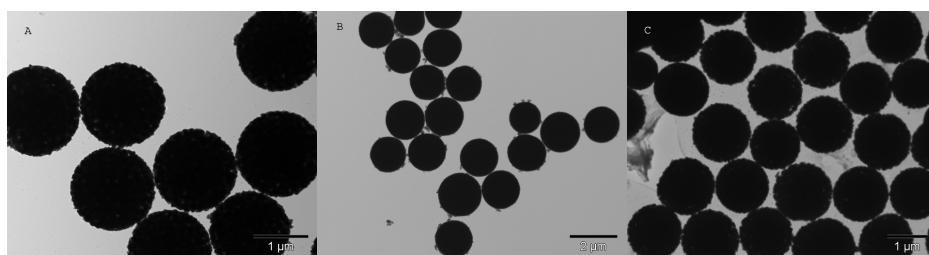


Figure 3.4: TEM images of (a) BaTiO₃ particles calcined at 900^oC, (b) SrTiO₃ particles calcined at 850^oC and (c) Ba_{0.5}Sr_{0.5}TiO₃ particles calcined at 900^oC, all particles were sonicated several minutes prior to deposition on a TEM grid.

Energy-Dispersive X-ray Spectroscopy (EDX). The elemental microanalysis of perovskite particles were achieved by performing EDX measurements on a Philips Tecnai 20F high-resolution transmission electron microscope operated at 200 keV, in scanning mode (STEM). The same types of samples as for TEM were used. The identical profile of EDX for gel and crystalline SrTiO₃ particles proves that the metal cations are well dispersed in the particle prior to calcination.

The BaTiO₃ particles after calcination at 700-900^oC had the cubic lattice, which is known to be para-electric. Phase transformation from the cubic to the ferroelectric tetragonal polymorph of BaTiO₃, which is the stable form at room temperature, can be induced by calcining the cubic sample to 1100-1300^oC. We

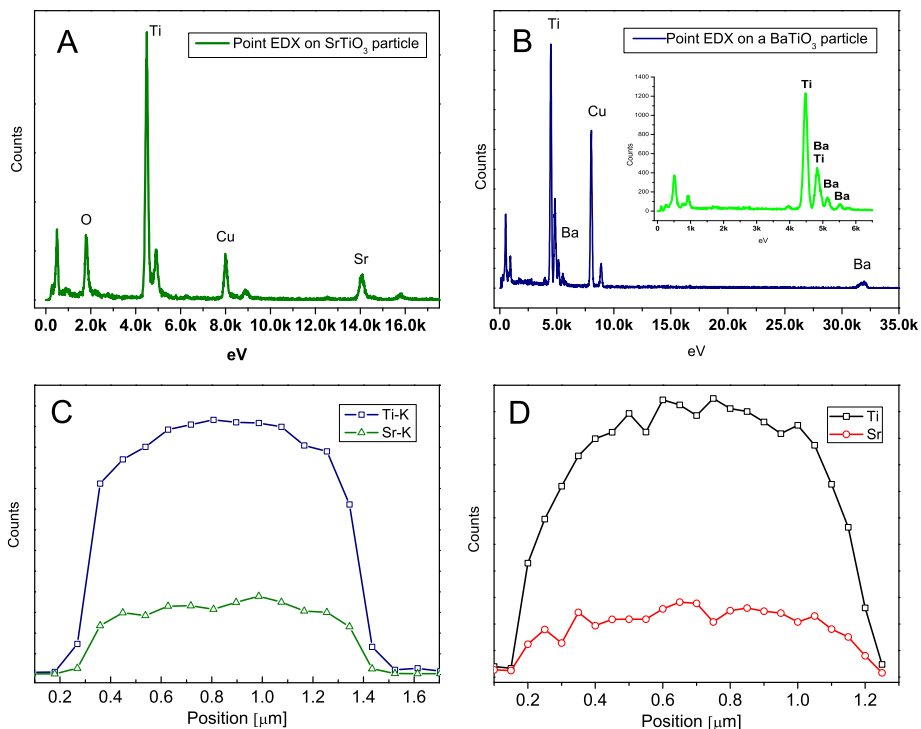


Figure 3.5: The EDX measurements on perovskite particles. (a) EDX spectrum on a spot at a SrTiO₃ particle (b) EDX spectrum on a spot at a BaTiO₃ particle, inset is the zoom to the region between 1-6 keV where the Ti and Ba peaks overlap, however Ba has 4 peaks with decaying intensity (Ti has 2 peaks). Here the last two are clearly visible, (c) EDX profile of a line-scan on a SrTiO₃ gel particle prior to calcination, (d) EDX profile of a line-scan on a SrTiO₃ particle after calcination at 900°C for 1 hour.

calcined our BaTiO₃ particles at 1200°C to observe the phase transformation from cubic to tetragonal. In literature the phase transformation is usually detected from the splitting of the (200) peak cubic at 45.4° into (002) and (200) of the tetragonal phase. This splitting was observed in our BaTiO₃ particles as well (Fig. 3.6). From the XRD of the tetragonal BaTiO₃ we found the *c/a* ratio to be 1.004. Although the particles became ferroelectric due to the high temperature treatment they lost sphericity and partially sintered together (Fig. 3.6b).

Mixed perovskites have importance for tuning structural and dielectric properties. The phase diagram of Ba_{*x*}Sr_{1-*x*}TiO₃ has cubic and tetragonal structures. In the case of the ternary perovskite Ba_{*x*}Sr_{*y*}Ca_{1-*x-y*}TiO₃ the orthorhombic phase also appears in the phase diagram [15]. To demonstrate that our method can equally well be used to prepare mixed perovskites, we have prepared Ba_{0.5}Sr_{0.5}TiO₃. The XRD pattern of the Ba_{0.5}Sr_{0.5}TiO₃ particles (Fig. 3.7) showed peaks exactly

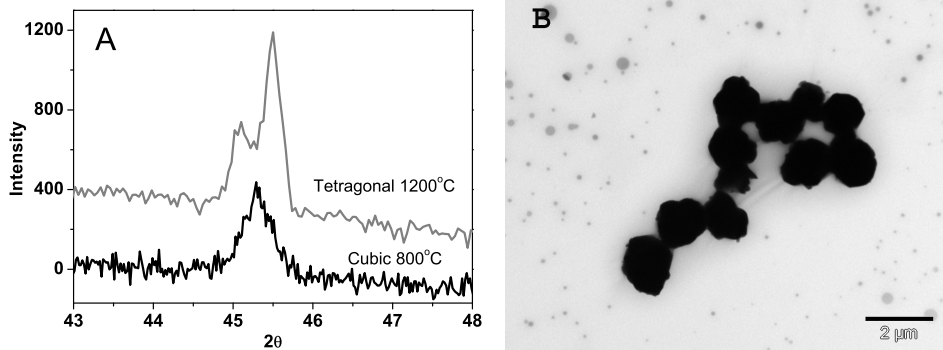


Figure 3.6: BaTiO₃ particles as synthesized are amorphous gels but after calcination between 700–1000°C the particles are cubic in structure. Calcination at higher temperatures results in tetragonal structure which is known to be ferroelectric. (a) The change in structure from cubic to tetragonal causes a splitting of the (200) peak, (b) TEM image of BaTiO₃ particles calcined at 1200°C for 1 hour.

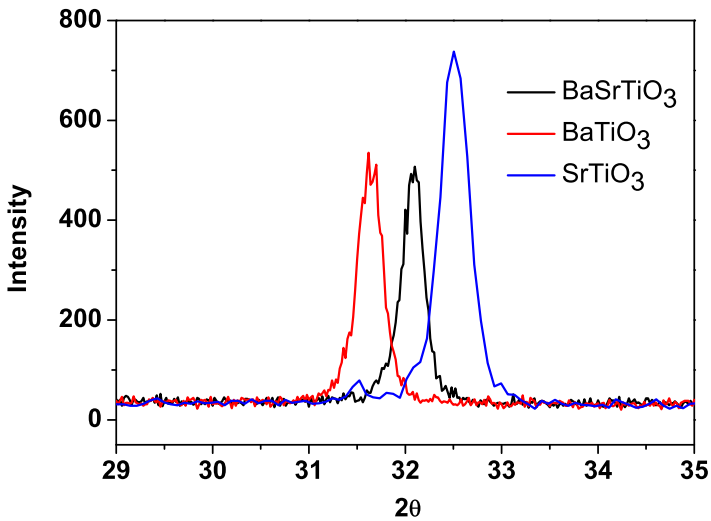


Figure 3.7: Ba_{0.5}Sr_{0.5}TiO₃ particles as synthesized are gel, after calcination at 900°C we observe mixed Ba_{0.5}Sr_{0.5}TiO₃ structure with averaged unit cell parameters between BaTiO₃ and SrTiO₃. This averaging shows that the mixing is at atomic level and (Ba+Sr)/Ti ratio is close to unity.

between the corresponding peaks of BaTiO₃ and SrTiO₃. This means that the differently-sized Ba and Sr atoms have mixed at a nanometer level causing the unit cell parameters to be averaged. We think that this nice averaging of the unit cell parameters is also evidence that the A/Ti ratio is close to unity, such that in-

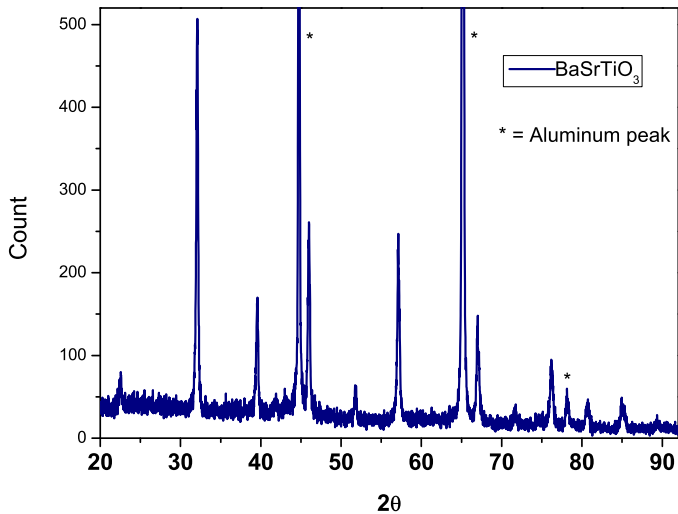


Figure 3.8: The full XRD pattern of the $\text{Ba}_{0.5}\text{Sr}_{0.5}\text{TiO}_3$ particles calcined at 900°C .

side the colloidal particle metal salts disperse uniformly and that using two metal salts instead of one introduced no impurity peaks. (For a full XRD pattern of the $\text{Ba}_{0.5}\text{Sr}_{0.5}\text{TiO}_3$ particles see Fig. 3.8)

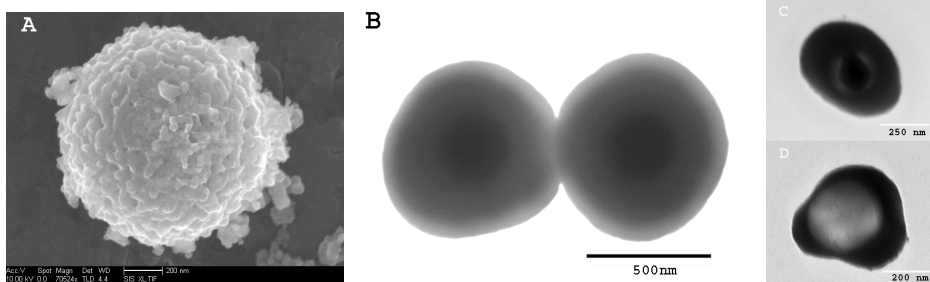


Figure 3.9: (a) An SEM image of Ag@BaTiO_3 particles after calcination with a rough surface which indicates the shell to be BaTiO_3 (b) The original Ag@TiO_2 particles before BaOH_2 treatment (contrast increased), Ag@TiO_2 particles etched with concentrate HNO_3 where (c) is partially, 1 day and (d) is fully etched, 2 days.

To demonstrate the generality of our approach, we also fabricated Ag core- BaTiO_3 shell (Ag@BaTiO_3) particles starting from Ag@TiO_2 particles. Core-shell BaTiO_3 with a conductive core and with a ferroelectric shell is crucial for production of percolative capacitors [12, 18]. The amorphous shell of Ag@BaTiO_3 crystallized upon calcination at 900°C . It could be expected that silver oxide would

have been formed due to contact with air, but this was not the case, as seen from the XRD pattern (see Fig. 3.10). We think that the oxidation is prohibited due to the thick layer of BaTiO₃. From the SEM image of the Ag@BaTiO₃ particles in Fig. 3.9a it was observed that the surface is similar in texture to the BaTiO₃ particle surface. The core-shell structure of the original particles can be seen in Fig. 3.9b, c and d. Fig. 3.9b is the TEM image of the Ag@TiO₂ particles and Fig. 3.9c and d are Ag@TiO₂ particles etched with concentrated HNO₃, partially and fully etched, respectively. Note that due to the softness of the shell the fully etched particles in Fig. 3.9d collapsed. From the SEM images the Ag particles were estimated to be 250 ± 20 nm in size whereas the Ag@TiO₂ particles were found to be 690 ± 45 nm from TEM image analysis. The titania shell around the Ag core is therefore about 220 nm thick. The thickness affects the oxidation time for the oxidation of Ag as well as the etching time of the Ag core with 65% (v/v) HNO₃. To our surprise the Ag core of the Ag@TiO₂ particles were not yet fully etched after one night exposure to concentrated HNO₃, whereas bare Ag particles were etched in seconds under the same conditions. It was not possible to etch the Ag core in Ag@BaTiO₃ at all. Note that a similar result was found by Lee et al. although they only had a 10 nm thick BaTiO₃ shell [12].

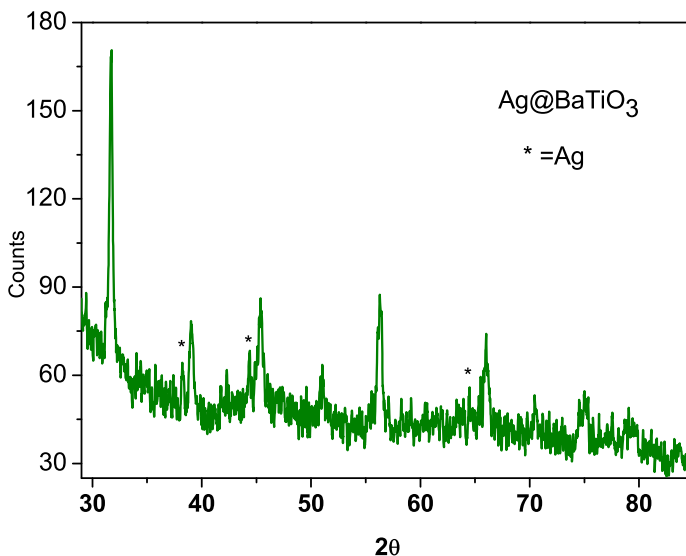


Figure 3.10: The XRD pattern of the Ag@BaTiO₃ particles calcined at 900° C. The peaks due to Ag are depicted with the (*) sign and BaTiO₃ were assigned to cubic polymorph.

The XRD pattern shows all the peaks for the BaTiO₃, additionally the weak peaks at 38.1, 44.4 and at 64.8 can be assigned to Ag (111), (200) and (220), respectively.

Our synthesis route offers the opportunity to easily manipulate the proper-

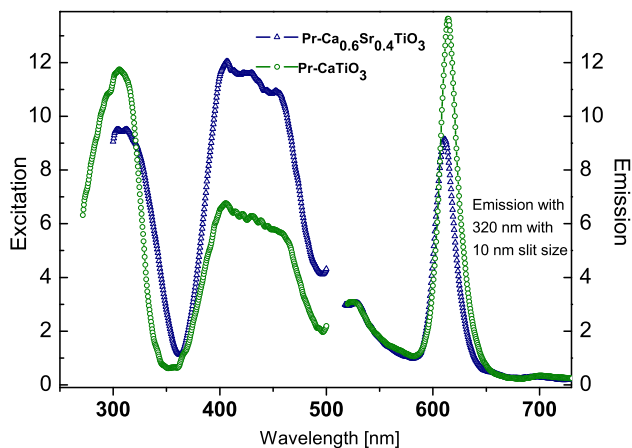


Figure 3.11: The excitation and emission spectra of Pr doped CaTiO_3 and $\text{Ca}_{0.6}\text{Sr}_{0.4}\text{TiO}_3$ particles. Excitation spectra on the left were collected for the 613 nm emission and the emission spectra on the right were excited with 320 nm with a 10 nm slit size in both cases.

ties of the particles after the titania synthesis. To demonstrate this we have successfully fabricated luminescent $\text{Ca}_{0.6}\text{Sr}_{0.4}\text{TiO}_3$ and CaTiO_3 particles doped with 0.2% Pr^{3+} salt by adding the salt into the dispersion of titania particles together with Ca or Ca, Sr mixed salts. The mixed dispersion was sonicated, dried, and calcined at 900°C for 1 hour. The luminescence peak at 613 nm of $\text{Pr}:\text{CaTiO}_3$ was clearly observed and it was preserved in the $\text{Ca}_{0.6}\text{Sr}_{0.4}\text{TiO}_3$ case with a decrease in the intensity and shift to a lower wavelength, which is also known for bulk, see Fig. 3.11 [15, 31]. As the Sr concentration increases the excitation intensity at 320 nm decreases whereas the excitation intensity at 410 nm (broad) increases. For $\text{Ca}_x\text{Sr}_{1-x}\text{TiO}_3$ it is also known that there is another emission at 491 nm that increases in intensity with an increase in the Sr ratio from $x=0$ to $x=0.3$ [15, 32]. The intensity of 491 nm emission has a maximum at $x=0.3$, starts decreasing over 0.3 and vanishes at $x=0.5$ [32]. We also observed this emission of $\text{Ca}_{0.6}\text{Sr}_{0.4}\text{TiO}_3$ particles at 491 nm by only exciting with 410 nm wavelength but not with 320 nm (Fig. 3.13). Thus we think that the 410 nm extinction is the cause of the emission at 491 nm, which increases with the increase of Sr/Ti ratio. We have observed the luminescence of single particles under a microscope by exciting with an Hg lamp filtered for the 350-380 nm region. The red emission of the particles is clearly visible (see Fig. 3.12).

For $\text{Ca}_x\text{Sr}_{1-x}\text{TiO}_3$ the emission at 491 nm is already known [15]. For our sample we observed this emission only when excited with 400-480 nm but not at 300-320 nm region. It could be due to lower calcination temperature than

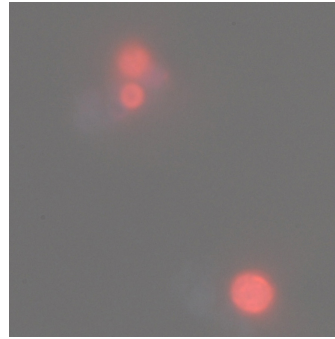


Figure 3.12: A typical microscopy image of Pr doped perovskite particles illuminated with a Hg lamp filtered with a filter cube exciting within 350-380 nm. The particles were dried on a glass slide for imaging. The red 613 nm emission is directly visible. In this particular case the particles were Pr doped CaTiO₃.

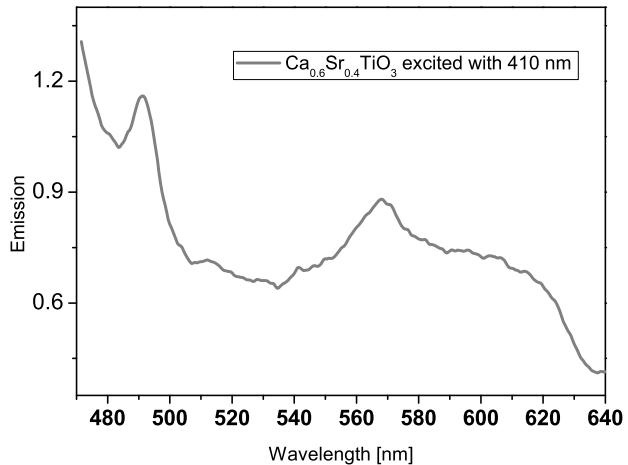


Figure 3.13: The Emission spectrum for Pr doped Ca_{0.6}Sr_{0.4}TiO₃ particles excited with 410 nm. In addition to the peak at 491nm there is also broad peak in red including 613 nm.

1300°C. There is still emission at 613 nm but very broad, note also that there is another peak at 567 nm.

3.4 Conclusions & outlook

We have reported an easy way of fabricating colloidal perovskite particles. Controlling access of metal salts to the pores in the titania by an optional drying step, shows that the synthesis relies on the porous structure of the as-synthesized titania particles. After calcination the perovskites are highly crystalline and monodisperse in size. These colloidal particles are potentially important for making films for electronic and photonic applications. This method offers the flexibility of obtaining various types of perovskite structures simply by changing the metal salt. Various types of stable crystallographic structures can be made by mixing different kinds of metal salts, as shown in the example of Ba_{0.5}Sr_{0.5}TiO₃. The method

also applies to core-shell particles as demonstrated for Ag@BaTiO₃. Additionally the method provides the flexibility of being able to play with the properties of the particles after the synthesis as in the example of doping the particles with Pr for luminescence.

Acknowledgement

First of all, we thank Stephane Badaire (Utrecht University, Soft Condensed Matter) for the synthesis of silver particles and for the SEM images. J. D. Meeldijk (Electron Microscopy Utrecht) is thanked for the assistance with the EDX measurements.

References

- [1] Chandler, C. D.; Roger, C.; Hampden-Smith, M. J. *Chem. Rev.* **1993**, *93*, 1205-1241.
- [2] Pena, M. A.; Fierro, J. L. G. *Chem. Rev.* **2001**, *101*, 1981-2017.
- [3] Bhalla, A. S.; Guo, R.; Roy, R. *Mater. Res. Innovations* **2000**, *4*, 3-26.
- [4] Dutta, P. K.; Asiaie, R.; Akbar, S. A.; Zhu, W. D. *Chem. Mater.* **1994**, *6*, 1542-1548.
- [5] Her, Y.-S.; Matijevic, E.; Chon, M. C. *J. Mater. Res.* **1995**, *10*, 3106- 3114.
- [6] Takeuchi, T.; Tabuchi, M.; Ado, K.; Honjo, K.; Nakamura, O.; Kageyama, H.; Suyama, Y.; Ohtori, N.; Nagasawa, M. *J. Mater. Sci.* **1997**, *32*, 4053- 4060.
- [7] Lee, T.; Aksay, I. A. *Cryst. Growth Des.* **2001**, *1*, 401-419.
- [8] Chen, Z. X.; Chen, Y.; Jiang, Y. S. *J. Phys. Chem. B* **2001**, *105*, 5766- 5771.
- [9] Setter, N.; Waser, R. *Acta Mater.* **2000**, *48*, 151-178.
- [10] Hennings, D.; Klee, M.; Waser, R. *Adv. Mater.* **1991**, *3*, 334-340.
- [11] Haertling, G. H. *J. Am. Ceram. Soc.* **1999**, *82*, 797-818.
- [12] Lee, J.-Y.; Lee, J.-H.; Hong, S.-H.; Lee, Y. K.; Choi, J.-Y. *Adv. Mater.* **2003**, *15*, 1655-1658.
- [13] Moreno, J.; Dominguez, J. M.; Montoya, A.; Vicente, L.; Viveros, T. *J. Mater. Chem.* **1995**, *5*, 509.
- [14] Clark, I. J.; Takeuchi, T.; Ohtori, N.; Sinclair, D. C. *J. Mater. Chem.* **1999**, *9*, 83-91.
- [15] Kyomen, T.; Sakamoto, R.; Sakamoto, N.; Kunugi, S.; Itoh, M. *Chem. Mater.*, **2005**, *17*, 3200-3204.
- [16] Qin, S.; Becerro, A. I.; Seifert, F.; Gottsmanna, J.; Jiang, J. *J. Mater. Chem.*, **2000**, *10*, 1609-1615
- [17] McQuarrie, M. *J. Am. Ceram. Soc.* **1955**, *38*, 444.
- [18] Pecharromon, C.; Esteban-Betegon, F.; Bartolome, J. F.; Lopez-Esteban, S.; Moya, J. S. *Adv. Mater.* **2001**, *13*, No. 20, 1541.
- [19] Ohtsu, N.; Sato, K.; Yanagawa, A.; Saito, K.; Imai, Y.; Kohgo, T.; Yokoyama, A.; Asami, K.; Hanawa, T. *J. Biomed. Mater. Res. A*, **2007**, *82A*, *2*, 304.
- [20] Lemanov, V. V.; Sotnikov, A. V.; Smirnova, E.P.; Weihnacht, M.; Kunze, R. *Solid State Commun.*, **1999**, *110*, 611-614.
- [21] Wang, Y.; Xu, H.; Wang, X.; Zhang, X.; Jia, H.; Zhang, L.; Qiu, J. *J. Phys. Chem. B*, **2006**, *110*, 13835-13840.
- [22] Choi J. Y.; Kim C. H.; Kim D.K. *J. Am. Ceram. Soc.*, **1998**, *81*, 5 1353-1356
- [23] Niederberger M.; Bartl M. H.; Stucky G. D. *J. Am. Chem. Soc.* **2004**, *126*, 9120-9126
- [24] O'Brien S.; Louis B.; Murray C.B. *J. Am. Chem. Soc.*, **2001**, *123*, 12085-12086
- [25] Su K.; Nuraje N.; Yang N. L. *Langmuir* **2007** *23* , 11369 -11372
- [26] Calderone, V. R.; Testino, A.; Buscaglia, M.T.; Bassoli, M.; Bottino, C.; Viviani, M.; Buscaglia, V.; Nanni, P. *Chem. Mater.* **2006**, *18*, 1627-1633.
- [27] Eiden-Assmann, S.; Widoniak, J.; Maret, G. *Chem. Mater.*, **2004**, *16*, 6.
- [28] Tao, A.; Sinsermsuksakul, P.; Yang, P. *Angew. Chem. Int. Ed.* **2006**, *45*, 4597.
- [29] Stöber, W.; Fink A.; Bohn, E. *J. Colloid Interface Sci.* **1968**, *26*, 62.
- [30] Demirörs, A. F.; van Blaaderen A.; Imhof, A. *Chem. Mater.*, **2009**, *21*, 979.
- [31] Diallo, P. T.; Boutinaud, P.; Mahiou, R.; Cousseins, J. C. *Phys. Stat. Sol.(a)*, **1997**, *160*, 255.
- [32] Jia W.; Xu W.; Rivera I.; Perez A.; Fernandez F. *Solid State Commun.*, **2003**, *126*, 153-157.

4

Anatase Core, Titania Shell Colloidal Particles for Optical Tweezing

We describe a novel method to synthesize colloidal particles with an anatase (crystalline titania)-core and an amorphous titania-shell structure. First of all seeded growth of titania onto titania particles was demonstrated. As a result of particle growth, one can tune the size of the particles accurately and improve monodispersity. Secondly, colloidal crystallization of grown monodisperse particles and thirdly, particle coating of titania (or other particles) with an amorphous titania shell becomes feasible with seeded-growth. We also show that by manipulating the amorphous titania shell after the synthesis it is possible to tailor the refractive index of the amorphous shell, an approach which is also applicable to composite particles with no core-shell structure as described in Chapter 2. On the other hand theoretical calculations have shown that if high refractive index particles like crystalline titania (refractive index 2.3) have a coating of certain refractive index-shell, in this particular case 1.8 gives an optimum, then these particles can be trapped in optical tweezers stronger compared to conventional trapping particles like polystyrene and also that the range of particles that can still be trapped in a single beam trap can be increased. Gaining stiffness in optical tweezing makes optical trapping a more versatile tool-box for a broader range of applications.

4.1 Introduction

Titania is abundantly studied in the literature for its importance in many fields such as catalysis (both as a catalyzer [1] and as a support [2]), in Grätzel solar cells as a semiconductor for conversion of light to electricity [3], in colloidal photonic crystals and as a paint pigment for its high refractive index [4–6]. Although there was scientific demand for colloidal titania in many areas, fast reaction kinetics of the titania precursors made the synthesis of highly monodisperse titania colloids difficult in a reproducible manner, until recently. Barringer et al. [7] and Jean et al. [8] reported synthesis procedures for monodisperse titania but their methods were not easily reproducible. Recently, Eiden-Assman [11], Yu et al. [12] and Jiang et al. [13] succeeded in producing monodisperse titania particles, which were more reproducible. Also after calcination the latter methods gave more spherical colloids with respect to the method of Barringer and Ring [9]. They all make use of the hydrolysis of titanium alkoxides and control their precipitation using a (non-ionic) surfactant. The method of Eiden-Assman is notable for its high particle yield compared to other methods and it is optimum for making particles of $\sim 1\mu\text{m}$ in size whereas the others give particles in the size range of 200 to 650 nm.

Seeded growth, well known for the growth of silica particles, is in general a reproducible way to obtain fine control of particle growth, which generally also helps to decrease the polydispersity of the particles [10]. In this chapter we show seeded growth of titania particles with amorphous titania starting from a crystalline core to come up with a core-shell structure with different but high refractive indices of core and shell.

This core-shell structure opens the way to tailor the refractive index of the core independently from that of the shell, which makes our particles useful candidates for photonic crystal applications. It was shown by Velikov et al. [14] that the L-stopgap width in *fcc* photonic crystals of high-index core and low-index shell particles was larger in comparison to the case of homogeneous particles of either material. It was also shown that a core-shell morphology could give additional control over the photonic stopgap characteristics like bandwidth, position and depth of the stopgap [14]. Here we present a way in which the refractive index of the shell can be tuned from 1.55 to 2.3 by manipulating the titania shell with silica incorporation and calcination steps, which yields structures with an anatase core and amorphous titania-silica shell with refractive index tunability of the shell.

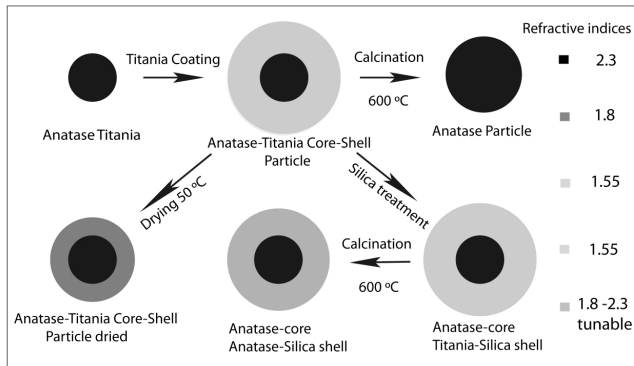
In addition to the above mentioned applications and properties of these core-shell structures, one reason we tried to synthesize these particles was because of their possible use in optical tweezers applications. Bormuth et al. [15] have shown that coated microspheres where the coating works as a kind of 'anti-reflection' layer can reduce the scattering forces and lead to stronger trapping. For high refractive index materials the scattering force, which scales with the square Δn^2 (Δn is the difference of the refractive index of the medium and the particle), dom-

inates and limits optical trapping. Note that the gradient force, which stabilizes the particle in a trap is to a first order approximation proportional to Δn . These effects result in an upper limit to where homogeneous high index particles of a certain size can still be trapped in a single beam trap [16]. However, having an 'anti-reflection' coating on high refractive index particles can make these particles trappable by reducing the destabilizing scattering forces. As illustrated in the second part of this chapter, calculations indicate that core-shell geometries with an index core of 2.3 and a low index shell of 1.8 would be optimal candidates to increase the trapping stiffness of micron sized particles within a single beam optical tweezer. According to such calculations these particles can be trapped twice as strong compared to the conventional polystyrene beads. This kind of improvement in the stiffness of the particles broadens the tweezing tool-box for biophysical applications.

In this chapter we present the synthesis and characterization of this desired particle system and in addition present trapping stiffness calculations obtained by our collaborators for these specially designed core-shell particles.

4.2 Experimental details

Preparation of Particles



Scheme 4.1. Schematic representation of the procedure for fabrication of core-shell titania structures. Note that all particles have a crystalline-titania (anatase) core. The particles are coated with amorphous titania and manipulated by heating and silica treatments.

A schematic representation of the procedure for fabrication of core-shell titania structures is given in Scheme 4.1. It is shown there that starting from a crystalline titania-core one can make various core-shell particles with different refractive indices of the shell ranging from 1.55 to 2.3. Heating steps cause shrinkage of amorphous titania. Calcination of the core-shell particle yields wholly crystalline titania particles with a larger size, whereas silica incorporation of these particles

limits shrinkage and keeps the density and refractive index low. The refractive index of the silica-titania shell depends on the amount of silica incorporated and the calcination time and temperature.

Crystalline titania cores were synthesized according to the procedure of Yu et al. with slight modifications [12]. For the synthesis two solutions were prepared, the first was a 0.46% (w/w) of titanium butoxide (TBT) (97%, Aldrich) solution in ethylene glycol, which also chelates with Ti and the second was an acetone solution of the surfactant Tween 20 (Aldrich), which was made with technical acetone at a concentration of 2.03 mM. The technical acetone used had a little amount of water for the reaction to start. In the case we used highly pure and thus dry acetone ~100 μ L water was necessary for 100 mL of acetone. Note that this tiny amount of water in acetone is crucial for realizing a successful spherical and monodisperse particle synthesis. 10-20 mL of the TBT solution was mixed with 100 mL of the acetone:Tween 20 mixture and agitated for 10 min, the transparent solution became milky white and the white precipitate was collected by centrifugation next day. Synthesis that did not turn milky after 10 min, mostly yielded high polydisperse and/or non-spherical particles. With this technique it is possible to synthesize anatase titania particles within the 230-650 nm range after calcination at 500 °C for 1 hour. The anatase core particles after calcination were dispersed in ethanol by sonication. To a 10 mL of this dispersion of 2.4 mg core particles 80 μ L of 0.1 M aqueous Lutensol ON50 (BASF) solution was added. In another 10 mL of ethanol 0.2 mL of TBT was added and the diluted titania precursor was mixed with the core particle dispersion. The mixture was sonicated for at least 20 minutes in a sonication bath during the reaction. This gave monodisperse titania core-shell particles with a total size between 700-1000 nm depending on the amount of the titania precursor and the seed particle concentration. The titania particles were collected by centrifugation and then dispersed in fresh ethanol without drying.

Ethanol used in this work (for the synthesis) was analytical grade and at least 99.7%. Also it was kept in the fridge at around 7°C prior to use.

Silica incorporation in the amorphous titania shell was made according to the procedure for composite particles described in Chapter 2, which basically involved silica synthesis under Stöber conditions in the presence of the anatase-titania core-shell particles. For the silica incorporation 1.1 mg anatase seeds were grown with 0.2 mL TBT in 40 mL of ethanol and after the centrifugation of the grown particles these particles were dispersed in 10 mL fresh ethanol without drying. 100 μ L TEOS was added to the dispersion of particles along with 0.2 mL of ammonia for (1) in Fig. 4.4b. Another synthesis with thicker titania shell particles and with 50 μ L TEOS yielded (2) in Fig. 4.4b.

Confocal Microscopy

For confocal microscopy measurements fluorescent rhodamine isothiocyanate (RITC) dye was added to the dispersion of the particles and the particles were centrifuged

afterwards to remove excess dye. Because the dye was only physisorbed to the particles, the particles were not washed more than twice.

Static Light Scattering

Static Light Scattering was performed with home-built equipment using a He-Ne laser as a light source (632.8 nm, 10 mW). The logarithm of scattering intensity data were plotted against the scattering vector $k=4\pi n\sin(\theta/2)/\lambda$, where n is the solvent refractive index, θ is the scattering angle, and λ the wavelength in vacuum.

4.3 Results and discussion

4.3.1 Synthesis and Characterization

In previous work (Chapter 2 and Chapter 3) we found that amorphous titania particles are very sensitive to drying; particles dried in an oven at 50 °C for 2 hours could be coated with silica under Stöber conditions which yielded core-shell particles [17]. However, particles treated with silica prior to drying formed homogeneously mixed composite $\text{TiO}_2\text{-SiO}_2$ particles [18]. The formation of homogeneously mixed composite particles proves that particles as-synthesized are porous and open to the access of the species added after the synthesis. The porosity difference between dried and non-dried particles was also observed by addition of a fluorescent dye to the dispersions of both types of particles [19].

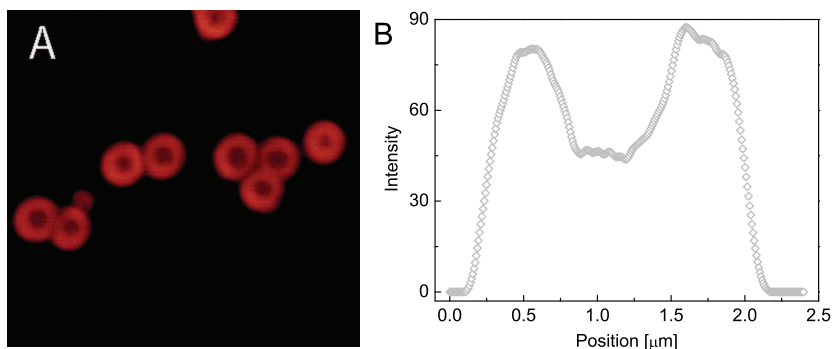


Figure 4.1: Confocal fluorescence microscopy images of (a) as-synthesized anatase core, titania shell particles after addition of fluorescent dye, where dye can only reach the shell (b) single particles profile of a particle in (a). [image size (a) = 13.25 μm \times 13.25 μm].

As-synthesized particles yielded fully dyed particles, whereas dried particles fluoresced only on the surface. We used this knowledge to image the anatase core and amorphous-titania-shell particles, where the dye could only penetrate down

to the edge of the anatase-core, which is dense due to sintering and does not let the dye go further in. This leads to a thick shell labeled with fluorescent dye as a sign of the core-shell structure. Fig. 4.1 shows a confocal microscopy image of the anatase-core, amorphous-titania shell particles labeled with RITC. Particles in Fig. 4.1a have an approximately 400 nm thick layer of amorphous titania shell, which is in agreement with successful seeded growth. Fig. 4.1b is a single particle profile of the sample in Fig. 4.1a and clearly shows the core-shell structure with a thick layer of titania shell, where the core is not labeled.

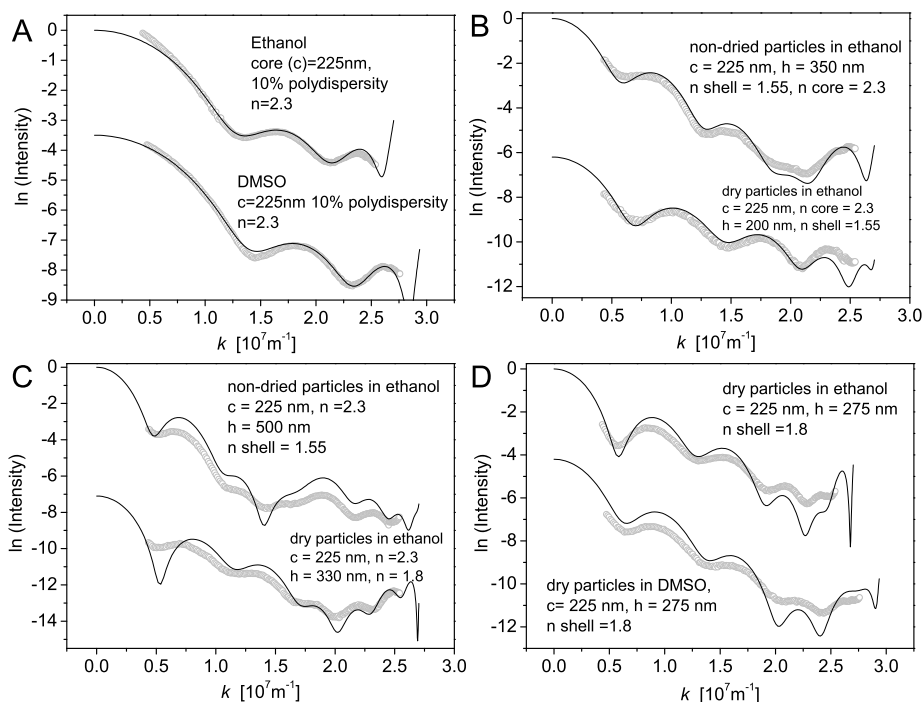


Figure 4.2: SLS experimental curves of the titania particles (symbols) in ethanol fitted to theoretical calculations of the full Mie solutions to the form factor (lines, offset for clarity). For the Mie solutions the polydispersity of the core was assumed to be 10 % and for all graphs the polydispersity for the shell was assumed to be 0 %. Core radius (c), shell thickness (h) and refractive indices (n) are shown on the graphs. (a) anatase titania particles used as seed particles to grow, (b) core-shell particles prior to drying (350 nm shell) and after drying (200 nm shell) in ethanol, (c) core-shell particles prior to drying (550 nm shell) and after drying (330 nm shell) in ethanol, (d) core-shell particles after drying (275 nm shell) in ethanol and in DMSO (k = scattering vector).

We did an thorough static light scattering (SLS) study of these particles; this method gives an easy way to estimate the size, polydispersity and the refractive index. The locations of the minima and maxima on the k -axis depend sensitively on the particle size and refractive index, whereas the depth of the minima gives

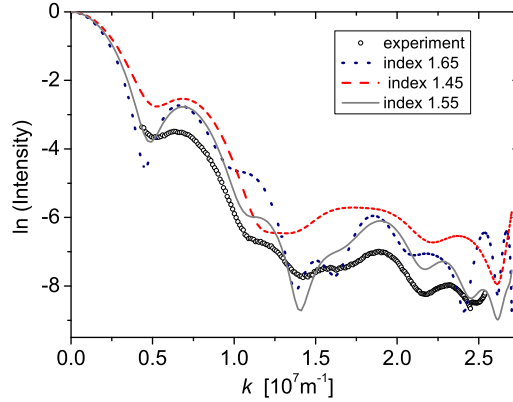


Figure 4.3: SLS experimental curves of the titania particles (symbols) in ethanol fitted to theoretical calculations of the full Mie solutions to the form factor (lines, offset for clarity). Core radius, shell thickness and refractive indices are shown on the graphs. Dried core-shell particles given in Fig. 4.2(c) and three different Mie solutions to the experimental data to give an idea about the accuracy of the refractive index assignment with SLS technique. The calculations with ± 0.1 differs a lot from the experimental curve and can not match the minima. The calculations with ± 0.05 index change are still off from the minima but we preferred to show ± 0.1 change for better visualization (k = scattering vector).

an estimate of the polydispersity. For the same material the number of minima increases with size [20, 21]. Fig. 4.2 shows the SLS graphs of titania particles. For some particles the SLS measurements were made in ethanol and in dimethyl sulfoxide (DMSO) to have more features because of a different refractive index contrast and to compare the data with each other for a better estimate of the parameters. Symbols in the graphs are the experimental data and lines are poly-disperse Mie calculations for the form factor. For the Mie solutions the polydispersity of the core was assumed to be 10 % as was found experimentally for the seed particles, shown in Fig. 4.2a. In core-shell morphologies the polydispersity for the shell was assumed to be 0 %. The anatase particles, that were used as seed particles to further coat with amorphous titania, had a size of 450 nm with 10 % polydispersity as shown in Fig. 4.2a. Size estimates of the anatase seed particles agree for both ethanol (refractive index $n=1.36$) and DMSO ($n=1.479$) with a particle refractive index of 2.3 of the core. TEM analysis for these particles also gave a similar result for the size (See Table 4.1). In Table 4.1, a decrease in the polydispersity is also observed with the particle growth. The literature value for the refractive index of anatase at 633 nm is 2.5 [22]. The value we find is slightly lower, probably due to some remaining porosity. From XRD analysis we know that the anatase core consists of nanocrystals with a typical size of 10 nm. Core-shell particles fabricated by coating the anatase seeds with amorphous titania were examined by SLS before and after drying. We have observed here that amorphous titania as-synthesized is highly porous. In our previous work we found that amor-

phous titania particles prior to drying were as large as $1.8 \mu\text{m}$ and became $1.3 \mu\text{m}$ when dried, as determined by static light scattering [18]. For this reason we expected the shell thickness before drying to be larger and the refractive index and the density to be smaller. This is confirmed in Figs. 4.2b and c, which show the SLS graphs for two examples of core-shell particles with unique features that helps to estimate the size and the refractive index accurately. Note also that the TEM analysis data and the SLS data (see Table 4.1) deviate for amorphous titania particles, which we attribute to the shrinkage of the amorphous titania in the TEM as an effect of drying under high vacuum and heating by the electron beam. Shrinkage of these particles under the influence of the electron beam was indeed observed during experimentation with TEM. The features in the SLS curves specific to size and refractive index of the spheres give the the opportunity of estimating the refractive index for both the core and the shell. For core-shell particles the core was taken to be 450 nm with a 10 % polydispersity, which were the values found for the core particles alone from TEM and SLS analysis. From the measurement given in Fig. 4.2b we found the thickness and refractive index of the shell prior to drying to be 350 nm and 1.55, respectively. The shell thickness decreased to 200 nm upon drying, whereas the refractive index increased to 1.8. For Fig. 4.2c the thickness of the shell prior to drying was found to be 500 nm with a refractive index of 1.55 and it became 330 nm upon drying with a refractive index of 1.8. For another dried particle system we made SLS measurements in DMSO and in ethanol to check for consistency at different index contrast. Fig. 4.2d shows SLS graphs of dried core-shell particles dispersed in ethanol and DMSO. The refractive index of the shell from both measurements was consistently found to be 1.8 with a 275 nm shell thickness. All these analyses agree on a refractive index of 1.55 for non-dried amorphous titania and a refractive index of 1.8 for dried and shrunken titania samples.

Table 4.1: Total diameter from TEM and SLS of the particles given in Fig.4.2 and Fig.4.4. Polydispersities of the particles are given in paranthesis.

Particles	2A	2B	2C	2D	4A(1)	4A(2)
TEM size [nm]	440 (9%)	715 (4%)	903 (2%)	850 (3%)	675 (4%)	1047 (3%)
SLS size [nm]	450 (10%)	850 (5%)	1110 (4%)	1000 (4%)	710 (6%)	1030 (4%)

To manipulate the refractive index of the shell we used a trick that we have demonstrated and explained in Chapter 2, where we made silica-titania composite particles by simple Stöber treatment of the non-dried titania. The porosity of the as-synthesized titanias makes it available for hydrolyzed silica precursors that condensed inside the pores. The amount of incorporated silica determines the properties of the final product. Fig. 4.4a shows an SLS graph of anatase core particles with a titania-silica composite shell (curve 2). It was expected that addition of silica, which is a low refractive index material, decreased the refractive index of the shell. The refractive index for the composite shell after drying was

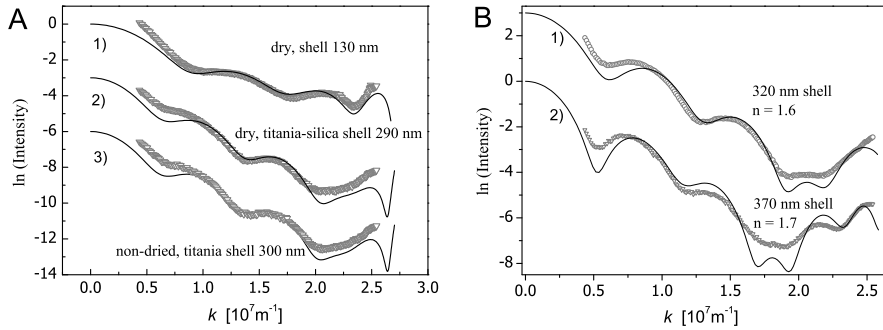


Figure 4.4: (a) core-shell particles (1) after drying with titania-only shell (130 nm shell), (2) core-shell particles with silica incorporated into the titania shell with a thickness of 290 nm size after drying, (3) the same particles prior to drying and without the silica incorporation, only titania shell of 300 nm size. (b) core-shell particles treated with silica (with composite shells) and calcined at 500 °C for 1 hour. The shell refractive index in (1) is 1.6 with a shell thickness of 320 nm and in (2) it is 1.7 with a 370 nm thick shell. All particles in (a) and (b) have the same cores with a 10% polydispersity. The refractive index for the anatase core is fitted as 2.3, for the non-dried titania shells as 1.55, for the dried titania shells as 1.8 and for the titania-silica composite shell as 1.55 ($k =$ scattering vector).

indeed found to be 1.55 from SLS data. This agrees with our prediction, as the refractive index of the shell decreased from 1.8 to 1.55 for the composite shell. It was also observed that incorporation of silica into the amorphous titania shell prevents particles shrinkage as a result of drying. Of course the absence of the shrinkage also contributes to a lower index of the final shells. For this particular case the non-dried shell was 300 nm (curve 3) and it shrank to 130 nm (curve 1) if silica was not added, however, its thickness was sustained at 290 nm after incorporation of silica as seen in curve (2) of Fig. 4.4a. The size difference for the dried titania and the dried composite shell, were also supported by the TEM analysis (see Table 4.1). Furthermore, if the anatase core, titania-silica composite shell particles are calcined in an oven at 500 °C the core will remain anatase with the same refractive index, however the shell will have an increment in its index due to the crystallization of the titania in the shell. The amount of silica incorporated, which is tunable by changing the amount of silica added, will affect the index of refraction. We prepared two samples with different silica content and calcined them at 500 °C for 1 hour. These particles were then dispersed in ethanol and examined with SLS. The indices of refraction for these particles were found to be 1.6 and 1.7 for (1) and (2) respectively in Fig. 4.4b. Based on this observation we think that by changing the silica content one can tailor the refractive index of the composite shell from 1.55 to 2.3, which is the refractive index of pure anatase titania.

The microstructure of the particles was also investigated by means of TEM. Fig. 4.5a shows a TEM image of anatase-titania core particles. Figs. 4.5b and c

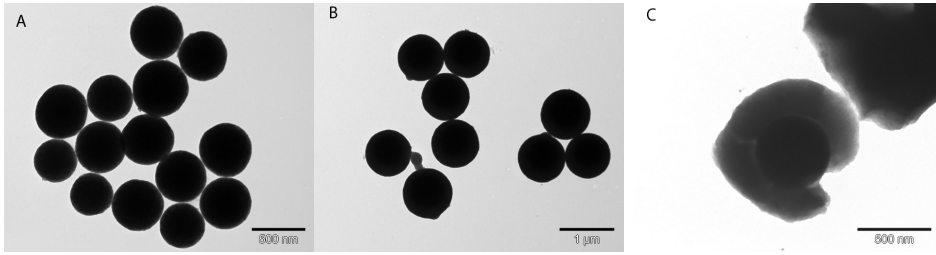


Figure 4.5: TEM images of (a) anatase core particles with a size of 450 nm and 10% polydispersity (b) core-shell particles of which the SLS curve is given in Fig. 4.2D, with a size of 970 nm in diameter, (c) a crushed core-shell particle after application of a mechanical force, which clearly shows the core-shell structure of the system.

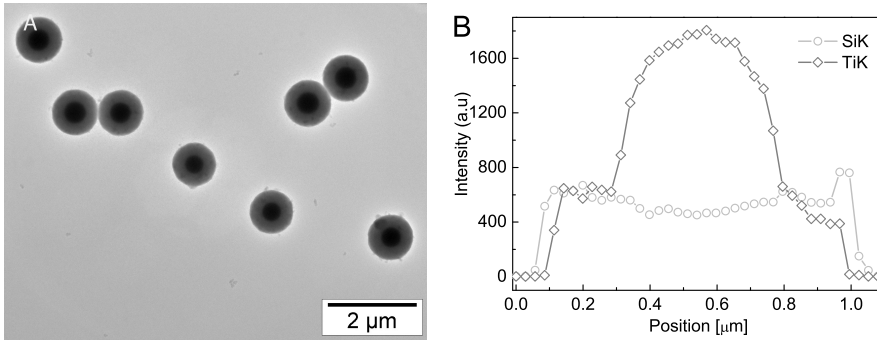


Figure 4.6: (a) TEM image of anatase core, composite titania-silica shell particles SLS data shown in Fig. 4.4a(2). (b) EDX line scans of Si-K and Ti-K lines through an anatase core, composite titania-silica shell particle given in (a).

show TEM images of core-shell particles with an anatase core and amorphous-titania shell that were broken core-shell particle after application of mechanical force. The sphericity of the titania particles was preserved and the polydispersity decreased by seeded-growth of the particles. With our technique it is possible to coat a thick layer of titania in one step, which can significantly decrease the polydispersity in one step. Fig. 4.6a shows an image of anatase core, titania-silica composite shell particles (same particles as in Fig. 4.4a(2)). Note that the core-shell structure is clearly visible in the TEM image whereas this was not the case for anatase core, titania shell particles (see Fig. 4.5b). This difference is due to the density decrease in the composite shell by addition of silica which increases the contrast between the core and shell. To prove that silica and titania co-exist in the shell and the core is much denser because of the crystallinity we performed an EDX analysis of the particles shown in Fig. 4.6a. It can be seen from the EDX line scan given in Fig. 4.6b that the shell has a composite structure because in the shell both silica and titania peaks exist. Titania in the middle of the line scan

increases in intensity proving that the crystalline titania core was denser than the shell. Silica peak exists on the shell and decreases in the middle of the line scan, which proves that the silica is only in the shell and it does not exist in the core of the sphere.

4.3.2 Particles as Tools for Optical Tweezing

Applications of single optical tweezers are limited for high index particles by the maximal force, which can be exerted on the trapped particle and the damage caused by high laser intensity in the focus, which leads to photo-toxic effects in cells. Achieving higher trap efficiencies at moderate intensities is only possible by using high refractive index particles. The gradient force, which stabilizes the particle in a trap, is to a first order approximation proportional to Δn , where Δn is the difference of the refractive index of the medium and the particle. However, the scattering force, which is the destabilizing factor for the trap, scales roughly with the square Δn^2 , dominates and limits optical trapping [16]. Consequently, there is a size limit for the high refractive index beads for which uniform microspheres still can be trapped in a single focused beam. For instance, titania particles (TiO_2) ($n = 2.3$) can only be trapped for diameters smaller than 280 nm. However, for such small diameters, there is no substantial improvement in trap stiffness compared to uniform polystyrene microspheres. A possible way for overcoming these problems is to use an 'anti-reflection'-like coating which decreases the scattering force, as hypothesized by Bormuth et al. [15]. Bormuth et al. [15] have also shown experimental evidence for an increase in the trapping stiffness of PS beads coated with an 'anti-reflection' silica shell.

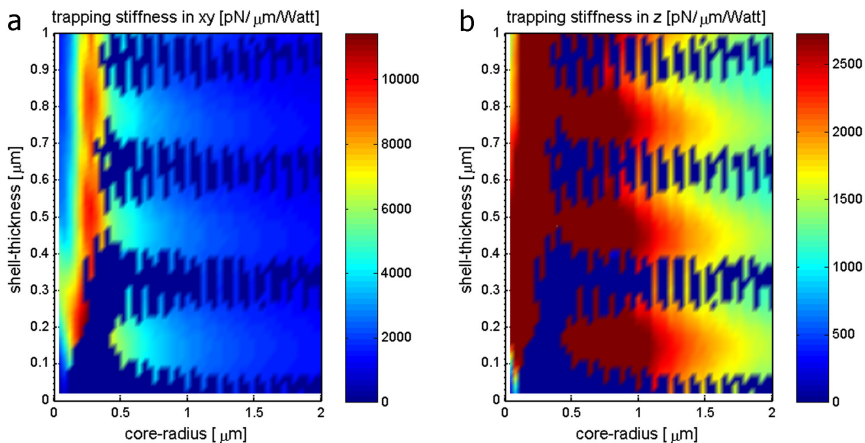


Figure 4.7: (a) Lateral trap stiffness and (b) axial trap stiffness as a function of particles diameter plotted against the diameter of the core diameter with an anatase-core, and an amorphous-titania-shell with the refractive indices of 2.3 and 1.8, respectively. Color version of the image is on page 123.

Theoretical calculations, made according to the method described in reference [16], showed that high refractive index particles coated with a lower refractive index material can be trapped even for larger diameters with a higher trapping efficiency than PS beads. For the calculations we chose a core with a refractive index of 2.3, which is the refractive index we can achieve for our crystalline-titania (TiO_2). Theory was used to design core-shell particles having optimal trapping properties for our high-refractive index beads. Based on geometric optics the ideal anti-reflective coating of such beads should have a refractive index of 1.8, which can be realized with an amorphous-titania shell. The calculations show that particles achieve at least twice the trap stiffness and maximum force compared to any PS beads.

The trap stiffness calculations based on the theory made for particles with a core refractive index of 2.3 and with a shell index of 1.8 are shown in Fig. 4.7 where Fig. 4.7a, and b are the trap stiffness in xy and z, respectively. It can be concluded from these calculations that our particles with a core diameter of 450-500 nm and a total diameter of 900-1000 nm are good candidates for a better trapping stiffness. Availability of these particles, which can subsequently be coated with a thin shell of silica as described in Chapter 2 allows one to use the rich chemistry of silica surface modification to further optimize the biophysical interactions with these spheres.

4.4 Conclusions & outlook

We reported an easy way of coating anatase particles with amorphous titania yielding monodisperse core-shell spheres without any use of glove box or nitrogen environment. This is also one of the first examples of seeded-growth shown for titania-on-titania particles. We have also shown that by manipulating the amorphous titania shell after the synthesis it is possible to tailor the refractive index of the amorphous shell. In principle, the manipulation of the refractive index can also be done for particles with no core-shell structure. Monodisperse titania particles with a high refractive index core and low index shell can be useful for photonic crystal applications and for optical tweezing of high refractive index particles. These crystalline core, amorphous shell titania particles can have approximately twice the trap stiffness compared to e.g. PS particles. This makes these particles interesting for tweezing experiments as it will increase the range of the possible experiments. Currently work is in progress to utilize the superior tweezing properties and strength of these core-shell spheres in biophysical experiments.

Acknowledgements

First of all, Anita Jannasch (Technical University Dresden) is thanked for the theoretical calculations on the core-shell particles, for the tweezing experiments and for assistance

in particle synthesis. Peter van Oostrum (Utrecht University, Soft Condensed Matter) is thanked for holography experiments on single particles for refractive index measurements and for calculations on core-shell particles and discussions. We also thank J. D. Meeldijk (Electron Microscopy Utrecht) for the assistance with the EDX measurements.

References

- [1] Hoffmann, M. R.; Martin, S. T.; Choi, W. Y.; Bahnemann, D. W. *Chem. Rev.*, **1995**, *95*, 69.
- [2] Valden, M.; Lai, X.; Goodman, D. W. *Science*, **1998**, *281*, 1647.
- [3] Oregan, B.; Grätzel, M. *Nature*, **1991**, *353*, 737.
- [4] Imhof, A.; Pine, D. J. *Nature* **1997**, *389*, 948.
- [5] Wijnhoven, J.; Vos, W. L. *Science* **1998**, *281*, 802.
- [6] Lodahl, P.; van Driel, A. F.; Nikolaev, I. S.; Irman, A.; Overgaag, K.; Vanmaekelbergh, D.; Vos, W. L. *Nature* **2004**, *430*, 654.
- [7] Barringer, E. A.; Bowen, H. K. *Langmuir* **1985**, *1*, 414.
- [8] Ring, T. A.; Jean, J. H. *Langmuir* **1986**, *2*, 251.
- [9] Holgado, M.; Cintas, A.; Ibisate, M.; Serna, C. J.; Lopez C.; Meseguer, F. *J. Colloid Inter. Sci.*, **2000**, *229*, 6.
- [10] van Blaaderen, A.; van Geest, J.; Vrij, A. *J. Colloid Inter. Sci.*, **1992**, *154*, 481.
- [11] Eiden-Assmann, S.; Widoniak, J.; Maret, G. *Chem. Mater.*, **2004**, *16*, 6.
- [12] Yu, H. K.; Yi, G. R.; Kang, J. H.; Cho, Y. S.; Manoharan, V. N.; Pine, D. J.; and Yang S. M. *Chem. Mater.* **2008**, *20*, 2704.
- [13] Jiang, X. C.; Herricks, T.; Xia, Y. N. *Adv. Mater.* **2003**, *15*, 1205.
- [14] Velikov, K. P.; Moroz, A.; van Blaaderen, A. *Appl. Phys. Lett.*, **2002**, *80*, 49.
- [15] Bormuth, V.; Jannasch, A.; Ander, M.; van Kats, C. M.; van Blaaderen, A.; Howard, J.; Schäffer, E. *Opt. Express*, **2008**, *16*, 13831.
- [16] van der Horst, A.; van Oostrum, P. D. J.; Moroz, A.; van Blaaderen, A.; Dogterom, M. *Appl. Optics*, **2008**, *47*, 3196.
- [17] Stöber, W.; Fink A.; Bohn, E. *J. Colloid Interf. Sci.* **1968**, *26*, 62.
- [18] Demirörs, A. F.; van Blaaderen, A.; Imhof, A. *Chem. Mater.*, **2009**, *21*, 979.
- [19] Demirörs, A. F.; Imhof, A. *Chem. Mater.*, **2009**, *21*, 3002.
- [20] Bohren, C.F.; Huffman, D.R. *Absorption and Scattering of Light by Small Particles*; Wiley: New York, 1983.
- [21] Kerker, M.; Farone, W.A.; Smith, L.B.; Matijevic, E. *J. Coll. Sci.* **1964**, *19*, 193.
- [22] Howard, C. J.; Sabine, T. M.; Dickson, F. *Acta Cryst.*, **1991**, *B47*, 462.
- [23] Nieminen, T. A.; Loke, V. L.; Stilgoe, A. B.; Knoner, G.; Branczyk, A. M.; Heckenberg, N. R.; Rubinsztein-Dunlop, H.; *J. Opt. A*, **2007**, *9*, S196.

5

A General Method to Coat Colloidal Particles with Titania

We describe a general one-pot method for coating colloidal particles with amorphous titania. Various colloidal particles such as silica particles, large silver colloids, gibbsite platelets, and polystyrene spheres were successfully coated with a titania shell. Although there are several ways of coating different particles with titania in the literature these methods are applicable for only one type of material. The present method is especially useful for giving the opportunity to directly cover the colloidal particles with titania without the use of any coupling agent for the titania precursor nor a pre-coating step. We could also produce particles with a smooth tunable thickness of titania with lower polydispersity whereas the literature methods have little control over the coating thickness. Monodispersity, gained by growth of the particles and the high refractive index of the titania make these particles potential candidates for photonic crystal applications. Here we also describe various ways of fabricating titania shells, which has been studied in the literature intensively for applications in electronics, catalysis, separations, and diagnostics. Note that this method grows amorphous shells on the particles and that needs to be heated to turn into crystalline titania.

5.1 Introduction

Colloidal titania (mostly crystalline) is a widely studied material for its unique optical, electrical, and chemical properties. It is well-known for photovoltaic [1–3] and photocatalytic [4, 5] applications, and it is used as a pigment [6], filler [7], and whitener in the paint, paper, cosmetic and food industries [8]. It is also used in photonic crystal applications of colloids for its high refractive index [9, 10].

Core-shell titania colloids are also a class of materials widely used in many fields of colloid and materials science. One goal for fabrication of core-shell structures of titania was producing titania shells [11, 12] by sacrificial removal of the core, which found applications from photonics to fillers, pigments and microencapsulation. Titania coated colloids are useful also to reduce the cost of pigment materials in coatings having the scattering properties of titania at the outer shell and by using a cheaper core than titania. Other applications of titania coating of colloids include changing the surface properties to obtain different particle interactions and changing the optical properties of the cores especially in case of metal cores [13, 14]. One notable application of core-shell particles with a titania shell was the fabrication of dielectric shell structures by converting the titania shell into perovskites, which have useful dielectric properties [15].

Coating of metal colloids with titania was shown by Caruso and Sakai et al. for gold and silver particles, respectively [16, 17]. The method of coating gold particles with titania reported by Caruso and co-workers is tedious and included several steps of coupling titania precursors to surfactants and finally to the surface [16]. Sakai et al. have shown an interesting way of coating silver particles in the presence of cetyltrimethylammonium bromide (CTAB), which also initiated the condensation of titania precursor [17]. In their work Sakai et al. also reported a red shift of the absorbance peak of the silver particles with a 5–10 nm titania shell, caused by an increase in the local refractive index.

In principle, many surfaces have a suitable chemical affinity to make direct titania coating possible, such as clay minerals, hematite, zirconia, zinc oxide and silica. However, there are few facile reports for coating even these colloids with titania, including the silica-titania couple. Although silica and titania are similar to each other in structure and it is easy to coat titania particles with silica with or without use of any surfactant [18], there are scarcely any methods reported to coat silica particles with a titania shell. Matijevic and co-workers reported a way of coating silica particles with titania, but synthesis conditions included several steps including heating and resulted in a thin, rough shell of titania [19]. Matijevic and co-workers also reported methods for coating zinc oxide and copper compounds with titania. These methods again included heating steps and could yield only limited thickness of titania layers [20, 21]. Coating methods of colloidal particles with titania in the literature almost always describes a thin titania layer that is not very smooth, which is probably due to the formation of the shell from smaller titania particulates [22–24]. This kind of synthesis usually causes aggregation

when a thicker coating is applied around the core [25].

The difficulties in a titania coating compared to for example silica are mostly caused by the fast and aggressive reaction kinetics of the titania precursors. This problem already makes it difficult to make homogeneous and monodisperse titania particles. However, these challenges can be overcome by using a surfactant, salt or a different solvent to slow down the reaction rate as was shown in recent reports [18, 26, 27]. The Stamm and Kawahashi groups have made notable contributions for coating polystyrene particles with smoother and thicker titania [28, 29]. Although they have lengthy reaction conditions like heating and refluxing for 20 h, they could reach a shell thickness of 130 nm with little aggregation and low surface roughness.

As seen from these examples the literature techniques are specific for coating one type of material with titania and they have several limitations. In this chapter we describe a more general method for coating different type of colloids with titania.

The procedure we present here to coat particles with titania is similar to that of Eiden-Assman et al. [18] in that it uses surfactant assisted precipitation of titania formed from the hydrolysis of a titanium alkoxide. We have modified it to an extent that it now allows one to coat seed particles of many different types. Our method is facile for its availability for post-synthesis modification of the titania shell like adding a fluorescent dye to label the particles for fluorescent microscopy, or different types of precursors for making a composite shell [30]. This technique also provides the flexibility of controlling the shell thickness from 10 nm to 250 nm at room temperature whereas in literature it is rare to find thick shells and they are hard to reproduce, especially when it consists of several growth steps or a layer by layer synthesis [31]. We think that our synthesis method is capable of coating any kind of ethanol dispersible sub-micrometer particles with titania of tunable thickness in a single step. We demonstrate this for the examples of silica, silver, gibbsite and polystyrene.

5.2 Experimental details

Particle preparation

Synthesis of Particles: Typical coating of a sub-micrometer particle was as follows: In a 10 mL dispersion of core particles in ethanol 80 μ L of 0.1 M aqueous Lutensol ON50 solution was dissolved. In another 10 mL of ethanol 0.1-0.2 mL of $\text{Ti}(\text{OC}_4\text{H}_9)_4$ (TBT) was added. The diluted titania precursor was mixed with the core particles dispersion by adding the ethanol solution of TBT to the dispersion of seeds and followed by vigorous shaking. The mixture was sonicated for at least 20 minutes in a sonication bath during the reaction. The mixture was left 2 hours to allow the reaction to go to completion. The titania-coated particles were collected by centrifugation and then dispersed in fresh ethanol without drying.

The absolute ethanol used in this work was kept in the fridge at around 7°C prior to use to slow down the condensation of the titania precursor. For details of the synthesis conditions and amounts of seeds added, see Table 5.1

SiO₂@TiO₂ particles were synthesized by using 600 nm RITC labeled silica particles, which were synthesized according to the procedure of van Blaaderen et al. [32]. For the titania coating of silica particles 80 μL of 0.1 M aqueous Lutensol ON50 (BASF) solution was added in to 10 mL of ethanol dispersion of silica particles. In another 10 mL of ethanol 0.2 mL of TBT was dissolved and the diluted titania precursor was mixed with the core particles dispersion. HF etching of the silica core was made with a 8% (v/v) HF solution.

Ag@TiO₂ particles were synthesized by using 250 nm Ag particles synthesized according to the procedure of Tao et al. [33]. These particles were initially dispersed in water but they could readily be dispersed in ethanol without any treatment. 80 μL of 0.1 M aqueous Lutensol ON50 solution was added to a 10 mL ethanol dispersion of silver particles. In another 10 mL of ethanol 0.2 mL of TBT was dissolved and subsequently this solution was mixed with the seed particles dispersion. The amount of titania precursor or the silver seeds was changed for in order to vary the titania shell thickness.

Table 5.1: Coating with Titania

particle	conc. of particle	Lutensol ON50 ^a	conc. TBT	shell thickness	
				dry	non-dried ^b
silica	1.86g/L	80 μL	10 mL/L	55 nm	110 nm
polystyrene	0.19g/L	80 μL	10 mL/L	250 nm	460 nm
polystyrene	0.38g/L	80 μL	7 mL/L	15 nm	42 nm
silver	0.23g/L	80 μL	7 mL/L	140 nm	-
silver	0.14g/L	80 μL	7.5 mL/L	220 nm	-
gibbsite	0.76g/L	80 μL	10 mL/L	35 nm	-

^a Amount of 0.1M Lutensol ON50 solution added for 20 mL synthesis solution.

^b Size of the particles prior to drying was obtained from SLS measurements, the spherical particles' dry size were obtained by TEM or SLS.

Cationic polystyrene (PS) spheres were prepared by surfactant free emulsion polymerization as described by Goodwin et al. [34]. The polystyrene particles were coated in a similar way as mentioned above. These particles were readily dispersible in ethanol. Seed particles were dispersed in 10 mL of ethanol and 80μL 0.1 M aqueous Lutensol ON50 (BASF) solution was added to this solution. In another 10 mL of ethanol 0.2 mL of TBT was dissolved. These solutions were mixed and sonicated.

Gibbsite platelets were prepared from aqueous aluminum oxide solutions by hydrothermal treatment at 85°C and purified by dialysis against demineralized water as described by Wierenga et al. [35] and transferred to ethanol by centrifugation.

For the titania coating to occur in a typical synthesis 80 μL of Lutensol ON50 solution was dissolved in a total 20 ml of ethanol. For this synthesis at least 0.1 mL of TBT was added. Concentrations lower than that did not yield condensation of titania in a reasonable time scale. An amount of TBT higher than 0.2 mL gave rise to aggregation and formation of secondary nucleates. Thus the coating thickness was tuned not through the TBT concentration but through the concentration of seed particles. With this method slight changes in the concentration of Lutensol ON50 amount are also possible. For example increasing the amount of Lutensol ON50 to 90 μL increased the reaction rate and also it decreased the limit of TBT for condensation from 0.1 mL TBT to a lower value ~0.07 mL TBT. Note that the drying mentioned throughout the chapter was done at 50°C in a vacuum oven.

Energy Dispersive X-ray (EDX) analysis and TEM images with high-angle annular dark-field (HAADF) detector were made by using a Philips Tecnai 20 electron microscope.

Confocal Microscopy

For confocal microscopy measurements the fluorescent dye rhodamine isothiocyanate (RITC) was added to a dispersion of the particles and the particles were centrifuged afterwards. Because the dye was only physisorbed to the particles, the particles were not washed more than twice. For confocal microscopy measurements the fluorescent RITC dye in the silica particles was excited with a 543 nm laser by using a Leica SP2 confocal microscopy equipped with a 63x objective NA 1.3.

Static Light Scattering

Static Light Scattering was performed with home-built equipment using a He-Ne laser as a light source (632.8 nm, 10 mW). The logarithm of scattering intensity data were plotted against the scattering vector $k=4\pi n\sin(\theta/2)/\lambda$, where n is the solvent refractive index, θ is the scattering angle, and λ the wavelength in vacuum [36].

X-ray Diffraction

The powder XRD measurements were performed with a Philips PW 1820 diffractometer with a Philips PW 1729 X-ray generator (Cu K_α radiation). A glass substrate was used to deposit the samples on.

5.3 Results and discussion

Coating Silica with Titania

In our previous work we found that amorphous titania particles are very sensitive to and modified by drying; particles dried in oven at 50 °C for 2 hours could be coated with silica under Stöber conditions yielding core-shell particles [37]. However, particles treated with silica prior to drying formed homogeneously mixed composite TiO_2 - SiO_2 particles [30]. The formation of homogeneously mixed composite particles shows that particles as-synthesized are porous and open to access of species added after the synthesis. The porosity difference between dried and non-dried particles was also demonstrated by the addition of a fluorescent dye to the dispersions of both types of particles [15]. As-synthesized particles yielding fully dyed particles, whereas dried particles fluoresced only from a surface layer. We used this knowledge to image the core-shell particles by labeling the amorphous-titania shell. Dye could only penetrate until it reached the core, which is denser and does not let the dye go further in. This would lead to a thick shell labeled with fluorescent dye as a sign of the core-shell structure.

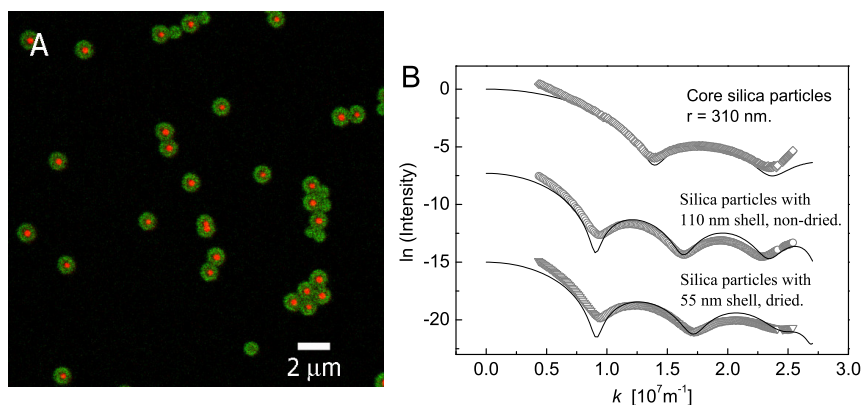


Figure 5.1: (a) Confocal microscopy image of RITC labeled silica particles coated with a titania layer labeled with FITC dye. The particles that look completely green are either second nucleation or particles that are not exactly in the same plane with the others, where only the shell is imaged. (b) SLS graphs of bare silica particles with a 5% polydispersity, 110 nm titania coated non-dried silica particles and particles after drying with a 55 nm titania shell from top to bottom, respectively. Image size of (a) = 26.91 μm × 26.91 μm.

RITC labeled silica particles with a 620 nm diameter were coated with titania. The titania coating of these particles was also labeled, but with FITC, to obtain contrast between the core and the shell. Fig. 5.1a shows a confocal microscopy image of the silica-titania core shell particles. The particles that look completely green are either second nucleation or particles that are not exactly in the same plane with the others, where only the shell is imaged. The coating thickness can be measured with SLS. The SLS graphs for these particles with and without the

titania coating is given in Fig. 5.1b. The symbols in the graphs are the experimental data and the lines are the full Mie calculations for the core-shell form factor. From the scattering data the polydispersity for the silica core was estimated to be 5%. The thickness of the titania shell is sensitive to drying and it decreases from 110 nm to 55 nm after drying with an increase in the refractive index of the shell from 1.55 to 1.8 (See Chapter 4).

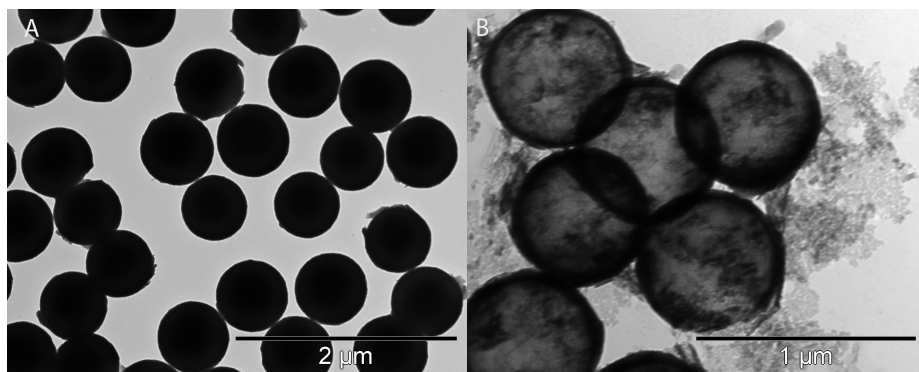


Figure 5.2: (a) TEM image of silica particles coated with titania, (b) TEM image of anatase titania shells after HF etching of Silica@Titania particles calcined at 500°C for half an hour.

Silica@Titania particles were also used to produce titania shells by selective etching of the silica core with HF. TEM images of Silica@Titania particles as-synthesized and of calcined Silica@Titania particles after etching with HF are given in Fig. 5.2a and b, respectively. The result is clear evidence that a titania coating was deposited on the particles.

Coating polystyrene with titania

We could also coat polystyrene (PS) particles successfully with titania. To show that we can tune the thickness of the titania shell here we show two extreme examples of thin and thick coating of cationic PS particles by changing the amount of titania precursor used per particle. Fig. 5.3a shows a typical confocal microscopy image of titania coated PS particles where the thick titania layer is fluorescently labeled. Fig. 5.3b is a TEM image of the titania coated PS particles found to be 1210 nm in diameter with 3% polydispersity. The original particles had a size of 770 nm. In our previous work we have found that amorphous titania particles that were as large as 1.8 μm prior to drying, shrank to 1.3 μm when dried, determined by the static light scattering technique [30]. Here we observe a similar shrinkage for the amorphous–titania coated particles. When the PS particles with a titania shell were calcined in an oven at 500°C for an hour the core burned away and the shells became crystalline. A TEM image of crystalline titania shells is shown in Fig. 5.3c and the corresponding XRD graph is given in Fig. 5.3d. The

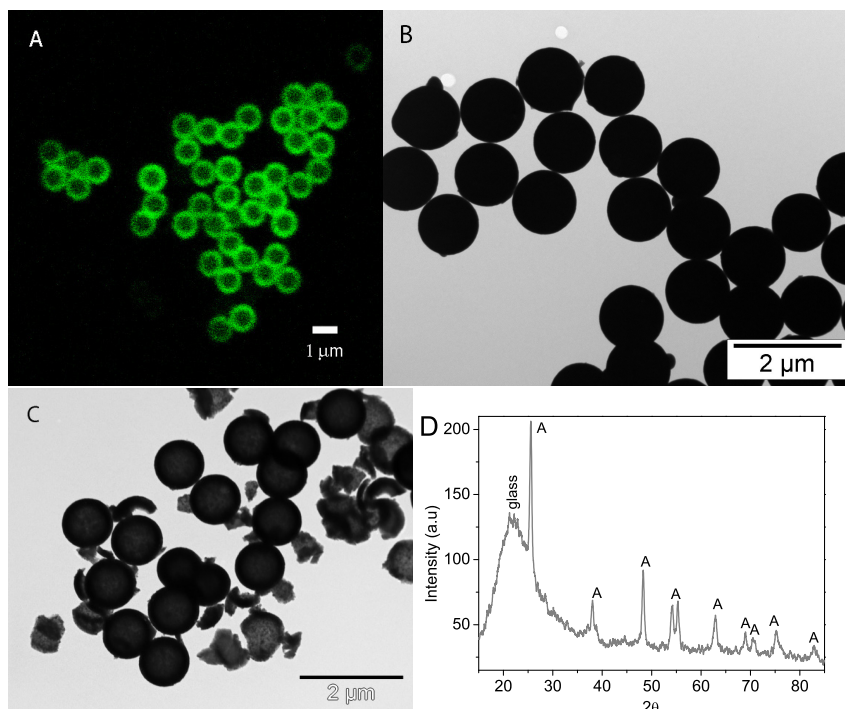


Figure 5.3: As-synthesized polystyrene core, titania shell particles (a) confocal microscopy image after addition of fluorescent dye, where dye can only reach the shell (b) TEM image of the particles shown in (a), (c) TEM image of crystalline titania shells after calcination of the titania-coated PS particles at 500°C, (d) XRD of the titania shells showing that the shell is anatase, peaks are denoted as "A" for anatase and the broad peak at around 20 is due to the glass substrate. [Image size of (a) = 15.01 μm \times 15.01 μm .]

XRD graph has the typical anatase peaks of titania. An SLS graph of these anatase shells is also given in Fig. 5.4c. This SLS graph proves that with this technique it is possible to make very monodisperse thick titania shells. It should be noted that the thick titania layer hinders the burning process of the PS core and this can be a reason for the bursting of some particles which can easily be seen from a TEM image of an uncleaned batch shown in Fig. 5.3c. However, it is also possible that a thicker shell is simply less flexible under heat stress this causes the break down.

The scattering features, specific to size and refractive index of both the material of the core and shell, give a chance of estimating a refractive index for the core and the shell. From SLS measurements, where we used the known PS refractive index of 1.59, we estimated the refractive index of the titania shell to be 1.55 prior to drying and 1.8 after drying. As shown in the SLS graphs in Fig. 5.4a and Fig. 5.4b it was possible to coat the PS particles with a thick and a thin layer of titania. In Fig. 5.4a(1), (2) and (3) an SLS graph of the original PS particles

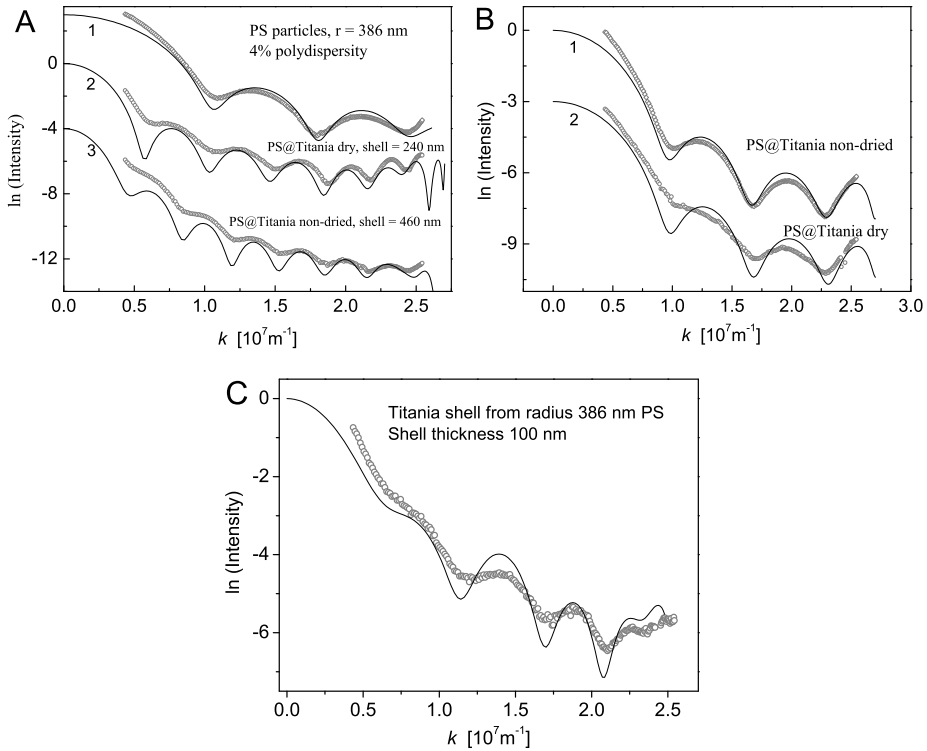


Figure 5.4: SLS graphs of PS particles coated with titania. Experimental curves of the particles (symbols) in ethanol fitted to theoretical calculations of the full Mie solutions to the form factor (lines, offset for clarity) (a) PS particles coated with a thick layer of titania, (1) belongs to the original PS particles with a radius of 386 nm, (2) the PS particles coated with a 240 nm thick titania shell after drying. (3) same particles as (2) with the titania shell prior to drying where the shell thickness amounts to be 460 nm. (b) SLS graphs of PS particles coated with a thin layer of titania which amounts to 42 nm for (1) particles prior to drying and 15 nm (2) for the dried particles. (c) SLS of crystalline titania shells with an estimated refractive index of 2.3 and thickness of 100 nm. Symbols are experimental data and the line is the corresponding Mie calculations.

is given together with the SLS graphs of the PS@Titania particles with a thick shell upon drying and prior to drying, respectively. The SLS graphs for the thin titania coated same PS particles are given in Fig. 5.4b(1) and (2) prior and after drying with a shell thicknesses of 42 nm and 15 nm, respectively. In the thick titania coating case we found a titania shell of 240 nm from SLS and 230 nm from TEM analysis. This thick titania shell blocks the dissolution of the inner PS by good solvents of PS. We tried to dissolve the core by using THF but the core was still not dissolved after several days of THF treatment. This experiment shows that although it is porous the thickness of the shell is preventing the dissolution of the core by slowing down the process to an impractical rate. However, for the

same particles coated with a thin layer of titania the dissolution of the cores was straight forward. In Fig. 5.5a a TEM image of PS@Titania particles with a 15 nm titania shell is given. These particles yielded nice and monodisperse amorphous titania shells upon dissolution of the PS core, which is shown in Fig. 5.5b.

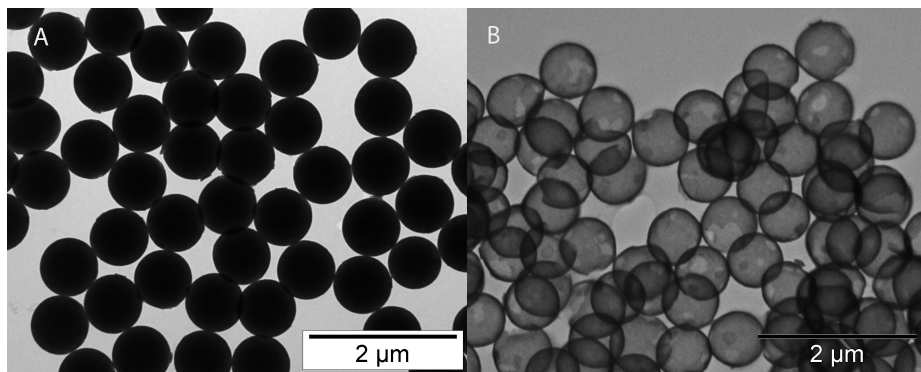


Figure 5.5: TEM images of (a) PS particles with thin shell of titania 15nm in thickness (b) Titania shells after dissolving the PS core with THF.

Coating metal oxides with titania

Next, we describe an example of titania coating on a metal oxide colloid, namely gibbsite platelets of 450 nm diameter. The titania coating on the platelets was 30 nm on the edges. The titania shell can be distinguished from the gibbsite core due to the density contrast of core and shell in the TEM image given in Fig. 5.6. Although the titania coating is visible in Fig. 5.6b the contrast with the gibbsite is a bit low. Therefore we analyzed the particles with EDX as well. On a single spot near the center of the particle EDX graph shows both peaks for titanium and aluminum, which are clear signs for the presence of titania and gibbsite, respectively. (see Fig. 5.6c) To show the fact that titania is coating the gibbsite platelet we did a line-scan at the edge of the particle in Fig. 5.6b. From the EDX line-scan given in Fig. 5.6d it is seen that the titanium peak starts before the start of aluminum peak and decreases as the aluminum peak shows up. The aluminum peak decreases approximately 30 nm after the titanium peak, which agrees with the titania shell thickness measurements. These features of the EDX line clearly show the core-shell structure of particles.

Coating a noble metal with titania

As an example of coating metal particles with titania we have fabricated silver core, titania shell particles starting from well-defined bare silver particles. Ag particles of 250 nm size and octahedral shape were successfully coated with a 220 nm thick titania layer in one step. A TEM image of the silver particles coated with titania is given in Fig. 5.7a. To show that the thickness can be tuned by chang-

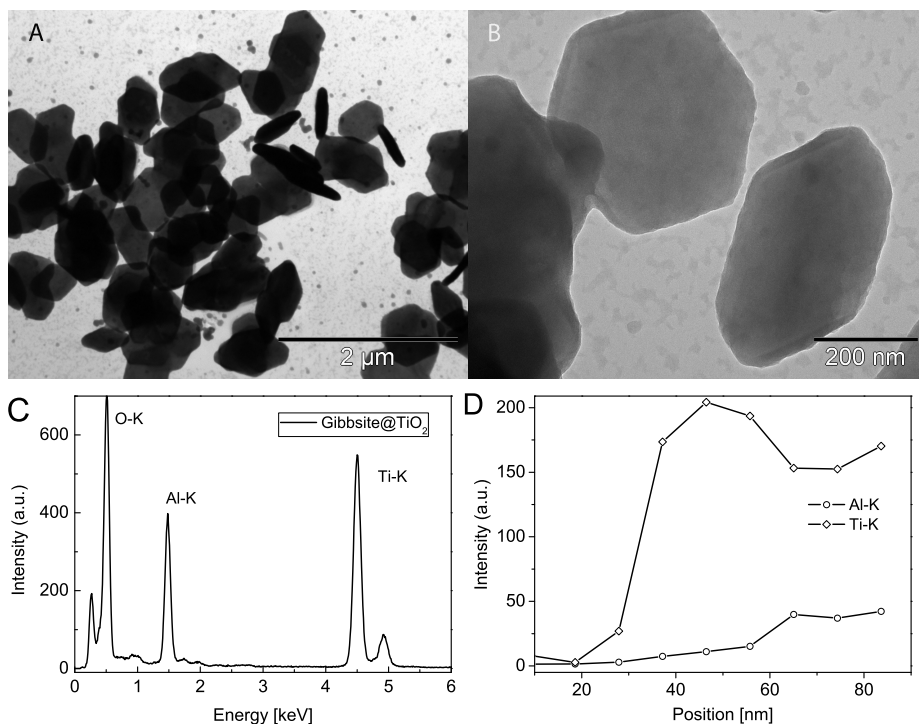


Figure 5.6: (a) Gibbsite platelets of 650 nm size coated with a 35 nm titania shell. (b) Zoomed image of a single gibbsite particle for better visibility of the titania shell. (c) EDX analysis on a spot at the particles in (b), which shows the presence of Al from the gibbsite and titanium from the titania, (d) EDX line-scan through the edge of the particle in (b), which clearly shows the core-shell structure.

ing the silver colloid concentration we tried the synthesis with a lower TBT:seed ratio. We obtained thicker shells for a synthesis where we used half of the seed particles compared the above example (See Table 5.1 for details). Note that the silver seeds we used were regular octahedrons and the facets of the core particles are visible in the TEM images. EDX analysis at the center and at the edge of a particle proves the core-shell structure. On a spot at the center of the particle both peaks for silver and titanium exists whereas at the edge only the titanium peak was observed (see also Fig. 5.7).

Since it is known that concentrated HNO₃ can etch silver by oxidizing it, we have tried to etch the core of Ag@TiO₂ particles with HNO₃. Although the etching works within a few seconds for non-dried particles (by completely leaving the dispersion transparent, which means that the non-dried titania is also etched away.), it took 1 day to partially etch the silver core of dried Ag@TiO₂ particles. This observation agrees with the results found when dissolving the PS core from coated particles. Additionally the surprising results in Chapter 3 about the Ag@BaTiO₃ particles that the silver core was not oxidized upon heating at 900°C

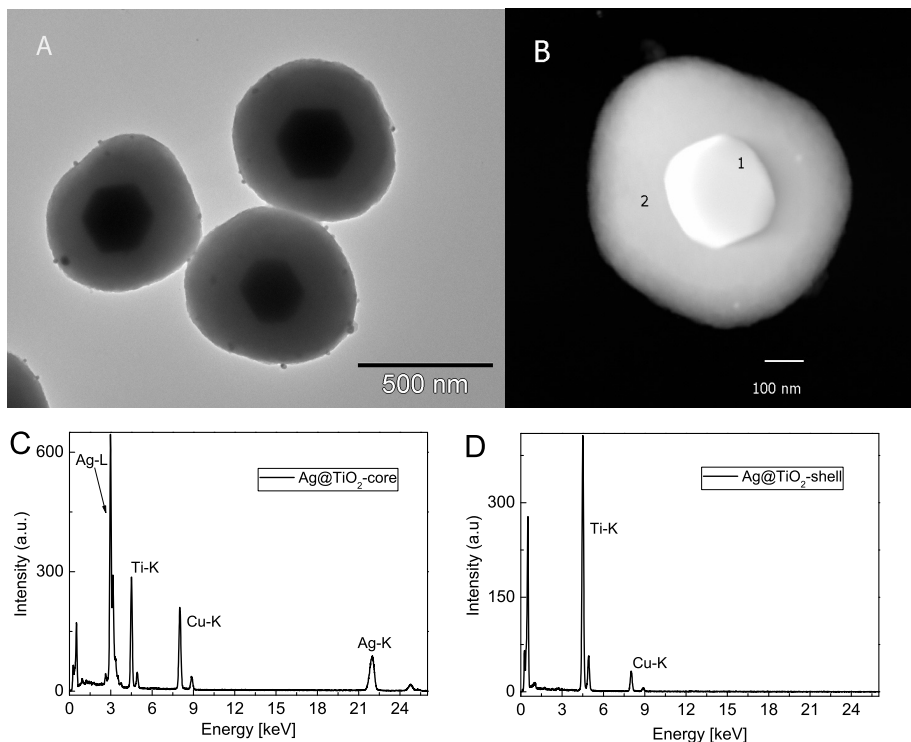


Figure 5.7: (a) TEM image of Ag@TiO₂ particles. (b) Transmission image of a single Ag@TiO₂ particle in HAADF mode, (c) EDX on a single spot in the core of the particle (shown in (b) as 1), which includes both elements of silver core and the titania shell. (d) EDX on a single spot on the edge of the particle (shown in (b) as 2), which has only titanium element of the shell. The copper signal is due to the substrate.

for 1 hour can be understood better with these results. (See Fig. 3.10 in Chapter 3 where no oxide peak, which is expected, was observed.)

5.4 Conclusions & outlook

We have developed an easy method for amorphous titania coating of colloidal particles with a controllable thickness. The coated particles are monodisperse in size and have a smooth surface. These colloidal particles are potentially important for photonic applications, especially because of the monodispersity gained by growth. This method offers the flexibility of tuning the thickness of the titania shell by changing the amount of seeds or by changing the amount of TBT added. Based on the methods we have described before it is also possible to make silica-titania composite shells for the particles shown here [30]. This new method can be applied to a broad range of sub-micron sized colloids, especially those that are

directly dispersible in ethanol. The amphiphilic and nonionic character of the surfactant, which defines the character of the synthesis, makes the method available for a broad range of colloid surfaces as demonstrated here for silica, silver, gibbsite and polystyrene. Heat treatment of the amorphous titania shells turns the shells in crystalline titania dependent on the temperature this is either anatase for 400-600°C or rutile for 800-900°C. Metal core, titania shell particles have importance in photonics and may find use in production of percolative capacitors by converting the titania shell to perovskites [15]. The growth mechanism of the titania on the colloids can be established by analyzing the competitive growth of a dispersion of titania spheres with a bimodal size distribution, this may give an idea, whether growth proceeds through a surface reaction-limited condensation or diffusion-limited condensation of the monomers. We are planning to observe this by growing titania on two different size PS or silica colloids similar to work made for silica [38].

Acknowledgements

The author thanks J.D. Meeldijk (Electron Microscopy Utrecht) for the assistance with the EDX measurements. Stephane Badaire (Utrecht University, Soft Condensed Matter) is thanked for the particle synthesis of the large silver particles and Maurice Mourad (Utrecht University, Van't Hoff Laboratory) is thanked for providing gibbsite platelets.

References

- [1] Grätzel, M. *Prog. Photovolt. Res. Appl.*, **2000**, *8*, 171.
- [2] Oregan, B.; Grätzel, M. *Nature* **1992**, *353*, 737.
- [3] Li, Y. X.; Hagen, J.; Schaffrath, W.; Otschik, P.; Haarer, D. *Sol. Energy Mater. Sol. Cells* **1999**, *56*, 167.
- [4] Bahnemann, D. W. *Res. Chem. Intermed.*, **2000**, *26*, 207.
- [5] Dillert, R.; Cassano, A. E.; Goslich, R.; Bahnemann, D. *Catal. Today* **1999**, *54*, 267.
- [6] Morris, G. E.; Skinner, W. A.; Self, P. G.; Smart, R. S. *Colloid Surface A* **1999**, *155*, 27.
- [7] Wen, J.; Mark, J.E.; *Rubber Chem. Tech.* **1994**, *67*, 806.
- [8] Meacock, G.; Taylor, K. D. A.; Knowles, M.; Himonides, A. *J. Sci. Food Agr.* **1997**, *73*, 221.
- [9] Imhof, A.; Pine, D. J.; *Nature*, **1997**, *389*, 948.
- [10] Wijnhoven, J. E. G. J.; Vos, W. L. *Science*, **1998**, *281*, 802.
- [11] Imhof, A.; *Langmuir*, **2001**, *17*, 3579.
- [12] Caruso, F.; Shi, X. Y.; Caruso, R. A.; Sussha, A. *Adv. Mater.* **2001**, *13*, 10, 740.
- [13] Liz-Marzan, L. M.; Giersig, M.; Mulvaney, P. *Langmuir*, **1996**, *12*, 4329.
- [14] Pastoriza-Santos, I.; Koktysh, D. S.; Mamedov, A. A.; Giersig, M.; Kotov, N. A.; Liz-Marzan, L. M. *Langmuir* **2000**, *16*, 2731.
- [15] Demirörs, A. F.; Imhof, A. *Chem. Mater.*, **2009**, *21*, 3002.
- [16] Mayya, K. S.; Gittins, D. I.; Caruso, F. *Chem. Mater.* **2001**, *13*, 3833.
- [17] Sakai, H.; Kanda, T.; Shibata, H.; Ohkubo, T.; Abe, M. *J. Am. Chem. Soc.*, **2006**, *128* (15), 4944.
- [18] Eiden-Assmann, S.; Widoniak, J.; Maret, G. *Chem. Mater.*, **2004**, *16*, 6.
- [19] Hsu, W. P.; Yu, R.; Matijevic, E. *J. Colloid Interf. Sci.* **1993**, *156*, 56.
- [20] Haq, I.; Matijevic, E. *Colloid Surface A*, **1993**, *81*, 153.
- [21] Ocana, M.; Hsu, W. P.; Matijevic, E. *Langmuir*, **1991**, *7*, 2911.
- [22] Lim, S. H.; Phonthammachai, N.; Pramana, S. S.; White, T. J. *Langmuir*, **2008**, *24*, 6226.
- [23] Li, G.; Bai, R.; Zhao, X. S. *Ind. Eng. Chem. Res.* **2008**, *47*, 8228.
- [24] Liu, L.; Dong, P.; Liu, R.; Zhou, Q.; Wang, X.; Yi, G.; Cheng, B. *J. Colloid Interf. Sci.*, **2005**, *288*, 1.
- [25] Li, G. C.; Zhang, Z. K. *Mater. Lett.* **2004**, *58*, 2768.
- [26] Yu, H. K.; Yi, G. R.; Kang, J. H.; Cho, Y. S.; Manoharan, V. N.; Pine, D. J.; and Yang S. M. *Chem. Mater.* **2008**, *20*, 2704.
- [27] Jiang, X.; Herricks, T.; Xia, Y.N. *Adv. Mater.* **2003**, *15*, 1205.
- [28] Agrawal, M.; Pich, A.; Zafeiropoulos, N. E.; Stamm, M. *Colloid Polym. Sci.*, **2008** *286*:593.
- [29] Shiho, H.; Kawahashi, N. *Colloid Polym. Sci.*, **2000** *278*:270.
- [30] Demirörs, A. F.; van Blaaderen A.; Imhof, A. *Chem. Mater.*, **2009**, *21*, 6, 979.
- [31] Caruso, F. *Adv. Mater.* **2001**, *13*, 11.
- [32] van Blaaderen, A.; Vrij, A. *Langmuir*, **1992**, *8*, 2921.
- [33] Tao, A.; Sinsermsuksakul, P.; Yang, P. *Angew. Chem. Int. Ed.* **2006**, *45*, 4597.
- [34] Goodwin, J. W.; Ottewil, R. H.; Pelton, R. *Colloid Polym. Sci.* **1979**, *257*, 61.
- [35] Wierenga, A. M.; Lenstra, T. A. J.; Philipse, A. P. *Colloid Surface A* **1998**, *134*, 359.
- [36] Bohren, C.F.; Huffman, D.R. *Absorption and Scattering of Light by Small Particles*; Wiley: New York, 1983.
- [37] Stöber, W.; Fink A.; Bohn, E. *J. Colloid Interf. Sci.* **1968**, *26*, 62.
- [38] van Blaaderen, A.; van Geest, J.; Vrij, A. *J. Colloid Interf. Sci.* **1992**, *154*, 481.

6

Soft Colloidal Dumbbells and Switching of Their Solid States

Colloidal hard dumbbells (pairs of colloidal spheres) were predicted computationally to form a plastic crystal and plastic glass at aspect ratios lower than 0.4 (Vega et al. *J. Chem. Phys.*, 1997, 107, 7 and Götze, et al. *Phys. Rev. E*, 2009, 65, 041503.). Although, phase behavior of soft dumbbells is not well studied, behavior of hard dumbbells can serve as a guide. Here, we present the realization of a plastic solid phase experimentally by tailoring the interactions from hard to soft, where screened Coulomb repulsions between the particles effectively decrease the aspect ratio. This solid system exhibits plastic behavior by enabling the dumbbell particles to freely rotate in the absence of an external field. However, the plastic solid phase forms ordered crystal phases upon applying an external electric field. The order can be induced by using an electric field and can reversibly be turned on & off. This switching property of our system can be important for photonic applications. We investigate the plastic crystal and ordered crystal phases of colloidal dumbbells by means of confocal microscopy and laser diffraction. Laser diffraction patterns with and without electric field also supports that order in the crystal can be switched by the electric field.

6.1 Introduction

The synthesis of spherical monodisperse colloids is by far the best established for most materials. A powerful strategy to arrive at more complex particles is to use spherical colloids as starting material to assemble them with complex geometries. A beautiful example of this approach is the anisotropic aggregates of spherical colloids with well controlled sizes, shapes, and structures that were first fabricated by using an oil-in-water emulsion [1]. Some of the more simple aggregates like dimers and the tetrahedral tetramers have shapes also found for certain molecules, bringing some to refer to these particles as 'colloidal molecules' [2]. Colloidal molecules have not only been proposed as model system but also drawn attention to their self assembled structures, as it has been predicted that crystals built up from particles with a lower degree of symmetry can be beneficial in achieving a full photonic band gap [3]. Colloidal dimers, or dumbbells as we shall call these particles in the rest of this chapter, are the simplest of the colloidal molecules but can be synthesized with high purity and high yield. Colloidal dumbbells can be synthesized either by forming protrusions on spherical polymer seed particles or by attaching two spherical particles for instance by destabilizing a dispersion of spherical particles followed by separation [4–6]. Colloidal dumbbells are interesting as a fundamental model system because their anisotropic shape makes rotational motion much more important than for spheres. The anisotropy is not large enough to form liquid crystal phases such as a nematic phase, but for certain aspect ratios it can result in a so-called plastic crystal phase. Whereas for liquid crystals there is no long range positional order, but some form of long range orientational order, plastic crystals are characterized by long ranged positional order but the absence of complete orientational order. Connected to this is the notion that for anisotropic molecules it is also possible that the rotational degrees of freedom have a glass transition separately from the translational degrees of freedom [7, 8]. We define the aspect ratio for our dumbbells, which could have 'overlapping spheres', as the length-to-diameter ratio $L^* = L/\sigma$, where L is the distance between the centers of the spheres and σ is the diameter of the (overlapping) spheres and takes values between 0 and 1 for the extrema of a single sphere and two touching spheres, respectively (see Fig. 6.1). The phase behavior of hard dumbbells was studied computationally by Vega et al. and Marechal et al. [9, 10]. In phase diagram of hard dumbbells Marechal et al. observe plastic crystals for aspect ratios below 0.4. For aspect ratios over 0.4 and at volume fractions over 0.65 an ordered crystal is predicted as the stable phase and for aspect ratios over 0.9 an aperiodic crystal phase is found, which was already predicted by Wojchickinski et al. for a 2D system [11].

In Fig. 6.1 the phase diagram of Marechal et al. is given where the aspect ratio is plotted against volume fraction (ϕ) and number density (ρ^*). The plastic crystal region observed for aspect ratios $L^* \leq 0.4$ was also divided into two regions shown with full and empty squares, which resemble stable face-centered-cubic

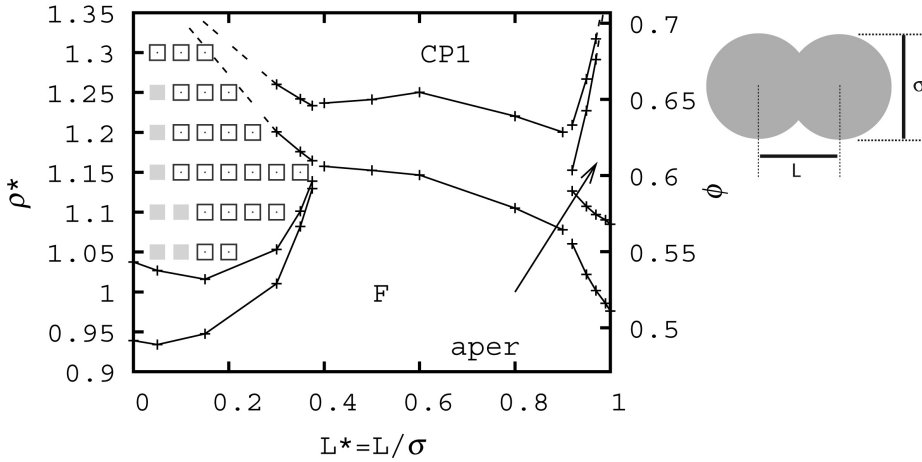


Figure 6.1: The phase diagram of hard dumbbells. 'F' is the fluid phase, 'CP1' is the ordered close-packed structure found for hard dumbbells and 'aper' is the aperiodic phase. The plastic crystal region for aspect ratios $L^* \leq 0.4$ is divided into two regions with full and empty squares. These resemble stable *fcc* and *hcp* phases, respectively. On the right L and σ is shown for a dumbbell particle, where L is the center-to-center distance of the dumbbell.

(*fcc*) and hexagonal-close-packed (*hcp*) phases, respectively. In the phase diagram an aperiodic crystal phase is also observed in 3D (region designated as *aper*) where both spheres that make up the dumbbell occupy triangular lattice sites while the particles are oriented randomly along different lattice directions. This phase is entropically favorable because it has many degenerate states. Note that recently Schweizer et al. [7] predicted the glass transition boundaries for hard dumbbells and the diagram has fluid, plastic glass (translational arrested), and double glass (translational and rotationally arrested) regions for similar aspect ratios to Marechal et al. [10].

Self assembly of dumbbell particles in 2D was studied by Liddell et al. [12, 13]. This group has shown the predicted aperiodic phase of high aspect ratio dumbbells [12]. In addition, they have also shown a plastic crystal (rotator) phase in 2D. However, their work did not focus on equilibrium structures of the anisotropic colloids as the solid phases were result of convective drying, a method in which packings are generated by a drying liquid, which exerts strong forces on the structures.

For hard dumbbells the aspect ratio is, besides the volume fraction, the determining factor for the phase behavior and defines the structure of the assembly. However, for particles that on top of the hard cores also interact through double layer repulsion, the range and thus aspect ratio of the repulsions can be tuned through the Debye-Huckel screening length, $1/\kappa$, in the solution. In this chapter we will be mostly concerned with solid phases of dumbbells interacting with a

soft potential, where the screening length was of the same order as the sphere size making up the dumbbells. In addition to gravity and the volume fraction of the particles we also influenced the crystallization with a homogeneous electric field with a frequency in the MHz range. Fields with such a high frequency only polarize the particle cores because the ions in the double layer do not have time to follow it. It was already shown by our group that such fields can help to grow larger crystals of single and bidisperse spheres [15, 16]. For our anisotropic dumbbell particles the electric field will not only introduce dipolar-like interactions between the spheres making up the dumbbells, but in addition will be able to align the anisotropic particles in the field direction [17].

Colloidal silica dumbbells synthesized according to the procedure of Johnson et al. [6] have a solid aspect ratio of 0.9 or less, which gives particles the opportunity to be aligned with an electric field. It is possible to lower the aspect ratio of the particles to 0.7 by growing additional silica layer (see Chapter 7), but to decrease the aspect ratio further is rather difficult because of aggregation and secondary nucleation. However, by making use of double layer interactions at high screening lengths, it is possible to reach low aspect ratios effectively. Previous work done in our group with polymethylmethacrylate (PMMA) particles has shown that interactions of charged particles can be tuned from hard to quite soft, with interaction distances of many microns in length, by putting the particles in an organic solvent [14]. The extension of this work has shown that this phenomenon is general for particles dispersed in a media with a dielectric constant ϵ between 4 and 10 [18]. Here we show that the same can be done with silica spheres by dispersing them in cyclohexylbromide (CHB) or in tetrahydrofuran (THF), which have dielectric constants of 7.9 and 7.2 respectively. In a dispersion of silica particles in CHB, Debye screening lengths $1/\kappa$ such that $\kappa R \approx 1$ are achievable. Long range repulsions due to long screening lengths in CHB and THF effectively increase the σ such that $L^* = L/\sigma$ values lower than 0.4 can be reached. This opens the way to explore the rich phase behavior of dumbbells more completely and to realize the plastic behavior experimentally. It should be remarked though that the phase behavior of soft dumbbells is not that well studied and the behavior of hard dumbbells can only serve as a guide.

Crystals of soft dumbbells are also expected to become important for photonic applications because an external electric field can be used to switch the structure quite dramatically as has already recently been demonstrated with magnetic fields and particles that interacted with soft potentials [19, 20]. Additionally, anisotropic building blocks for a self-assembled colloidal crystals are also promising for the fabrication of photonic band gap materials [21]. Li et al. computationally determined that it is easier to reach a full band gap structure for both *fcc* and body-centered-cubic (bcc) lattices of dumbbell particles [22]. The photonic band structure is strongly dependent on the direction of the dumbbell axis, which for our system can be controlled by the help of an external field.

In this chapter we present a plastic solid of soft dumbbells in addition to ordered crystal phase, which is the result of application of an electric field. The

order in the crystalline dumbbell system, as a function of the external electric field strength, is characterized with a nematic order parameter. Additionally, laser diffraction experiments on soft dumbbell solids with and without electric field were performed.

6.2 Experimental details

Particle preparation

1.3 μm silica particles were synthesized by seeded growth of Stöber [23] silica particles synthesized according to van Blaaderen et al. [24] with a rhodamine isothiocyanate (RITC) labeled, 350 nm core. Fabrication of dumbbells was done according to the procedure of Johnson et al. [6]. The silica dumbbells were coated with a layer of 3-(trimethoxysilyl)propyl methacrylate (TPM) under Stöber conditions prior to purification with density gradient centrifugation (DGC) technique. For the TPM coating 0.34 g silica particles ($\sim 40\%$ dumbbells mixed with single spheres) were dispersed in 15 mL ethanol and 1 mL ammonia (29% aqueous solution) was added to this dispersion along with 2 mL of TPM, the reaction mixture was allowed to react only for 2 hours. After TPM coating the silica particles were still water dispersible and purified with DGC to a 99 % of dumbbells. For the DGC we used 20% and 70% glycerol-water solutions. The purified dumbbells were dispersed in cyclohexyl bromide (CHB) with the help of poly(12-hydroxy stearic acid) (PHSA) stabilizer, which is used for the synthesis of PMMA particles according to the procedure of Bosma et al. [25]. 5-15 mg stabilizer was dissolved in 10 g CHB and this solution was used to disperse already dried silica dumbbells. Together with the TPM coating the stabilizer enabled silica particles to disperse in CHB. Silica without these treatments is not stable in CHB for the long term.

Confocal Microscopy

For confocal microscopy measurements the fluorescent RITC dye in the silica particles was excited with a 543 nm laser by using a Leica SP2 confocal microscopy equipped with a 63x objective NA 1.3. Images were taken below the sample perpendicular to the gravity, which is the xy plane. All images here are made in xy plane, where gravity (g) is along $-z$.

Particle tracking was achieved using the image processing language package IDL (RSI) and methods similar to those described by van Blaaderen et al. [26] and Crocker and Grier [27]. In addition, the particle tracking codes available at the web site of Eric Weeks were frequently used [28]. Particle dispersions were put in a square capillary (Vitrocom), which was coated with 3 nm of chromium, followed by 9 nm of gold on two opposite sides for applying an external electric field, as shown in Fig. 7.1 of Chapter 7. The electric field applied was an AC electric field with a frequency of 1MHz to avoid double layer polarization and electric currents.

6.3 Results and discussion

When the van der Waals attractions are ignored (because the particles are sterically stabilized and have long ranged repulsions) the particle interactions of soft silica particles can be described with a screened coulomb potential, which is given as follows:

$$\frac{U_{\text{Yukawa}}(r_{ij})}{k_B T} = \begin{cases} \frac{Z^2 \lambda_B}{(1 + \kappa \sigma / 2)^2} \frac{\exp[-\kappa(r_{ij} - \kappa \sigma)]}{r_{ij}}, & r_{ij} > \sigma \\ \infty, & r_{ij} < \sigma \end{cases} \quad (6.1)$$

where k_B is Boltzmann's constant, T the absolute temperature, κ is the inverse Debye screening length ($\kappa^{-1} = 1/\sqrt{8\pi\lambda_B c}$ for a number density $2c$ of a monovalent salt) and σ the particle diameter. Z here is the particle charge and $\lambda_B = e^2/4\pi\epsilon_0\epsilon_m k_B T$ is the Bjerrum length of the suspending medium with dielectric constant ϵ_m ; e is the elementary charge and ϵ_0 is the permittivity of vacuum.

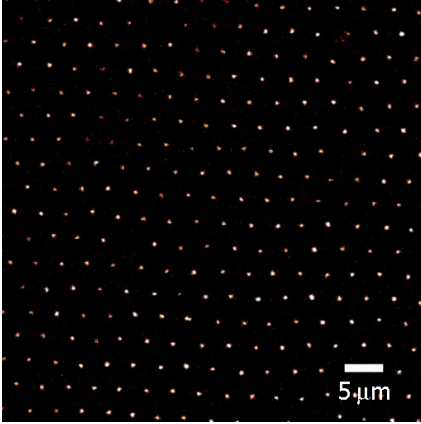


Figure 6.2: (a) Confocal microscopy image of RITC labeled single silica spheres of size $1.3 \mu\text{m}$ dispersed in CHB with a particle-particle distance of $3.5 \mu\text{m}$. Image size = $54.78 \mu\text{m} \times 54.78 \mu\text{m}$.

Dielectric constants $4 < \epsilon_m < 10$ are high enough for significant dissociation, which causes the particles to charge, but low compared to polar solvents such as water that the screening length can be made quite large. This increases the range over which repulsion experienced by the particles can lead to freezing of micron sized particles down to concentrations of less than a volume percent. Long range repulsion is a result of the κ term in the exponential, as κ gets smaller the potential becomes longer ranged. The particle-particle repulsion is directly visible in the confocal image given in Fig. 6.2 where the particle-particle distance is $3.5 \mu\text{m}$ for particles of $1.3 \mu\text{m}$ size, where we roughly estimated the $1/\kappa$ as $1.2 \mu\text{m}$. In the following we tacitly assume the interactions between the dumbbells can be well approximated by a screened Coulomb potential, as given in Eq. 6.1, originating at the spheres making up the dumbbells.

When colloidal silica dumbbells are dispersed in CHB they exhibit a similar long range repulsive behavior and as the dumbbells are anisotropic particles, the inter-particle repulsion enables them to freely rotate for sufficiently large screening lengths. When silica dumbbells have sedimented in CHB they display plastic solid behavior, where it is called a *plastic crystal* when the system has positional order but no orientational order and it is called a *plastic glass* when particles in the system are translational trapped but rotationally free. Fig. 6.3a shows a confocal microscopy image taken in the middle of the sample cell between the electrodes and at the bottom layer (with respect to gravity) of plastic solid phase of dumbbell particles. Only the two cores of the dumbbells are visible in the fluorescence image. Note that the dumbbells also rotate out of the plane. In the computer simulations the plastic crystal phase for hard dumbbells is expected for aspect ratios smaller than 0.4. Here the soft interactions enable us to decrease the aspect ratio effectively close to 0.4. For our system we determined the effective aspect ratio based on the confocal image given in Fig. 6.3b as 0.44. For determining the aspect ratio we assumed the inter-particle distance perpendicular to the field as the diameter σ and the core-core distance as the L .

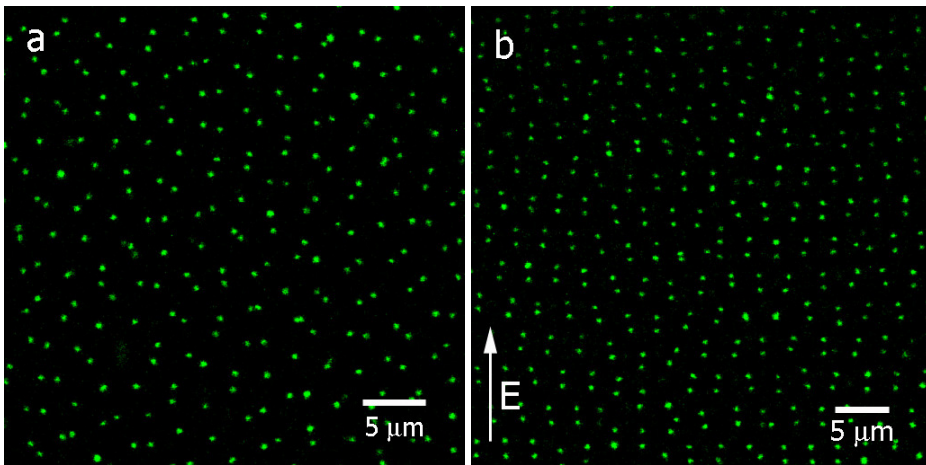


Figure 6.3: Confocal microscopy image of RITC labeled silica dumbbell particles dispersed in CHB (a) without any external electric field, (b) same sample with an external electric field of $117 V_{rms}/mm$ in the direction of alignment. Only the cores of the dumbbell lobes are visible. Image size (a) $=36.79\mu m \times 36.79\mu m$, (b) $=43.02\mu m \times 43.02\mu m$.

We describe the properties of the plastic solid phase below, but first show that the dumbbells can be oriented using an external electric field. It is already known from literature that as an electric field is applied on a dispersions of spheres a dipole moment is induced in the direction of the external field [29–31]. For the dumbbell particles a larger dipole moment is induced when the dumbbell particles

are oriented along the field direction. Thus, all the dumbbells become aligned along the field in the presence of a sufficiently strong electric field. The orientation of the dumbbells with the electric field is easily recognized in Fig. 6.3b. Even although dumbbell particles are not anisotropic enough to form nematic liquid crystal phases it is useful to characterize the orientational order induced by the field by the usual nematic order parameter defined for liquid crystals. Here we used this nematic order parameter as a measure of the local orientational order for dumbbell particles in both 2D and 3D. The two-dimensional nematic-order parameter S_{2d} for an N -particle system is defined as:

$$S_{2d} = \frac{1}{N} \left\langle \sum_{i=1}^N \cos(2\theta_i) \right\rangle \quad (6.2)$$

where θ_i is the angle between the i^{th} dumbbell major axis and the nematic director, which is for our case the electric field direction. This nematic-order parameter S_{2d} takes on an average value between 0 for a completely disordered (isotropic) phase and 1 for a perfectly oriented phase. We have used image analysis similar to Weeks and Grier [27, 28] to determine the positions of the fluorescent cores inside the spheres making up of the dumbbells. Centers of spheres belonging to the same dumbbell can be identified because their separation is less than the (known) diameter σ of the dumbbell. By determining the positions of the both fluorescent cores of the dumbbells we determined the orientation of dumbbells with respect to the electric field direction in 2D. For our plastic solid system seen in Fig. 6.3a we found the average of the nematic order parameter S_{2d} as 0.09 ± 0.04 for the case without an applied electric field and for the ordered crystal system seen in Fig. 6.3b an average of S_{2d} of 0.86 ± 0.02 was found in the presence of an 131 V_{rms}/mm electric field.

Particle tracking reproduction of dumbbells from Fig. 6.3a without any applied external electric field is shown in Fig. 6.4a; here out of plane-oriented dumbbells show up as single particles. The centers of mass of the dumbbell particles in Fig. 6.4a are shown in Fig. 6.4c, where the hexagonal order is observed with many defects. Particle tracking reproduction of dumbbells from Fig. 6.3 with an external electric field of 117 V_{rms}/mm is shown in Fig. 6.4b, for these particles the centers of mass are given in Fig. 6.4d, where the hexagonal order is also observed. It is important to study the centers of mass for the dumbbells because the centers of mass are expected to have 3D long ranged order for a plastic crystal, while the bond order should not be long ranged.

We have also calculated the two-dimensional orientational bond order parameter (ψ_6) for the plastic solid and ordered crystal systems. For this calculation we determined the centers of mass for the dumbbells and used these as the coordinates of the particles. The two-dimensional orientational bond order parameter ψ_6 is defined as follows:

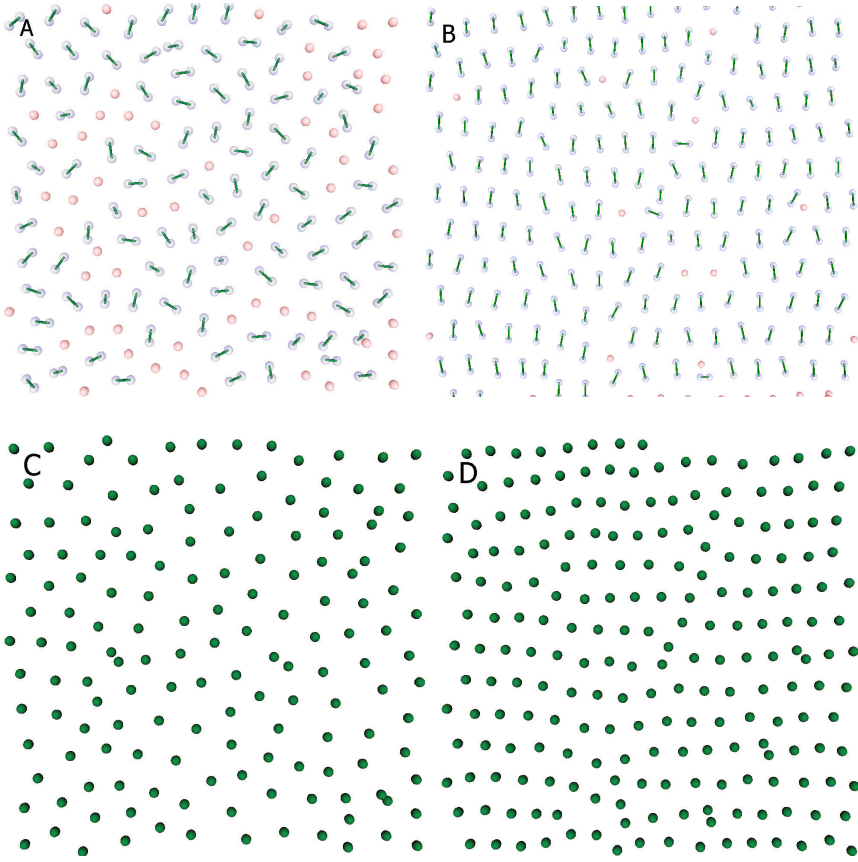


Figure 6.4: Computer generated reproduction of the dumbbells in CHB from Fig. 6.3 (a) without any applied external electric field, single particles are oriented out of the plane (b) with an external electric field in the direction of the induced alignment (single particles (red) are dumbbells oriented out of the plane). (c) center of masses of the dumbbell particles without a field, (d) center of masses of the dumbbell particles in the case of an applied field, Image sizes (a,c) $\sim 36.79\mu\text{m} \times 36.79\mu\text{m}$ (b,d) $\sim 43.02\mu\text{m} \times 43.02\mu\text{m}$.

$$\psi_6(\mathbf{r}_i) = \frac{1}{N} \sum_{j=1}^N \exp[6i\theta(\mathbf{r}_{ij})] \quad (6.3)$$

where the summation j runs over the N nearest neighbors of particle i , $\theta(\mathbf{r}_{ij})$ is the angle between the bond-vector connecting the particles i and j and an arbitrary axis. $|\psi_6|$ is ~ 0.4 for a typical dense fluid and increases to ~ 1 , for hexagonally ordered perfect crystal. For the finite systems of our 2D image analysis (images

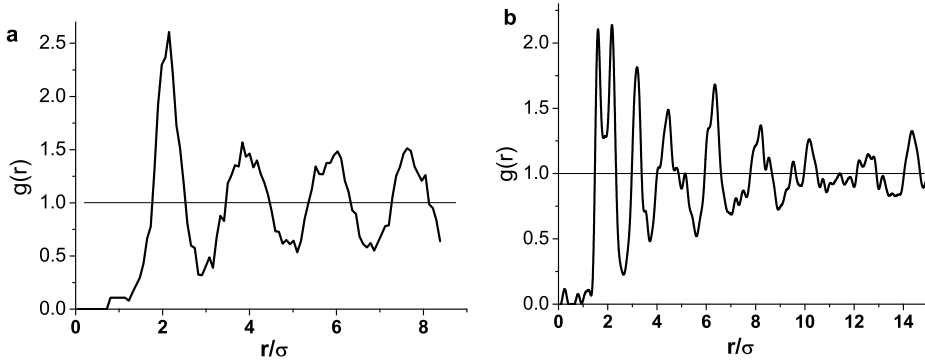


Figure 6.5: Two-dimensional radial distribution function for the dumbbell centers of mass (a) without any external electric field for plastic crystal phase, (b) for the ordered crystal phase with an external electric field. The split peak is because of the difference in particle-particle distances in x and y -axis (a dumbbell is elongated along y). σ is the diameter for a lobe of dumbbell.

given in Fig.6.3) we have found the $|\psi_6|$ as 0.57 for the plastic solid system and 0.65 for the ordered soft crystal system. From these results and also taking into account that the system is soft, it can be concluded that with and without the field the system is solid. For the plastic solid phase it is hard to conclude whether it is crystalline or glass. Although 0.57 is higher than the fluid limit of 0.4 for the hard sphere fluids, it is lower than the hard sphere limit of crystallinity of ~ 0.7 [33], which can also be considered as a result of the softness. For the ordered crystal phase the bond order parameter 0.65 is enough to conclude the crystallinity considering the defects and softness of the system. In addition to that the images were taken 10-20 minutes after the electric field was turned on and this may not be enough for a better crystallinity and order of the system. Furthermore, the anisotropic shape of the dumbbells distinguishes the inter-particle distances in x and y axes of the xy plane and this anisotropy also decreases the bond order parameter. With these arguments it can be concluded the system with the electric field is crystalline.

Therefore, the two-dimensional radial distribution function for the dumbbell centers was calculated for the plastic solid and ordered crystal phases, as given in Fig. 6.5. The radial distribution function for the plastic solid phase has no significant crystalline features but this may be a result of two-dimensional analysis. The radial distribution function of the ordered crystal system has clear crystalline features, with a doublet peak at $2r/\sigma$. This doublet peak is due to the difference in inter-particle distance in x and y axes for the ordered-crystal system due to the elongated shape of the particle.

We used image analysis and tracked the positions of the fluorescent cores inside the dumbbells to find the orientation of dumbbells with respect to the electric field direction in 3D as well. The orientation of the dumbbells in 3D is given by an

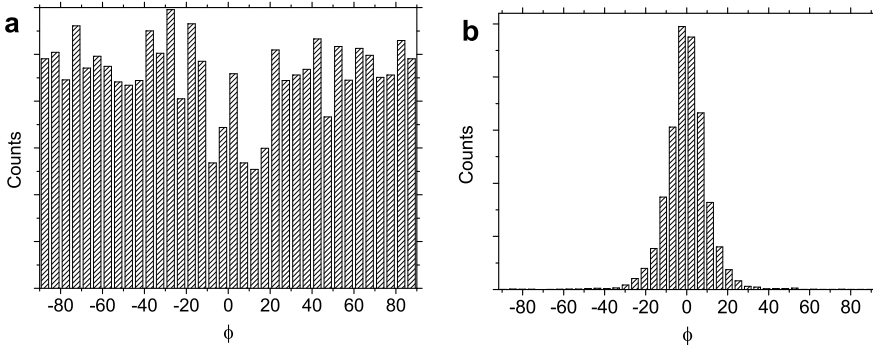


Figure 6.6: Three-dimensional analysis: Orientation of the dumbbell axis with respect to the electric field direction where ϕ is the angle between the electric field and the dumbbell axis (a) in case of no field, (b) in case of a field of $106 \text{ V}_{\text{rms}}/\text{mm}$, which aligns the dumbbells.

angle ϕ , which is the polar angle between the dumbbell axis and the electric field direction, where electric field is along z -axis and the dumbbell axis is the line that passes through the centers of the spheres of the dumbbell. Here ϕ takes on a value within the range $-\frac{\pi}{2} \leq \phi \leq \frac{\pi}{2}$. In Fig. 6.6 we have plotted the number distribution of the dumbbells with respect to ϕ . It is clear that when there is no electric field applied the particles are randomly rotating so that at any instant they are equally oriented in every direction (see Fig. 6.6a) and when an external electric field is applied particles get oriented along the field direction and populate in a narrow ϕ region (see Fig. 6.6b).

The nematic order parameter in 2D considers only the dumbbells in the xy plane and ignores the ones out of this plane. As it is observed in Fig. 6.4a without an electric field a significant amount of the dumbbells are out of the plane. For better statistics it is necessary to find the 3D nematic order parameter. Similar to the 2D case, order induced by an external electric field can be measured in 3D by using the three-dimensional nematic order parameter (S_{3d}) for dumbbell particles, which is defined as follows:

$$S_{3d} = \frac{3 \langle \sum_{i=1}^N \cos^2 \phi_i \rangle}{2N} - \frac{1}{2} \quad (6.4)$$

where ϕ_i is the angle between the i^{th} dumbbell axis and the electric field direction. From the particle tracking analysis we have found the coordinates of the dumbbell lobes and the ϕ_i for all the dumbbell particles. 3D analysis of 1494 particles gave an order parameter S_{3d} of 0.864 ± 0.006 for an electric field of $106 \text{ V}_{\text{rms}}/\text{mm}$. When no electric field was applied particles were randomly oriented which gave an order parameter S_{3d} of 0.00 ± 0.02 calculated for 570 dumbbells

as theoretically expected for a completely randomly oriented phase of the dumbbells. The volume fraction of the soft dumbbell solids was estimated to be 6% in both cases.

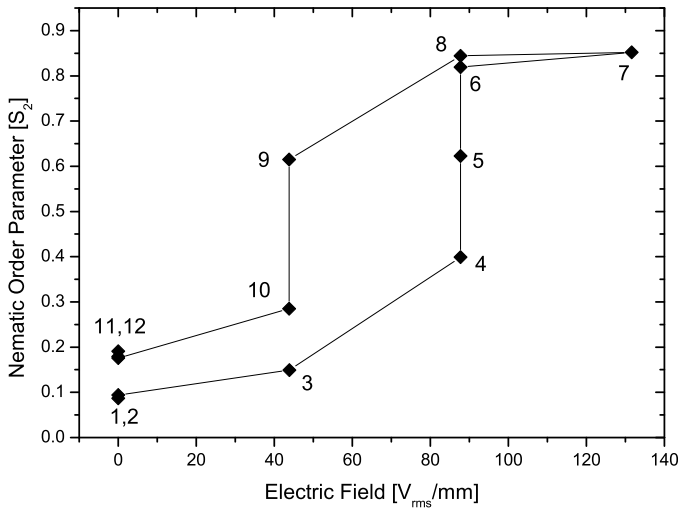


Figure 6.7: (a) Nematic order parameter (S_{2d}) for the dumbbells as a function of electric field. Numbers are showing the data points in time. The graph clearly shows a hysteresis, which means that order induced by the electric field relaxes back to the non-ordered state within a longer time interval. The points from 1-12 designate the time steps of 10, 47, 57, 65, 85, 123, 160, 196, 232, 268, 309, 319 sec.

Alignment of the particles with an electric field was reversible and could be performed infinitely many times. As the field is turned off, induced order by the electric field was observed to decay. However, we observed that the time response of the dumbbells to an increasing field and a decreasing field was not the same. We increased and decreased the field strength in steps while observing the particles in a 2D plane. From the image analysis of this data in time we have calculated S_{2d} as a function of the applied field strength. The plot of nematic order parameter S_{2d} with respect to electric field strength is given in Fig. 6.7, where hysteresis between the relaxation and alignment of the particles with the switching of the field arise is clearly present. This hysteresis is a result of the time difference that it takes to orient the particles with a field as compared to the clearly slower relaxation of the particles to disorder when the field is turned off. Note also that the system was not fully relaxed to orientational disorder at the last (12th) step. The nematic order parameter S_{2d} at this step is as high as 0.18 after 1.3 minutes, which is the time it took us to decrease the field in steps down back from the oriented state. Clearly the relaxation time was even longer than 25 seconds, which is the time that corresponds to the last step of the plot in Fig. 6.7.

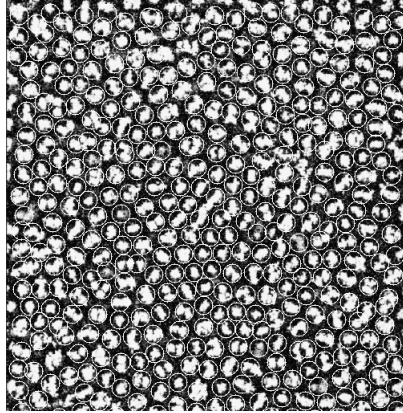


Figure 6.8: Plastic solid phase of particles observed over 1 minute of time and the trajectories of the particles were shown by superimposing all the images taken over this time at the same plane. Particles form mostly hexagonal structures whereas they span a region due to Brownian motion and rotation in time.

The positional order in the plastic solid system was also followed in time in 2D. To visualize this, confocal microscopy images taken from the same plane at different times were superimposed to show the hexagonal ordering of the particles during 1 minute with 1.6 second intervals and to also demonstrate the particles did not have any long time self diffusion, but were free to rotate on lattice positions. The resulting image is given in Fig. 6.8. Dumbbell particles indeed were found to be localized while rotating over all orientations. The circles in the image represent the lattice sides, which could be identified for most particles even although they rotated freely and moved around their average position because of the softness of the confining potential.

One other parameter that demonstrates the degree of order in the plastic solid phase is the density of the particles in the gravity direction (z -axis). The particle density in a plastic crystal stack is shown in Fig. 6.9 as a function of height in the stack. Clearly, the system is strongly layered. The stack is formed of 6 layers where the bottom 4 layers form a solid and the top layers stay fluid. The density modulation inside the stack, which forms layers, show that the dumbbells in the plastic solid exhibit positional order along z -axis. The steepness of the first peak is due to the bottom glass wall and following peaks decrease gradually as a function of pressure as the height increases. The density modulations indicate some degree of order such that the stack is a solid state, however, as the particles density does not fall to zero after the 2nd layer is evidence against the crystallinity of the system.

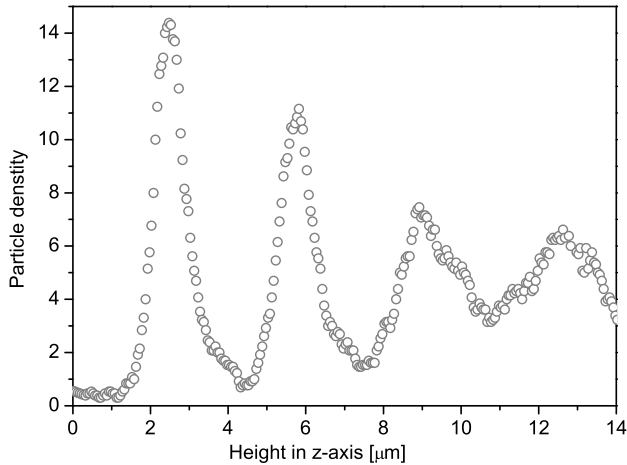


Figure 6.9: Particle density as a function of height in a plastic solid stack without an electric field.

6.3.1 Laser diffraction of soft dumbbell solids

Soft interactions in assemblies of anisotropic particles can be interesting for photonic applications. To show these possibilities, but also to characterize our 3D order on a significantly shorter time scale than is possible with taking 3D confocal data sets, we performed laser diffraction on our soft dumbbell system. In this particular case the soft dumbbells had a lower inter-particle repulsion. However, soft interactions were still present for the particles to freely rotate and align with the field. In such a dumbbell system the lobes of the dumbbells are the scatterers and when no electric field was applied the particles were subject to free rotation, under this condition the position of the dumbbells had a fluid like behavior. However, when an electric field was applied all the dumbbells became oriented and the particles formed an ordered crystal. The diffraction pattern of the soft dumbbell particles is shown with and without the external electric field in Figs. 6.10a and b, respectively. Applying an electric field restricts free rotation of the scatterers and keeps them ordered, which is the reason for the appearance of the hexagonal Bragg spots. In the case without a field the diffraction pattern resembles that of a fluid phase as seen in Fig. 6.10b, which is due to free rotation of positional trapped dumbbells. The free rotation of the particles is also observed from the dynamics of the speckles that show fluctuations in position and intensity. One useful feature of this soft assembly is that the diffraction pattern changes as a function of electric field.

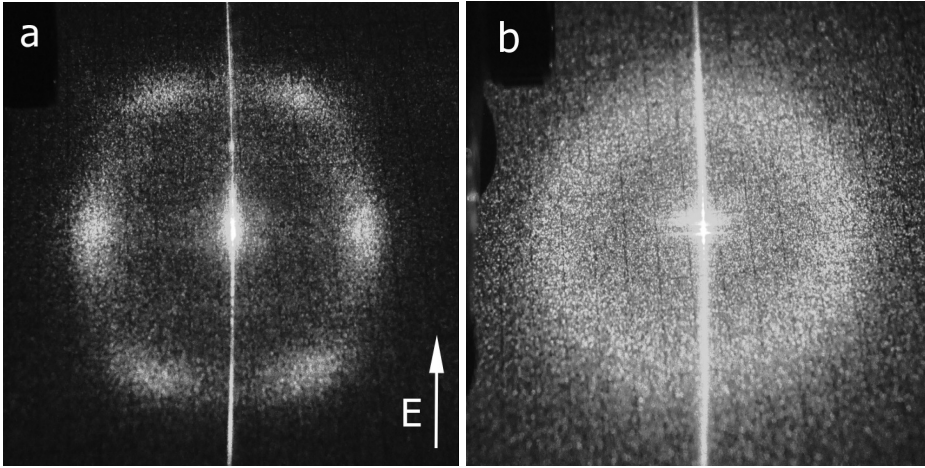


Figure 6.10: Laser diffraction patterns of soft dumbbell solids (a) in an electric field and (b) when the field is turned off.

This transition could be induced many times (more than 20) and had a relaxation time of 5-10 minutes. We observed the hysteresis mentioned in Fig. 6.7 here as well. The relaxation of the hexagonal pattern to a ring takes significantly more time than converting the ring pattern back to the hexagonal one. Note that the hexagonal pattern in Fig. 6.10a is elongated in the field direction. We think that it has two reasons; one is the dumbbell lobes, in the field direction are spaced closer to each other than the lobes of two adjacent dumbbells and the other reason is the dipolar attraction of the dumbbells in the field direction, which decreases the spacing between the dumbbells along the field direction.

6.4 Conclusions & outlook

We report the first experimental realization of plastic solid behavior of low aspect ratio colloids in three-dimensions, which was predicted previously for hard sphere dumbbells by simulation. Soft interactions make crystallization easier compared to hard systems and could also be used for tuning the effective aspect ratio of the particles. Soft interactions also enable the manipulation of the order in the crystals by an external electric field by giving the dumbbells enough space for free rotation. The possibility of tuning the order by an external electric field is certainly very interesting for photonic applications. For instance, the orientational disorder and translational order of dumbbells in case of plastic crystals and ordered crystal may enable a photonic band gap to be turned on & off by application of an external electric field. As computationally found by Li et al. [22] an ordered phase of dumbbells is potentially helpful for the realization of a full photonic

band gap. Here we showed that the crystallization of anisotropic particles and manipulating of them by an external field can be achieved by dispersing these particles in organic solvents with a dielectric constant of $4 < \epsilon < 10$. We think that soft interactions for anisotropic particles' self-assembly gives important additional possibilities to manipulate the system. Plastic solid phase observed here is either a plastic crystal or a plastic glass. Although there is not a strong evidence for the crystallinity of our system it is possible that the Debye screening length of the system can be increased such that crystallinity becomes significant. Here we have also shown an interesting transition between solid states by using an external electric field, which switches the plastic solid into an orientational and translational ordered crystal.

Acknowledgements

The author thanks Carlos van Kats (Utrecht University, Soft Condensed Matter) and Patrick Johnson (Amolf) for helpful discussions and for introducing the synthesis of the silica dumbbells and IDL routines. Marjolein Dijkstra, Hanumantha Rao Vutukuri and Johan Stiefelhagen (Utrecht University, Soft Condensed Matter) are thanked for useful discussions.

References

- [1] Manoharan, V. N.; Elsesser, M. T.; Pine, D. J. *Science*, **2003**, *301*, 483.
- [2] van Blaaderen, A.; *Science*, **2003**, *301*, 470.
- [3] Maldovan, M.; Thomas, E. L.; *Nature Mater.*, **2004**, *3*, 593.
- [4] Yake, A. M.; Panella, R. A.; Snyder, C. E.; Velegol, D.; *Langmuir*, **2006**, *22*, 9135.
- [5] Sheu, H. R.; El-Aasser, M. S.; Vanderhoff, J. W. *J. Polym. Sci.*, **1990**, *A28*, 629.
- [6] Johnson, P. M.; van Kats, C. M.; van Blaaderen, A. *Langmuir*, **2005**, *21*, 11510.
- [7] Zhang, R.; Schweizer, K. S. *Phys. Rev. E*, **2009**, *80*, 011502.
- [8] Chong, S. H.; Götze, W. *Phys. Rev. E*, **2009**, *65*, 041503.
- [9] Vega, C.; Monson, P.A.; *J. Chem. Phys.*, **1997**, *107*, 7.
- [10] Marechal, M.; Dijkstra, M. *Phys. Rev. E*, **2008**, *77*, 061405.
- [11] Wojciechowski, K. W.; Frenkel, D; et al. *Phys. Rev. Lett.*, **1991** *24*, 3168.
- [12] Lee, S. H.; Gerbode, S. J.; John, B. S.; Wolfgang, A. K.; Escobedo, F. A.; Cohen, I; Liddell, C. M. *J. Mater. Chem.*, **2008**, *18*, 4912.
- [13] Hosein, I.D.; John, B. S.; Lee, S.H.; Escobedo, F. A.; Liddell, C. M. *J. Mater. Chem.*, **2009**, *19*, 344.
- [14] Yethiraj, A.; van Blaaderen, A. *Nature*, **2003**, *421*, 513.
- [15] Yethiraj, A.; Thijssen, J.; Wouterse, A.; van Blaaderen, A. *Adv. Mater.*, **2004**, *16*, 596.
- [16] Vermolen, E. C. M.; Kuijk, A.; Filion, L. C.; Hermes, M.; Thijssen, J. H. J.; Dijkstra, M.; van Blaaderen, A. *Proc. Nat. Ac. of Sci.*, **2009**, *xxx*, xxx.
- [17] Mittal, M.; Furst, E. M. *Adv. Funct. Mater.* , **2009**, *19*, 3271.
- [18] Leunissen, M. E.; van Blaaderen, A.; Hollingsworth, A. D.; Sullivan, M. T.; Chaikin, P. M. *Proc. Nat. Ac. of Sci.*, **2007**, *105*, 2585.
- [19] Ge, J.; Hu, Y.; Yin, Y. D. *Angew. Chem. Int. Ed.* **2007**, *46*, 7428.
- [20] Ge, J.; Yin, Y. D. *Adv. Mater.* **2008**, *20*, 3485.
- [21] Hosein, I. D.; Ghebrehghan, M.; Joannopoulos, J. D.; Liddell, C. M. *Langmuir*, **2009**, online.
- [22] Li, Z. Y.; Wang, J.; Gu, B. Y. *J. Phys. Soc. of Jpn*, **1998**, *9*, 3288.
- [23] Stöber, W.; Fink A.; Bohn, E. *J. Colloid Interface Sci.* **1968**, *26*, 62.
- [24] van Blaaderen, A.; Vrij, A. *Langmuir*, **1992**, *8*, 2921.
- [25] Bosma, G.; Pathmamanoharan, C.; de Hoog, E. H. A.; Kegel, W. K.; van Blaaderen, A.; Lekkerkerker, H. N. W. *J. Colloid Interface Sci.*, **2002**, *245*, 292.
- [26] van Blaaderen, A.; Ruel, R.; Wiltzius, P. *Nature* **1997**, *385*, 321.
- [27] Crocker, J. C.; Grier, D. G. *J. Colloid Interface Sci.*, **1996**, *179*, 298.
- [28] Particle tracking routines were downloaded from web page of Weeks E. R. Particle tracking using IDL. <http://www.physics.emory.edu/~weeks/idl/>
- [29] Pohl, H. A. *J. Appl. Phys.*, **1951**, *22*, 869.
- [30] Pohl, H. A. *Dielectrophoresis* Cambridge University Press, London, 1978.
- [31] van der Zande, B. M. I.; Koper, G. J. M.; Lekkerkerker, H. N. W. *J. Phys. Chem. B*, **1999**, *103*, 5754.
- [32] Hynninen, A. P.; Dijkstra, M. *Phys. Rev. Lett.*, **2005**, *94*, 138303.
- [33] Wu, Y. L.; Derks, D.; van Blaaderen, A.; Imhof, A. *Proc. Nat. Ac. of Sci.*, **2009**, *106*, 10564.

7

Phase Behavior of Colloidal Dumbbells in an Electric Field

We studied in real space by confocal microscopy the phase behavior of non-density matched, micron sized and charged colloidal dumbbells, pairs of (possibly overlapping) spheres, in an electric field. From computer simulations the phase behavior is already known for hard dumbbells, but not for dipolar and/or soft dumbbell type particles. The formation of 3D dumbbell crystals was only possible with the assistance of an external electric field, which orients the particles and when no field was applied dumbbell particles only yielded colloidal glasses. We investigated dumbbell particles with two different size ratios (length/width) and with a double layer thin and thick compared to the particle size at two different electric field strengths. Already this sparsely probed parameter space yielded 6 different crystal structures of which 4 were not yet observed before. Moreover, one martensitic crystal-crystal transition was found as a function of the electric field strength. The analysis of the systems with a long-ranged repulsive interaction also made it clear that the crystal properties of these crystals can be tuned by the application of an external electric field as it allows reorientation of the dumbbells without destroying the crystallinity.

7.1 Introduction

The self assembly of colloids into colloidal crystals received a lot of attention in the recent literature [1] not only because it is an interesting condensed matter model system in the study of crystallization, but also for its use in realizing advanced materials such as photonic crystals [2]. In principle, self assembly is an inherently cheap method to produce 3D structures, however, for single sized spheres these are more or less limited to body centered cubic (bcc) for long range repulsive systems or face centered cubic (fcc) for harder potentials. Moreover, external fields are necessary to guide the self assembly, e.g. to orient crystals in preferred orientations. External fields can also help to obtain some new crystal structures such as hexagonally close packed (hcp) with colloidal epitaxy [3] and body centered cubic (bcc) with electric fields [4, 5], but the number of symmetries and structures is limited. One way to significantly increase the number of structures available is to turn to binary colloidal crystals. For instance, in the case of the recently discovered binary crystals made from particles with an opposite charge the number of different crystal structures has been more than doubled [7, 8]. Moreover, even for binary hard sphere crystals new phases have recently been discovered, such as binary Laves phases which could lead to a diamond photonic crystal but which have for now only been realized in computer simulations [9]. Another approach to arrive at a richer set of crystal structures is to make the interaction potentials in between the particles more complex [10–12]. For instance, by creating so-called patchy particles [11] or by using anisotropic rod-like shaped colloids [13]. Perhaps the simplest anisotropic particles (certainly if one wants to make them from spherical building blocks) are two spheres held together: dumbbells. The self assembly of colloidal dumbbells is not only of scientific importance fundamentally as they are the colloidal analogue of diatomic molecules but may also be useful for photonic band gap materials applications [14]. For instance, Li et al. [15] have shown with photonic band gap calculations that dumbbell crystals ordered in specific crystal lattices can exhibit a full photonic band gap. Recently, the first experimental papers on dumbbell self organization were presented, but it mainly was focussed on 2D systems [16, 17]. In computer simulations more work on 3D systems has been done, for instance Vega et al. and Marechal and Dijkstra studied the phase behavior of hard colloidal dumbbells [18, 19]. In the phase diagram of hard dumbbells Marechal and Dijkstra observed plastic crystals for an aspect ratios below 0.4. The aspect ratio is defined as the length-to-diameter ratio $L^*=L/\sigma$, where L is the distance between the centers of the two overlapping spheres and σ is the diameter of each sphere (For clarity, here in our definition of a dumbbell the two spheres forming it can overlap). For aspect ratios over 0.4 and at higher volume fractions there is an ordered crystal phase and for aspect ratios over 0.9 there is an aperiodic crystal phase. This aperiodic crystal phase was first predicted by Frenkel for a 2D system much earlier [20]. In the 2D phase that Frenkel found dimers have random orientations and it thus is a rare exam-

ple of a disordered equilibrium solid phase. Marechal and Dijkstra predict the 3D equivalent of this crystal phase, which they call an 'aperiodic crystal' also in part of the 3D phase diagram as mentioned above [19]. In Fig. 6.1 (of Chapter 6) the phase diagram of Marechal and Dijkstra is given where the aspect ratio is plotted against volume fraction (ϕ) and against number density (ρ^*). In this chapter we present experimental results on self-assembly and crystallization of colloidal silica dumbbells synthesized according to procedure of Johnson et al. [26]. They are dispersed in index matching solvent DMSO-water and also in organic solvents. Here we investigate the crystal structures of the dumbbells, compare their structure with literature predictions and discuss their possible photonic applications. As mentioned in Chapter 6 charged particles dispersed in a solvent of dielectric constant $4 < \epsilon < 10$ exhibit soft interactions for sufficiently low ionic strengths. For the soft system we investigated particles with a core aspect ratio of 0.9 and for the hard dumbbell system we used two different aspect ratios of 0.9 and 0.7. An important finding was that without an electric field we only obtained glassy systems, this is why electric fields were used in all crystallization experiments. An external electric field prevented the formation of the aperiodic crystal structure, which is at close packing photonically not different from an *fcc* crystal of single spheres. In addition to this an external electric field is a very efficient tool to control the rotational degree of freedom of the anisotropic particles, especially in the case where softness in the potential literally leaves more room for this [22, 23]. We are fully aware of the fact that the parameter space that is spanned up by the double layer thickness (softness), size ratio of the particle cores and electric dipole induced dipolar field strength is large. Moreover, as far as we know, the phase diagram of soft-hard-dipolar dumbbells is not yet known, contrary to that of soft-hard-dipolar spheres [7, 8]. In this chapter we only probed the parameter space with a few points, but the results obtained with these points give an indication of the increased possibilities for new structures.

Long range repulsions due to large screening lengths that can be achieved in cyclohexyl bromide (CHB) effectively increased the value of σ such that $L^* = L/\sigma$ values around 0.44 can be reached. This opened the way to explore a plastic solid phase as described in the previous chapter. In addition to this, a soft interaction makes crystallization easier for particles probably for kinetic reasons, moreover as mentioned they can also be more easily manipulated with an external field. The lower kinetic barriers in soft systems make them superior systems for studying self assembly.

Moreover, as colloidal dumbbells are analogues of diatomic molecules their phase study is of also fundamental importance. The crystal structures found for colloidal dumbbells of aspect ratio 0.7 and 0.44 are similar structures to α -O₂ (aspect ratio 0.42) and α -F₂ (aspect ratio 0.50). They all have a base-centered-monoclinic crystal structure with C2/m symmetry [24]. For diatomic molecules multipolar interactions, of which quadrupolar interaction is the most significant, play a significant role in stabilizing some crystal structures, like α -N₂ (aspect ratio 0.3) [25], Cl₂, Br₂ and I₂ with Cmca symmetry and aspect ratios of 0.63, 0.72 and 0.84, re-

spectively [24] (see Table 7.1). It is also striking that simple theory excluding the quadrupolar interactions, but retaining the Lennard-Jones interaction, predicts the base-centered monoclinic crystal structure with $C2/m$ symmetry to be the stable structure for aspect ratios from 0.32 to 0.84 for all of the diatomic molecules [24]. They also find $P6m2$ structure closely stable with very slight difference in free energy (0.02% difference in energy). Considering the dipolar forces between the dumbbell colloids due to the presence of the electric field, which aligns all dumbbells in the field direction, our findings are in agreement with the literature structures of diatomic molecules.

7.2 Experimental details

Particles

Synthesis of Particles: 1.3 μm and 800 nm silica spheres were synthesized via seeded growth of Stöber [27] silica particles synthesized according to van Blaaderen et al. [28] with a rhodamine isothiocyanate (RITC) labeled core. The fabrication of the dumbbells was done according to the procedure of Johnson et al. [26] developed in our lab. For the 0.9 aspect ratio dumbbells, 1.3 μm silica particles were first dimerised and then coated with a thin silica layer to covalently stick the spheres. For 0.7 aspect ratio dumbbells, 800 nm silica particles after being dimerised were coated with extra silica to a diameter of 1.3 μm per sphere of the dumbbell. For dispersing the silica dumbbells in conventional solvents like dimethylsulfoxide (DMSO) no extra treatment was made. However, to disperse them in CHB the particles were surface modified. Prior to purification with density gradient centrifugation (DGC) [26] technique the silica dumbbells were coated with a layer of 3-(trimethoxysilyl)propyl methacrylate (TPM) under Stöber conditions. After this TPM coating the silica particles were still water dispersible and purified with DGC. No more than 1% of spheres were left in the dumbbell suspension after DGC. The purified dumbbells were dispersed in CHB with the help of poly(12-hydroxy stearic acid) (PHSA) stabilizer, which is used in the synthesis of PMMA particles according to the procedure of Bosma et al. [29]. 5-15mg of PHSA-PMMA graft-comb stabilizer was dissolved in 10 g of CHB and this solution was used to disperse dried silica dumbbells. The electric field applied was an AC electric field with a frequency of 1MHz, high enough that the double layer ions cannot follow the field. Particle dispersions were put in a capillary with 0.4 mm square cross section, which was sputter coated with chromium (3 nm) and gold (9 nm) on two opposite sides for applying an external electric field, as shown in Fig. 7.1.

Refractive index matching dimethylsulfoxide DMSO:water solutions were prepared as described in ref. [30] where 11.6% water was mixed with 88.4% DMSO by weight.

The symmetry of the crystal structures obtained for dumbbells were investigated by using a computer programme specifically designed to classify crystal

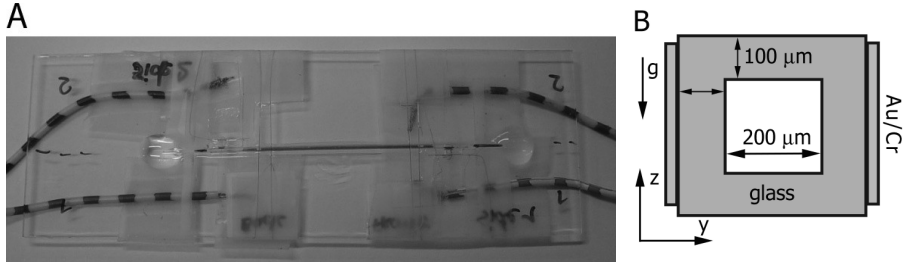


Figure 7.1: Sample cell with two parallel plate electrodes (a) Photograph of the ~ 5 cm long & 0.4 mm wide sample cell, on top of a supporting microscopy slide. (b) Schematic cross section of the sample cell in (a). Electric field is along y-axis and gravity is shown with "g".

structures based on particle coordinates, which is available online [33].

7.3 Results and discussion

It was found for all systems studied here that apart from a few layers close to the glass bottom wall the sediments obtained without an electric field were amorphous and glassy solids as illustrated in Fig. 7.2. These glasses are of interest in their own [34]. However, in this chapter the main focus is on the crystal structures of dumbbells. In case of the hard dumbbell system crystals were obtained by sedimentation in the presence of an electric field. It should also be mentioned that the crystals we obtained had an average height of 7-11 layers of particles after sedimentation and the initial volume fractions of the dispersions were 7-9%. It is important to remark here that all structures in this chapter formed not only under the influence of an electric field, but also under the influence of a gravitational field. The gravitational length of our dumbbells was 230 nm for 0.9 aspect ratio dumbbells in DMSO:water. Gravitational length is known from experiments for spheres (285 nm) [36] and from simulations for dumbbells (0.25-1) [32].

As mentioned, the phase diagram for soft-hard and dipolar dumbbells is not known, but it is instructive however, using estimates of the double layer thickness and the dipolar field strength between two spheres, to place the parameters used for the dumbbells in the phase diagram of that of soft dipolar spheres under the same parameters. This gives for instance an indication of how dominant the dipolar interactions are. For estimating the dimensionless prefactor γ , which measures the strength of the dipole induced on the particles, we used the following formula (more details can be found in ref. [6] together with the phase diagrams of dipolar hard and soft spheres.):

$$\gamma = \frac{\pi\sigma^3\beta^2\epsilon_m\epsilon_0|E_{loc}|^2}{8k_B T} \quad (7.1)$$

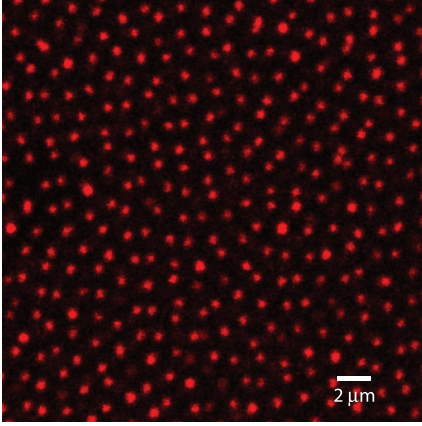


Figure 7.2: Confocal microscopy image of RITC labeled silica dumbbell glass formed by sedimentation without an electric field. The aspect ratio of these particles is 0.7. Image size is $23.25\mu\text{m} \times 23.25\mu\text{m}$

where E_{loc} is the local electric field and defined as $E_{loc} = \mathbf{E} + \mathbf{E}_{dip}$. Here, \mathbf{E} is the external field and \mathbf{E}_{dip} is the field induced by the other dipoles and the polarizability of the particles in the medium is determined by β as $\beta = (\epsilon_p - \epsilon_m) / (\epsilon_p + 2\epsilon_m)$, where ϵ_p is the dielectric constant of the particles and ϵ_m is the dielectric constant of the medium. Here, E_{loc} was also estimated by $E_{loc} = E / (1 - \alpha\pi/6)$ [31]. The double layer thickness for the hard dumbbell cases is about several tens of nanometers. Here, we find the volume of the dumbbell and take the half of it as the volume of the sphere and assume this truncated sphere as a sphere for calculations. The volume of the dumbbell is given with the following formula [32], where r is the radius of a sphere of the dumbbell.

$$V_{db} = \frac{4\pi r^3}{3} \left(1 + \frac{3}{2}L^* - \frac{1}{2}(L^*)^3 \right) \quad (7.2)$$

Crystals of Hard Dumbbells with an aspect ratio 0.9

Crystals of colloidal hard dumbbells with an aspect ratio of 0.9 were produced by sedimentation of the particles in the presence of an electric field. The particles aligned along the electric field direction and self-assembled into crystals upon sedimentation, which took about 20-30 minutes. The crystal structure was annealed by flipping the sample cell up & down 3-4 times and repeating the sedimentation while keeping the field on, in a similar procedure as was previously found for spheres [30]. For the particular case shown in Fig. 7.3 we estimated γ as 383 for a sphere of dumbbell, which indicates strong dipolar interactions.

Confocal microscopy images of the resulting crystals of the RITC labeled silica dumbbells in an electric field of $177 V_{rms}/\text{mm}$ are shown in Fig. 7.3. An image from the 3D crystal stack in the xy -plane is given in Fig. 7.3a.

Although all particles are dumbbells, only the cores of the spheres making up the dumbbells are visible in the microscopy image. The high aspect ratio of the

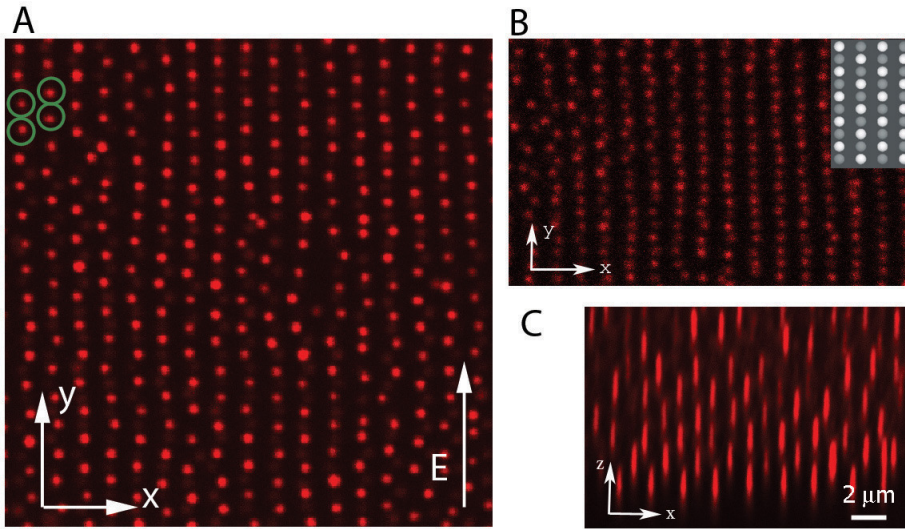


Figure 7.3: Confocal microscopy images of RITC labeled silica dumbbells in a crystal formed in an electric field of $177 \text{ V}_{\text{rms}}/\text{mm}$ with an aspect ratio of 0.9. (a) An image in the xy plane of the 3D stack, where dumbbells are oriented along the field and form a hexagonal pattern ((110) plane), only fluorescent sphere centers of the dumbbells are visible. (b) An image of the same stack in the xy -plane clearly shows the bridge-site stacking of the crystal structure. Here 4 layers of the stack were superimposed and the inset shows two hexagonal planes of dumbbells that were overlaid, where white and gray spheres corresponds to dumbbell spheres of different hexagonal layers. (c) An image of the xz -plane where aba stacking is observed ((001) plane). Image size (a) = $23.78 \mu\text{m} \times 23.78 \mu\text{m}$, (b) = $21.6 \mu\text{m} \times 13.2 \mu\text{m}$, (c) = $25.5 \mu\text{m} \times 8.5 \mu\text{m}$. Color version of the image is on page 123.

particles complicates the visualization of the dumbbell particles. These dumbbell particles structurally are very close to two touching spheres, which makes them look like single spheres in confocal microscopy images, although in movies of the particles the dumbbells can be recognized as the coupled centers move in unison. When the spheres making up the dumbbells are considered as separate spheres, stacking of the spheres is identical to the bct lattice of single spheres. Note that single spheres in an electric field also exhibit a bct structure [30, 35]. However, when the centers of mass of the dumbbells are considered the crystal structure is a tetragonal structure with space group number 129 and a symmetry of $P4/nmm$; the Wyckoff position of this structure is c with $z = -0.125$ [37]. The parameters for the unit cell are; $a = 1.5 \mu\text{m}$, $b = 1.5 \mu\text{m}$ and $c = 2.5 \mu\text{m}$. In this structure the dipolar interactions are significant and determines the final structure. An image of the dumbbells that is an overlay (superposition) of particles in xy -planes of 4 layers is shown in Fig. 7.3b, this image is actually similar to what one would observe for the bct structure of single spheres and shows the bridge-site stacking of the next layer on the previous one. Fig. 7.3c shows an image of the same stack of particles in the xz -plane, where the dumbbells are now perpendicular to the

image plane. This clearly illustrates the **aba** stacking of the crystal phase and agrees with the designated space group. Note that a single sphere making up the dumbbell appears stretched in the z -direction due to the larger width of the microscope's point spread function in this direction.

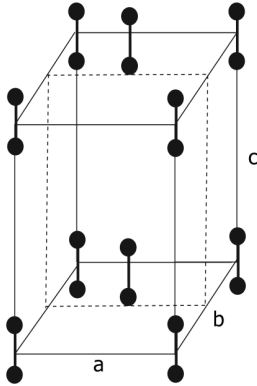


Figure 7.4: Tetragonal unit cell of hard dumbbell particle crystal with an aspect ratio of 0.9 formed in an electric field of $177 V_{rms}/mm$. The crystal has a $P4/nmm$ symmetry with the space group number 129. Here $a, b = 1.5 \mu m$ and $c = 2.5 \mu m$.

In Fig. 7.4 the unit cell of a crystal of the hard dumbbells with 0.9 aspect ratio is given, where the dumbbells are aligned along the field direction and the dumbbells at the base-centers are shifted by a quarter of a unit cell parameter in the field direction. Note that one sphere of the center dumbbell touches the upper and lower unit cell planes. As the field was increased to $\sim 250 V_{rms}/mm$ the crystal structure was destroyed. Inhomogeneity of the field at higher fields caused formation of stripes at the edges close to electrodes, while pushing the rest of the particles closer to the middle of the capillary.

Crystals of Hard Dumbbells with an aspect ratio 0.7

Crystals of colloidal hard dumbbells with an aspect ratio of 0.7 (with a gravitational length of 400 nm) were grown similar to the previous case by sedimentation of the particles in an electric field. The particles got aligned in an electric field and self-assembled into crystals upon sedimentation. Confocal microscopy images of the resulting crystals of RITC labeled silica dumbbells in an electric field of $147 V_{rms}/mm$ are shown in Fig. 7.5 where we estimated the prefactor γ as 243 for half of a dumbbell. As is seen in Fig. 7.5a the dumbbell particles can be easily distinguished and tracked as a result of the lower aspect ratio that keeps the labeled cores closer to each other. The images of the 3D crystal stack in the xy -plane, xz -plane and in the yz -plane are shown in Fig. 7.5a, b and c, respectively. In the xy -plane the hexagonal order of all aligned-dumbbell particles is noticeable. In 3D these particles form a stack, similar to the fcc lattice of hard spheres in that the next layers are identical to the first, but shifted along the dumbbell length in y -direction. However, here centers of the dumbbells form a

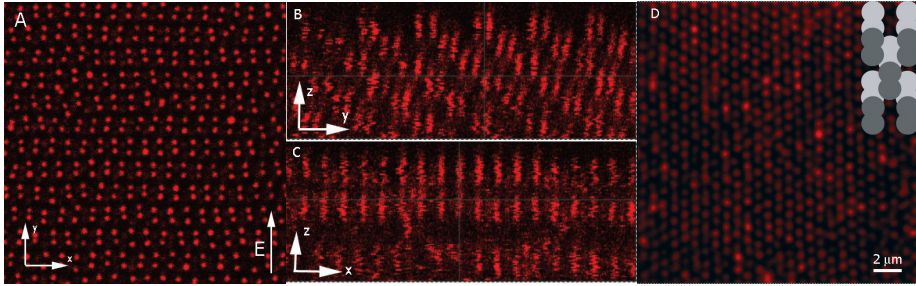


Figure 7.5: Confocal microscopy images of RITC labeled silica dumbbells with an aspect ratio of 0.7 in a 3D crystal formed with an electric field of $147 \text{ V}_{\text{rms}}/\text{mm}$. (a) An image of an xy plane out of the z -stack, where the dumbbells are oriented along the field and form a hexagonal pattern. (b) An image reconstructed from the same stack in the zy plane where the **abcdea** stacking is visible. (c) A reconstructed image out of the same 3D stack in the xz plane where only the **ada** layers are visible, (d) an image made by projecting 8 layers in the xy plane, which is evidence for close-packing and the regularity of the crystal. The inset is the stacking of the hexagonal layers, where white and gray dumbbells show different layers. Image size (a) = $27.09 \mu\text{m} \times 27.09 \mu\text{m}$. Color version of the image is on page 124.

abcdea stacking sequence instead of an **abca** stacking of *fcc*. In this stacking the coordinate of the dumbbell repeats itself at the 6th layer whereas this happens in the 4th layer for an *fcc* crystal (see Fig. 7.5b). The image of the xz -plane shown in Fig. 7.5c shows only 3 layers with a rectangular symmetry. These layers are **ada** layers of the stack, which means that particles from the 1st, 4th and 6th layer are visible. As can be seen from Fig. 7.5b in the 4th layer the other (complementary) sphere of the dumbbell particle comes to the same y -position as the 1st layer and this is the reason for the 4th layer (**ada** layers) to be observed in the xz plane image given in Fig. 7.5c. The image shown in Fig. 7.5d is a superposition of 8 layers in the xy -plane. The superposition of layers for this kind of **abcdea** stacking results surprisingly in a very neat image, which fills all the possible holes and forms regular hexagons composed of the fluorescent cores of the spheres. It should be noted that the superposition of an *fcc* crystal of singles would just yield the same superposition. We think that this is a result of close packing, however here close packing is restricted by the aspect ratio and shape of the dumbbells.

From our analysis of the particle coordinates we found the crystal structure to be base-centered monoclinic with the space group $C2/m$ (number 12) and a Wyckoff position a . The unit cell parameters for the structure are as follows; $a=4.4 \mu\text{m}$, $b=1.7 \mu\text{m}$ and $c=1.5 \mu\text{m}$. Crystals with base-centered monoclinic phase and $C2/m$ symmetry were also predicted for dumbbell particles by Vega et al. [25], which they named CP1 and CP2 for close-packed *fcc-like* and *hcp-like* stacking of the dumbbell centers of mass. Note that the structure of $\alpha\text{-O}_2$ has the same base-centered monoclinic structure with a unit cell angle $\beta = 132^\circ$ [38] whereas in our dumbbell structure $\beta = 153^\circ$. Also the orientation of the dumbbells in $\alpha\text{-O}_2$ differs: dumbbell axes orient perpendicular to the ab -plane in the unit cell of α -

O_2 . However, in our system dumbbell axes are parallel to the ab -plane. We think that the different aspect ratios brought about the difference in the angle β . Here the electric field does not directly influence β , but it fixes the orientation of the dumbbell and it is possible that changing the orientation of the electric field with respect to gravity may change β or the stacking. The unit cell of the crystal structure and the angle β are depicted in Fig. 7.6. From this unit cell it can be seen that the orientation of the external electric field and the aspect ratio of the dumbbells influence the angle β . The aspect ratio of Br_2 is 0.72 and is closest to the above structure, however the observed structure for Br_2 is an orthorhombic crystal with a $Cmca$ symmetry [24] (see also Table 7.1). It was suggested theoretically that quadrupolar interactions, which do not exist for our colloidal dumbbells, stabilized the orthorhombic phase of Br_2 with respect to the monoclinic phase. In addition to this the dipoles on the dumbbells do not only align the particles but may also affect the stable structure of the crystal formed.

Table 7.1: Stable phases and aspect ratios of di-atomic molecules [24].

	α - N_2	α - O_2	F_2	Cl_2	Br_2	I_2
Stable phases	$Pa3^a$	$C2/m$	$C2/m^b$	$Cmca^c$	$Cmca$	$Cmca$
Aspect ratio	0.32	0.42	0.5	0.63	0.72	0.84

^a cubic ^b monoclinic ^c orthorhombic

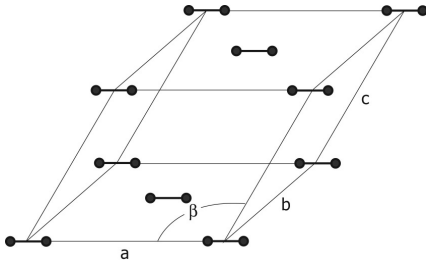


Figure 7.6: Base-centered monoclinic unit cell of colloidal dumbbell crystals with the $C2/m$ symmetry and the space group number 12.

After the electric field strength was increased to $234 V_{rms}/mm$ (γ estimated as 615) for the already crystalline particles the structure of the system evolved to a bct phase in few seconds, but we allowed the system evolve for 10 minutes before making images. The confocal images given in Fig. 7.7 show the bct phase clearly. The xy -plane as seen in Fig. 7.7a has hexagonally ordered dumbbells similar to the previous case, however, the stacking is different here. Again, the layers are identical but shifted half a period perpendicular to the dumbbell length. The xy -plane given in Fig. 7.7b is characterized by **aba** stacking where the 3rd layer is at the same position as the 1st, resulting in 4-fold symmetry. This stacking is a property of bct and combined with the Fig. 7.7c, which has hexagons of singles

Table 7.2: Crystal structures of dumbbells with different aspect ratios, interactions and electric field strength.

Sample*	Space group	H-M symbol	Wyckhoff position- β	parameters	Fig.
0.9 - hard - high	129 ^a	P4/nmm	c, z = -0.125	a = 1.5 μm , b = 1.5 μm , c = 2.45 μm	7.3
0.7 - hard - low	12 ^b	C2/m	a, $\beta = 153^\circ$	a = 4.4 μm , b = 1.7 μm , c = 1.5 μm	7.5
0.7 - hard - high	139 ^c	I4/mmm	e, z = -0.05	a = 1.1 μm , b = 4.1 μm , c = 1.1 μm	7.7
0.4 - soft - low ^d	12 ^b	C2/m	a, $\beta = 152^\circ$	a = 3.0 μm , b = 7.1 μm , c = 3.2 μm	7.8
0.4 - soft - low ^e	12 ^b	C2/m	a, $\beta = 136^\circ$	a = 3.0 μm , b = 3.0 μm , c = 4.0 μm	7.9
0.4 - soft - high	139 ^c	I4/mmm	e, z = -0.05	a = 2.1 μm , b = 2.1 μm , c = 6.9 μm	8.4

* The sample is described by aspect ratio, interaction and field strength, respectively.

^a = tetragonal, ^b = monoclinic, ^c = body-centered-tetragonal

^d stands for the **abca** stacking for sample Fig. 7.8.

^e stands for the **aba** stacking for sample Fig. 7.9

indicates a *bct* phase. To have an idea about the long range stacking we superimposed 6 layers in *xy*-plane on top of each other. This resulted in the image given in Fig. 7.7d, where the dumbbells are sitting on the bridge-site in the *x*-axis and form a rectangular structure, which belongs to *bct*. The space group of this crystal phase is I4/mmm with space group number 139. Because the movements in the unit cell are small and did not require a restacking of layers this is a martensitic crystal-crystal transition [36]. Space groups, space group numbers, Hermann-Mauguin (H-M) symbols, Wyckhoff positions and parameters of this crystal structure are tabulated in Table 7.2 along with all other structures.

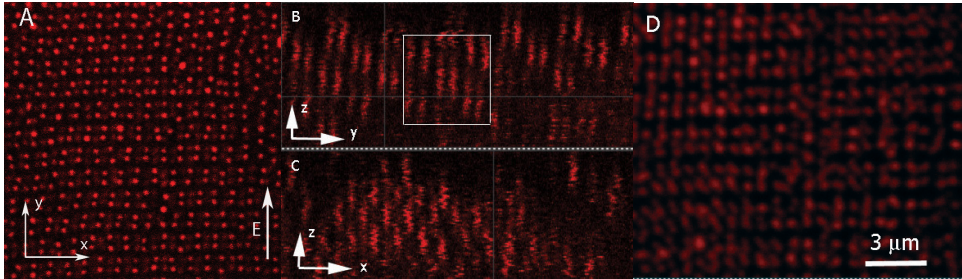


Figure 7.7: Confocal microscopy images of RITC labeled silica dumbbells with an aspect ratio of 0.7 in a crystal formed with an electric field of 234 V_{rms}/mm . (a) An image in the *xy*-plane of the 3D stack, where hexagonally ordered dumbbells oriented along the field are observed. (b) An image of the same stack in the *yz*-plane where the **aba** stacking is visible. (c) An image of in the *xz*-plane where **aba** layers are visible. (d) The 6 layers of the *z*-stack are superimposed on each other, implies that all the layers were on top of each other. Image size (a) = 25.05 μm * 25.05 μm . Color version of the image is on page 124.

Crystals of Soft Dumbbells with an effective aspect ratio ~ 0.4

Here, crystals of colloidal soft dumbbells were made by sedimentation of the particles (with an aspect ratio of 0.9 and a gravitational length of 320 nm) in an organic solvent (CHB) as described in Chapter 6. Besides the plastic solid phase that formed when no field was applied and described in Chapter 6, particles also form more fully ordered crystals when an electric field is applied. It was easier to obtain crystals with the soft system and no flipping of the sample was found to be necessary for annealing the crystal structure as the repulsion between the particles gave apparently enough freedom for the particles to rearrange during the sedimentation process. The Coulomb repulsion between the particles, which causes the soft interaction, keeps the particles well separated and enables them to be rotated by an external electric field easily. The crystalline structure can be turned on & off easily by switching the electric field. The confocal microscopy images of the crystal structure obtained, when an electric field of $106 \text{ V}_{\text{rms}}/\text{mm}$ was applied, are given in Fig. 7.8. As is seen from the image of the xy -plane in Fig. 7.8a particles were aligned by the field. The value of γ was 12 for a half of the dumbbell, which means that the dipole-dipole interactions were relatively mild. The effective aspect ratio of the dumbbells in this structure was 0.44. Nematic order parameter (S_{3d}) for these soft dumbbell particle systems were found to be as 0.864 ± 0.006 when an external electric field of $106 \text{ V}_{\text{rms}}/\text{mm}$ was applied and it was 0.00 ± 0.02 for the case without an electric field (see also Chapter 6). The structure observed for the soft dumbbells in a moderate electric field is again a base-centered monoclinic structure with space group number 12 and with a C2/m symmetry. This structure has the same symmetry as the 0.7 aspect ratio hard dumbbells in moderate electric fields, however, here the unit cell angle β was 152° instead of 153° , as was the case for the hard dumbbell crystal. The stacking shown in Fig. 7.8b belongs to a phase with C2/m symmetry. Here an **abca** stacking, where 4th layer of particles has the same position as the 1st, is observed. The rectangle in the image outlines the **abca** stacking of the crystal. The superposition of layers in xz -plane of the stack is shown in Fig. 7.8c which agrees with the proposed space group. The unit cell parameters of this system are: $a=7.1\mu\text{m}$, $b=3.0\mu\text{m}$ and $c=3.2\mu\text{m}$ with $\beta=152^\circ$. Aspect ratio of F_2 is 0.50 and is closest to the above structure and F_2 is observed to have the same symmetry C2/m with an angle $\beta=134.6^\circ$. F_2 was also suggested to be a simple van der Waals' solid with low quadrupolar interactions [24]. In case of diatomic molecules there is a tilt of molecular axis with respect to the unit cell axes, this tilt angle does not exist in our crystals due to the electric field and this may cause changes in β .

Most of the crystal domains of these colloidal soft dumbbells at lower electric field strengths ($106 \text{ V}_{\text{rms}}/\text{mm}$) were observed to have a base-centered monoclinic phase with C2/m symmetry, but in the sample cell we also observed regions which had a structure with an **aba** stacking. The images of this crystal structure that was also observed with an electric field of $106 \text{ V}_{\text{rms}}/\text{mm}$ (where we estimated the prefactor γ as 12 for a half of the dumbbell) are given in Fig. 7.9. As

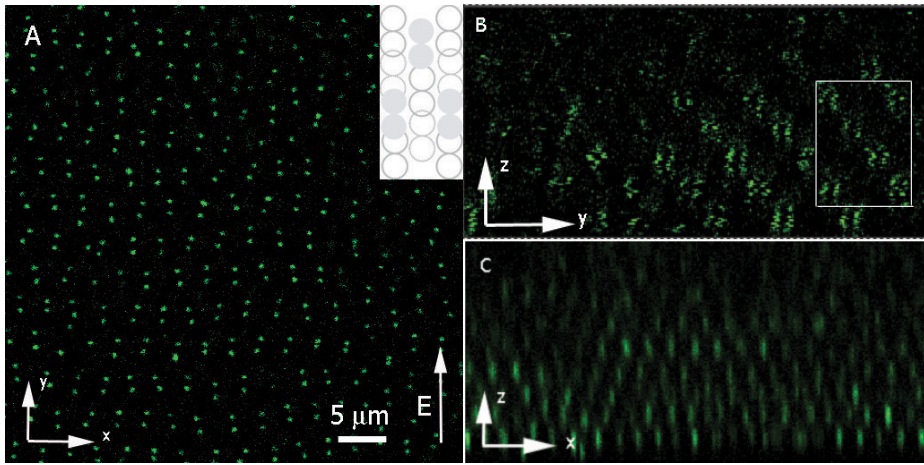


Figure 7.8: Confocal microscopy images of soft dumbbells, which formed a base-centered monoclinic crystal with $C2/m$ symmetry when an electric field of $106 V_{rms}/mm$ (prefactor γ was 12 for a half of the dumbbell) was applied. (a) An image in the xy -plane scanned in sequence to build up a 3D stack. (b) An image in yz -plane reconstructed from the 3D stack, the rectangular region outlines $abca$ stacking of the crystal. (c) An image in xz -plane superimposed over 3 layers in this plane that shows the hexagonal order of the fluorescent cores of the dumbbells aligned along the field, which agrees with the proposed $C2/m$ symmetry of phase. Image size (a) = $46.80\mu m \times 46.80\mu m$. Color version of the image is on page 124.

is seen from an image of xy -plane in Fig. 7.9a particles were aligned head-to-toe parallel to the electric field, contrary to all the other structures. The structure observed for the soft dumbbells under these circumstances was base-centered monoclinic with the symmetry group $C2/m$ but with unit cell angle $\beta = 136^\circ$. The stacking shown in Fig. 7.9b shows an aa stacking with a square symmetry. Here the 3rd layer of particles has the same position as the 1st layer. A projection of 5 layers in the xy -plane is shown in Fig. 7.9c. This image agrees with the unit cell shown in Fig. 7.10. Note that in Fig. 7.9c two crystal domains are observed on the right and left hand side of the image with a line defect in the center. The unit cell parameters of this system are similar to the previous soft system with; $a = 3.0\mu m, b = 3.0\mu m, c = 4.0\mu m$ and $\beta = 136^\circ$. Note that here in Fig. 7.9a particles form parallelograms, which looks like a different stacking with respect to the previous case under similar conditions. However, as seen in the unit cell of this structure shown in Fig. 7.10, the unit cell is again the base-centered monoclinic $C2/m$. However, here the orientations of the dumbbells were different: they were not lying in the hexagonal plane but passing through it. This suggests that here the structure was grown on the parallelogram face instead of the hexagonal one with the same symmetry. Note that, the effective aspect ratio of the system is similar to that of F_2 with a similar $\beta = 136^\circ$ (for F_2 $\beta = 134.6^\circ$), with the same

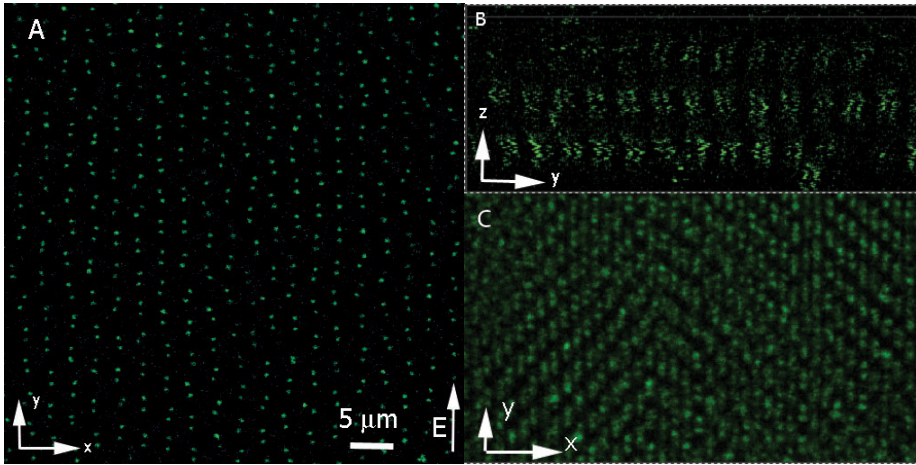


Figure 7.9: Confocal microscopy images of soft dumbbells, which form a base-centered monoclinic crystal phase with $C2/m$ symmetry when an electric field of $106 V_{\text{rms}}/\text{mm}$ ($\gamma \approx 12$) was applied. (a) Image of an xy -plane scanned in sequence to build up a 3D stack, (b) an image in yz -plane reconstructed from the 3D stack, the square region outlines the aa stacking of the crystal, where b is not visible from this view, (c) an overlay of 5 xy layers, this image shows the stacking of the phase clearly. Image size (a) = $55.28\mu\text{m} \times 55.28\mu\text{m}$. Color version of the image is on page 125.

base-centered monoclinic structure and similar to $\alpha\text{-O}_2$ as well with aspect ratio 0.42 and $\beta = 132^\circ$. This time the orientation of the dumbbells is identical to that of the molecules in $\alpha\text{-O}_2$ and F_2 . The observed monoclinic angle β is also nearly the same.

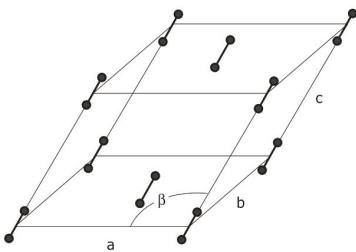


Figure 7.10: Monoclinic unit cell of colloidal dumbbell crystals, which is base-centered monoclinic with the $C2/m$ symmetry and the space group number 12. Here, it is observed that dumbbells are oriented differently when compared with the previous case. This is the corresponding unit cell for the structure shown in Fig. 7.9

After the electric field strength was increased from $106 V_{\text{rms}}/\text{mm}$ to $200 V_{\text{rms}}/\text{mm}$ (raising the prefactor γ to 45 for half of the dumbbell) the crystal structure of the system evolved to a bct phase with space group number 139 and with a $I4/mmm$ symmetry. It should be noted that the effective aspect ratio of the dumbbells in this crystal structure due to the high field strength increased to 0.6, whereas it was 0.44 for the soft systems with moderate electric fields

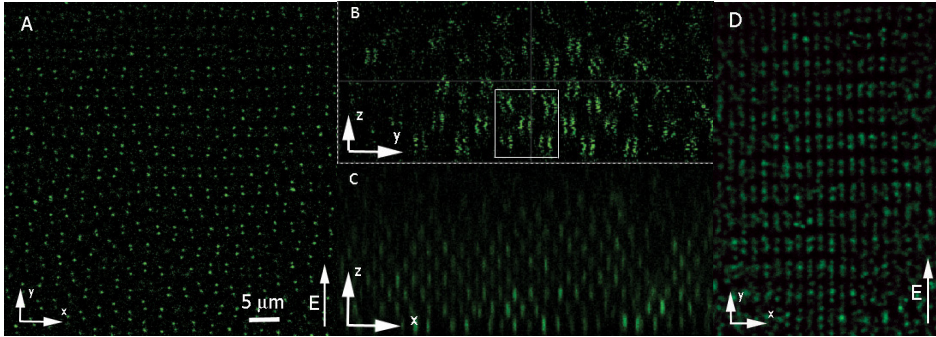


Figure 7.11: Confocal microscopy images of soft dumbbells, which form a *bct* crystal when an electric field of $200 \text{ V}_{\text{rms}}/\text{mm}$ ($\gamma \approx 45$) was applied. (a) Image of an *xy*-plane scanned in sequence to build up a 3D stack, (b) Image of an *yz*-plane reconstructed from the 3D stack, the square region outlines the *aba* stacking of the crystal. (c) An image of an *xz*-plane of the stack showing the hexagonal order of the dumbbells aligned along the field, which agrees with the proposed *bct* phase, (d) a projection of 6 layers in the *xy*-plane, this image shows the bridge-site stacking of a *bct* phase clearly. Image size (a) = $59.12\mu\text{m} \times 59.12\mu\text{m}$. Color version of the image is on page 125.

($106 \text{ V}_{\text{rms}}/\text{mm}$). The confocal images given in Fig. 8.4 show different planes of the new structure. The *xy*-plane as seen in Fig.8.4a has the hexagonally ordered dumbbells similarly to the previous case, however, the stacking is different in this case. Because the movements in the unit cell are small and did not require a restacking of layers this is a martensitic crystal-crystal transition. This is similar to the *fcc-bct* transition that was observed for hard dipolar spheres [36]. The *xy*-plane given in Fig.8.4b shows an *aba* stacking where the 3rd layer is at the same position as the 1st. This stacking is a property of the *bct* lattice, and combined with the Fig. 8.4c, showing hexagons of singles proves the *bct* phase. To have an idea about how the layers were stacked in the *z* direction we superimposed 6 layers in the *xy*-plane on top of each other. This resulted in the image in Fig. 8.4d where the dumbbells are sitting on the bridge-site in the *x*-axis and form a rectangular structure of *bct*. The unit cell parameters for the *bct* phase of these soft dumbbells are: $a=2.1\mu\text{m}$, $b=2.1\mu\text{m}$ and $c=6.9\mu\text{m}$.

7.4 Conclusions & outlook

We have made a first start at exploring experimentally the crystallization of colloidal dumbbell particles in the presence of an electric field with respect to the aspect ratio and the softness of the inter-particle interactions as set by the Debye-Hückel screening length. The phase behavior becomes much richer with the inclusion of the long-ranged charge or soft interactions between the particles by using a solvent with a dielectric between $4 < \epsilon < 10$. This also lowers to aspect ratio to 0.44. The soft interactions were found to facilitate crystallization and furthermore

enabled the manipulation of the crystal properties with an electric field by allowing literally more room for the external field to align the dumbbells in different directions or switch between different crystal structures through a martensitic transition. The silica particles used in this work would not crystallize in the absence of an electric field. This is probably due to their rapid sedimentation and short gravitational length, which quickly leads to kinetic arrest resulting in amorphous or glassy solids. However, with the electric field the particles crystallized quite readily with their long axis parallel to the field. Note that, in this work the structures observed were the equilibrium phase structures combined with gravity as the particles were not density matched but only refractive index matched.

We analyzed the crystallization of dumbbells with a hard core size ratio of 0.7 and 0.9 for two values of the double layer thickness, one small compared to the particle size and the other on the same order of the particle size. Moreover, the crystals were grown at two electric field strengths. Already at this quite sparse probing of the enormous parameter space we observed 6 different crystal structures of which to the best of our knowledge 4 have not been seen before. We also observed a martensitic crystal-crystal transition as a function of the electric field strength. For the crystals obtained with the long-ranged soft repulsions it was furthermore clear that the electric field could be used to reorient the dumbbells while maintaining crystallinity and thus change the crystal properties. Such switching behavior is interesting for photonic use of such crystals. Although it is clear from these few results that the possibilities for new crystal structures with these anisotropic particles are significantly increased it is also clear that a more extensive study of the phase behavior, possible martensitic switching, and the glass formations in these systems is warranted. When dumbbell particles are dispersed in CHB two different kind of structures with the monoclinic $C2/m$ symmetry were observed at low field strengths and a bct phase is observed at high field strengths. Crystals of base-centered-monoclinic $C2/m$ symmetry were also predicted for hard dumbbell particles by Vega et al. [25]. Notably, some of the diatomic molecules also form crystals with $C2/m$ symmetry. α - O_2 and F_2 crystals are known to form base-centered monoclinic phases with $C2/m$ symmetry. Although it is known that for α - O_2 the magnetic dipole moment has a role to stabilize the α phase [39], F_2 is a simple van der Waals solid without any significant dipolar or quadrupolar interactions [24], and the base-centered monoclinic phase is only caused by the geometry of the molecule and van der Waals attractions.

Acknowledgements

The author thanks Carlos van Kats, Patrick Johnson, Hanumantha Rao Vutukuri and Johan Stiefelhagen for helpful discussions.

References

- [1] Palberg, T. *J. Phys.-Cond. Mat.*, **1999**, *11*, 28, R323.
- [2] Imhof, A.; Three-dimensional photonic crystals made from colloids, *Nanoscale Materials*, edited by L. M. Liz-Marzan and P. V. Kamat (Kluwer Academic, Boston, 2003), pp. 423-454.
- [3] Hoogenboom, J. P.; van Langen-Suurling, A. K.; Romijn, J.; van Blaaderen, A. *Phys. Rev. Lett.*, **2003**, *90*, 138301.
- [4] Dassanayake, U.; Fraden, S.; van Blaaderen, A. *J. Chem. Phys.*, **2000**, *112*, 3851.
- [5] Hynninen, A. P.; Dijkstra, M. *Phys. Rev. Lett.*, **2005**, *94*, 138303.
- [6] Hynninen, A. P.; Dijkstra, M. *Phys. Rev. E.*, **2005**, *72*, 051402.
- [7] Hynninen, A. P.; Christova, C. G.; van Roij, R.; van Blaaderen, A.; Dijkstra, M. *Phys. Rev. Lett.*, **2006**, *96*, 138308.
- [8] Hynninen, A. P.; Leunissen, M. E.; van Blaaderen, A.; Dijkstra, M. *Phys. Rev. Lett.*, **2006**, *96*, 018303.
- [9] Hynninen, A. P.; Thijssen, J. H. J.; Vermolen, E. C. M.; Dijkstra, M.; van Blaaderen, A. *Nature Mater.*, **2007**, *6*, 202.
- [10] van Blaaderen, A. *Nature*, **2006**, *439*, 545.
- [11] Glotzer, S. C.; Solomon, M. J. *Nature Mat.*, **2007**, *6*, 557.
- [12] Yang, S. M.; Kim, S. H.; Lima, J. M.; and Gi-Ra, Y. *J. Mater. Chem.*, **2008**, *18*, 2177.
- [13] Vroege, G. J.; Lekkerkerker, H. N. W. *Rep. Prog. Phys.*, **1992**, *55*, 1241.
- [14] Hosein, I. D.; Ghebrebrhan, M.; Joannopoulos, J. D.; Liddell, C. M. *Langmuir*, **2009**, online.
- [15] Li, Z. Y.; Wang, J.; Gu, B. Y. *J. Phys. Soc. of Jpn*, **1998**, *67*, 9, 3288.
- [16] Lee, S. H.; Gerbode, S. J.; John, B. S.; Wolfgang, A. K.; Escobedo, F. A.; Cohen, I.; Liddell, C. M. *J. Mater. Chem.*, **2008**, *18*, 4912.
- [17] Hosein, I. D.; John, B. S.; Lee, S. H.; Escobedo, F. A.; Liddell, C. M. *J. Mater. Chem.*, **2009**, *19*, 344.
- [18] Vega, C.; Monson, P. A.; *J. Chem. Phys.*, **1997**, *107*, 7.
- [19] Marechal, M.; Dijkstra, M. *Phys. Rev. E*, **2008**, *77*, 061405.
- [20] Wojciechowski, K. W.; Frenkel, D.; Branka, A. C. *Phys. Rev. Lett.*, **1991** *24*, 3168.
- [21] Mock, E. B.; Zukoski, C. F. *Langmuir*, **2007**, *23*, 8760.
- [22] Mittal, M.; Furst, E. M. *Adv. Funct. Mater.*, **2009**, *19*, 3271.
- [23] Feng, Z.; Zhang, X.; Feng, S.; Ren, K.; Li, Z. Y.; Cheng, B.; Zhang, D. *J. Opt. A: Pure Appl. Opt.*, **2007**, *9*, 101.
- [24] English, C. A.; Venables, J. A. *Proc. R. Soc. Lond. A*, **1974**, *340*, 57.
- [25] Vega, C.; Paras, E. P. A.; Monson, P. A. *J. Chem. Phys.*, **1992**, *96*, (12), 9060.
- [26] Johnson, P. M.; van Kats, C. M.; van Blaaderen, A. *Langmuir*, **2005**, *21*, 11510.
- [27] Stöber, W.; Fink A.; Bohn, E. *J. Colloid Interface Sci.* **1968**, *26*, 62.
- [28] van Blaaderen, A.; Vrij, A. *Langmuir*, **1992**, *8*, 2921.
- [29] Bosma, G.; Pathmamanoharan, C.; de Hoog, E. H. A.; Kegel, W. K.; van Blaaderen, A.; Lekkerkerker, H. N. W. *J. Colloid Interface Sci.*, **2002**, *245*, 292.
- [30] Yethiraj, A.; Thijssen, J. H. J.; Wouterse, A.; van Blaaderen, A. *Adv. Mater.*, **2004**, *16*, 596.
- [31] Tao, R.; Sun, J. M. *Phys. Rev. Lett.*, **1991**, *67*, 398.
- [32] Matthieu Marechal, PhD Thesis, Chapter 4, **2009**.
- [33] Online version of the FYNDSYM programme by Harold T. Stokes and Dorian M. Hatch, which is available at <http://stokes.byu.edu/findsym.html>.
- [34] Zhang, R.; Schweizer, K. S. *Phys. Rev. E*, **2009**, *80*, 011502.
- [35] Yethiraj, A.; van Blaaderen, A. *Nature*, **2003**, *421*, 513.
- [36] Yethiraj, A.; Wouterse, A.; Groh, B.; van Blaaderen, A. *Phys. Rev. Lett.*, **2004**, *92*, 058301.
- [37] International Tables for Crystallography, Volume A Space Group Symmetry, edited by Hahn, Theo. (Fifth edition), 2005

[38] Meier, R. J.; Helmholtz, R. B. *Phys. Rev. B*, **1984**, *29*, 1387.

[39] English, C. A.; Venables, J. A.; Salahub, D. R. *Proc. R. Soc. Lond. A* , **1974**, *340*, 81.

8

Chains of Colloidal Beads

An external electric field induces dipolar interaction between colloidal particles. Inter-dipolar interactions favors head-to-toe arrangement of the colloids and this causes the particles to form string fluids for low-volume-fraction dispersions and relatively low dipolar interaction energies. In this chapter we show our preliminary results on making permanent chains out of colloidal spherical particles. With this methodology it was possible to make colloidal chains from emulsion droplets, silica particles and polystyrene particles. By coating the dipolar strings with extra material, either the same or different from the core allowed us to make the strings permanent. This procedure offers a way of synthesizing anisotropic particles with the length tunable by the electrode spacing. Such permanent strings of colloidal particles are potentially interesting as a model system for studying liquid crystalline phase transitions. In addition to that flexible strings are useful as model system for (bio)polymer systems.

8.1 Introduction

Macroscopic properties of a colloidal suspension can change dramatically by applying an external electric field. An electric field can increase the viscosity of the suspension by several orders of magnitude and can turn the original fluid into a solid-like material. As the field is switched off the material returns back to the original state. Colloidal suspensions that exhibit this property are called electro-rheological fluids [1, 2]. In an electro-rheological fluid, the colloidal particles are suspended in a solvent with a significantly different dielectric constant. The particles acquire a dipole moment in an external electric field due to this permittivity contrast.

The change observed in the flow behavior of such electro-rheological suspension is due to the induced dipole-dipole interactions between the particles that lead to a change in the microstructure. Electro-rheological fluids, due to the possibility of easy manipulation of the macroscopic properties by switching the field, have found a variety of industrial applications, such as hydraulic valves, clutches, brakes and displays [3, 4]. There have been many experimental, e.g. Ref. [5–8] focus on work of our own group which pioneered quantitative real space analysis of these systems, theoretical, e.g. [9–13], and simulation studies, e.g. [14–16], investigating the nature of the field-induced particle structures of these fluids.

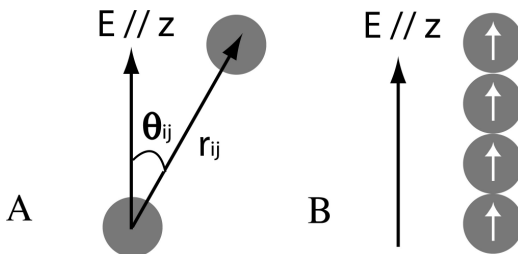


Figure 8.1: Dipole-dipole interactions induced by an electric field. (a) For each pair of particles the vector r , which connects their centers, forms an angle θ with the direction of the external electric field, oriented along the z axis. (b) The dipoles (depicted as arrows) favor particle configurations in which they are aligned in a head-to-toe fashion.

The phase diagram of dipolar hard and soft spheres as a function of dipolar strength was studied experimentally by Yethiraj et al. [5]. For low volume fractions the structure was found to be a string-like fluid phase, which is basically a combination of chains of particles in the field direction and a liquid like order in the plane perpendicular to it, see Fig. 8.1. The same behavior was also shown in computer simulations by Hynninen et al. [17] that confirmed the stability of the observed crystal structures and predicted also some structures other than Yethiraj et al. [5] observed.

In this chapter, we will mainly focus on suspensions with low particle concentrations. Here, we assume that the particles interact via a pair-potential that can be written as the sum of a DLVO type screened Coulomb interaction [18, 19], a hard-core repulsion, and point-like dipole-dipole interactions [20]. We will neglect the van der Waals interactions, because our systems are either well index matched and/or the repulsions are of sufficient range that the particles will never

come into contact. The first two contributions are isotropically repulsive and for two particles, separated by the vector r_{ij} , it can be written as follows:

$$\frac{U_{\text{Yukawa}}(r_{ij})}{k_B T} = \begin{cases} \epsilon_c \frac{\exp[-\kappa(r_{ij}-\sigma)]}{r_{ij}/\sigma}, & r_{ij} \geq \sigma \\ \infty, & r_{ij} < \sigma \end{cases} \quad (8.1)$$

where k_B is Boltzmann's constant, T the absolute temperature, κ the inverse Debye screening length ($\kappa^{-1} = 1/\sqrt{8\pi\lambda_B c}$ for a number density $2c$ of a monovalent salt is given below) and σ the hard-core, or particle diameter. The value of this potential at contact (when $r_{ij} = \sigma$) is

$$\epsilon_c = \frac{Z^2}{(1 + \kappa\sigma/2)^2} \frac{\lambda_B}{\sigma} \quad (8.2)$$

where Z is the particle charge and $\lambda_B = e^2/4\pi\epsilon_0\epsilon_m k_B T$ is the Bjerrum length of the suspending medium with dielectric constant ϵ_m ; e is the elementary charge and ϵ_0 is the permittivity of vacuum. The (point) dipole-dipole contribution to the total interaction can be written as:

$$\frac{U_{\text{dip}}(r_{ij})}{k_B T} = \frac{\gamma}{2} \left(\frac{\sigma}{r_{ij}}\right)^3 (1 - 3\cos^2\theta_{ij}) \quad (8.3)$$

where, θ_{ij} is the angle that r_{ij} forms with the z axis, which is the direction of the electric field (Fig. 8.1a). The dimensionless prefactor is given by:

$$\gamma = \frac{\mathbf{p}^2}{2\pi\epsilon_0\epsilon_m\sigma^3 k_B T} \quad (8.4)$$

and $\mathbf{p} = \frac{\pi}{2}\beta\epsilon_0\epsilon_m\sigma^3\mathbf{E}_{\text{loc}}$ is the dipole moment induced in the particle by the local electric field $\mathbf{E}_{\text{loc}} = \mathbf{E} + \mathbf{E}_{\text{dip}}$. Here, \mathbf{E} is the external field and \mathbf{E}_{dip} is the field induced by the other dipoles. Finally, the polarizability of the particles in the medium is determined by β :

$$\beta = \frac{\epsilon_p - \epsilon_m}{\epsilon_p + 2\epsilon_m} \quad (8.5)$$

where ϵ_p is the dielectric constant of the particles. From these equations, it can be seen that the phase behavior basically depends on four parameters: the density of the suspension, the charge of the colloids, the screening length of the solvent and the strength of the applied field. From Eq. 8.3 it is also clear that the dipole-dipole interaction is anisotropic. It gives rise to an attraction when $\theta_{ij} < 54.7$, but

repulsive interactions otherwise. It can be concluded that when the colloids are not highly charged and when the screening length is not high the dipole-dipole interaction easily overcomes the repulsions and forms strings of colloids for low particle concentrations. It is important, though, that there are significant charge-charge interactions at far enough distance, otherwise the strings start to interact laterally and become sheets and bct crystals [21].

Inspired by similar behavior, Bibette and co-workers have observed string formation by applying an external magnetic field to magnetic beads and they conducted notable work to understand the bridging of polymers used for stabilizing the magnetic particles in an external magnetic field. Although the strings they formed to understand the bridging were not permanent they have shown strings which last for few days long [22]. A similar idea by Velev and co-workers was used to fabricate micro-wires by the assembly of metal nanospheres [23], where conductive spheres were aligned by applying an external electric field to form wires for bio- and micro-circuits. In addition to this recent work Farle and co-workers reported 1D assembly of magnetic cobalt spheres, which were made permanent with a silica shell around the particles [24]. This kind of strings of particles that form a 1D assembly are important for micro-electronics as wires in case of conductive spheres and important photonically for offering the possibility of changing the aspect ratio of the particles [25]. In addition to the above mentioned functions the controlled production of such segmented rods is useful to study the liquid crystal phase transitions and basics of polymer dynamics experimentally which is well established computationally and theoretically.

Fabrication of flexible strings may also offer the chance of studying and mimicking bio-polymers like DNA, actin and microtubules, which are all quite stiff compared to 'regular' polymers.

8.2 Experimental details

Particle preparation

1.3 μm silica particles were synthesized with seeded growth of Stöber [26] silica particles synthesized according to van Blaaderen et al. [27] with a rhodamine-B-isothiocyanate (RITC) labeled core. An electric field was applied to the silica particles under Stöber conditions, which means the presence of ethanol, ammonia and silica precursor: tetraethyl orthosilicate (TEOS). Particle growth in the presence of an electric field caused the particles to stick to each other covalently because of the growth of a thin silica shell around touching particles. String formation for silica particles was observed in ethanol and in glycerol. Glycerol with 10-20% (v/v) of ammonia was the optimum condition for long and stiff silica strings, which gave the necessary silica coating in 2-3 h. For a 0.5-1 % volume percent particle dispersion in 10 mL glycerol, an amount of 100 μL TEOS was added for the coating of silica strings. We put the mixture in a capillary, apply

an electric field of 200 V/mm and let the reaction for 2-3 hours. Glycerol due to its higher density and viscosity is superior to ethanol because of slower Brownian motion, which keeps the chain of particles more straight.

Monodisperse emulsion droplets were synthesized according to the procedure of Zoldesi et al. [28]. We found that by playing with the ammonia concentration it was possible to get large monodisperse droplets as large as $\sim 4 \mu\text{m}$. The idea we applied was to increase the ammonia concentration as we increased the concentration of precursor dimethyl dimethoxysilane (DMDS). Typically Zoldesi et al. used 2-10 % (v/v) ammonia with 2-10 % (v/v) DMDS concentrations but we used 20-25 % (v/v) ammonia with 5-10 % (v/v) DMDS with the methodology of keeping ammonia always higher than DMDS concentration. Larger droplets were manipulated easier with an electric field (see Equation 8.3 where σ^3 is a volume term) and the resulting shells and strings of larger droplets are more elastic compared to the ones templated from smaller droplets [29, 30]. For confocal microscopy measurements of emulsion droplets the fluorescent RITC dye was coupled to 3-aminopropyl triethoxy silane (APS) prior addition to the droplet dispersion. The coupling reaction was done in a little amount of ethanol (0.5 mL) solution by mixing 0.1 mL APS with ~ 0.001 g of RITC and sonicating at least for 1 h. It is important to keep the amount of ethanol low because ethanol dissolves the oil droplets. RITC is normally soluble in water and stays in water first, however the APS-RITC reaction product likes oil droplets more, compared to water and labels the droplets after a diffusion period. For the synthesis of strings the dispersion of droplets with the silica precursor was let for a period for the shell growth before applying the electric field, which caused less overlap between the shells in the string and yielded in better flexibility. However droplets could also be stringed up without the shell formation but in any case for the string formation the silica shell is necessary to stick the droplets to each other. The amount of TEOS for the shell growth was 0.018M as described in Ref. [28].

Polystyrene (PS) particles were synthesized according to the procedure of Goodwin et al. [31] and were dispersed in ethanol for further experimentation. The PS particles were grown larger with titania in the presence of an electric field according to the conditions described in Chapter 5. For all sample preparations volume fractions of the samples were kept below 0.5 % to avoid particle aggregation as they sediment. For 10 mL ethanol dispersion of particles 0.1 mL tetra-butyl titanate (TBT) was used to coat PS particles together.

Experiments were made in rectangular capillaries 0.1 mm*1 mm size, equipped with conductive wires for applying an electric field of 1 MHz frequency, in order to only polarize the particle cores and not the double layers.

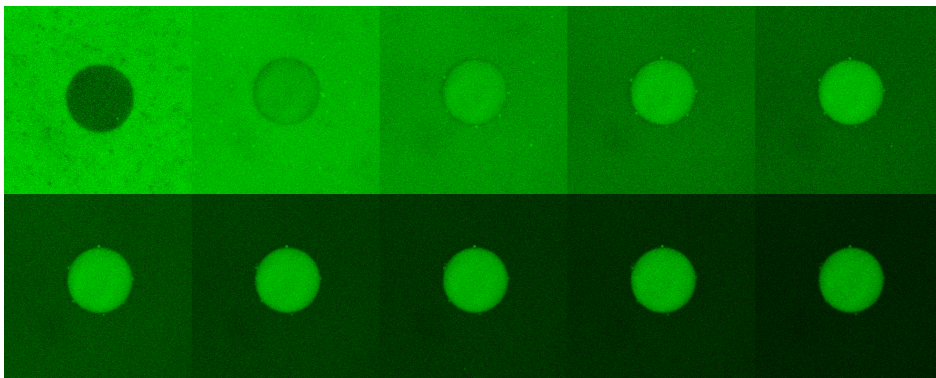


Figure 8.2: A series of confocal microscopy images of a large emulsion droplet in time which shows the diffusion of the APS-RITC couple into the droplet over 2 hours of time. In the first panel all the dye is in the dispersing medium and the droplet is dye-free, whereas in the last panel all the dye has gone into the droplet and the medium is almost free of dye. The images in the panels were taken at times $t: 0$ min, 11 min, 23 min, 35 min, 46 min, 57 min, 69 min, 80 min, 92 min and 102 min. Image size of single a panel is $167.8\mu\text{m} \times 167.8\mu\text{m}$.

8.3 Results and discussion

8.3.1 Chains of Emulsion Droplets

Emulsion droplets

For the synthesis of labeled emulsion droplets, first the emulsion droplets with the method of Zoldesi et al. [28] were synthesized and then the dye RITC coupled to APS was added to the dispersion medium of the emulsion droplets. As APS-RITC is soluble in water it first stayed in the water phase but diffused subsequently into the oil phase in time in which it is apparently better soluble. It was already known that RITC is hydrophilic (with an ionic structure) and dissolves in water and does not diffuse into the oil phase of PDMS droplets. However previous work done by Vincent and co-workers [32] had shown that silane precursors like APS and methyl-triethoxy silane (MTES) when mixed with the PDMS droplets, diffuse into the oil phase and cause the droplets to swell. However, only MTES forms a network (cross-link) with the oligomers of PDMS. It was also shown by Vincent and co-workers [32] by using NMR that MTES couples to the network of the DMDS molecules, but that APS is only physically driven to the oil phase because of better dissolution and does not couple to the structure due to the steric hinderance of the functional group on the precursor whereas this functional group is significantly smaller in MTES. For the droplets with APS there were no triply functional siloxanes detected, which meant APS stayed in the droplet as a monomer or it coupled only to the ends of the linear oligomer that amounts

only ~15 % of the droplet [32]. For the same reason the APS-RITC molecule does not couple to the droplet network, but only diffuses into the oil phase and labels the droplets. A series of confocal microscopy images of a large emulsion droplet, which shows nicely the diffusion of the dye, is given in Fig. 8.2. It is seen from the confocal microscopy images shown in Fig. 8.2 that at the beginning of the series the continuous phase (water) contains all of the dye, whereas the emulsion droplet is free of dye. The images in the panels of Fig. 8.2 were taken over a period of 102 min.

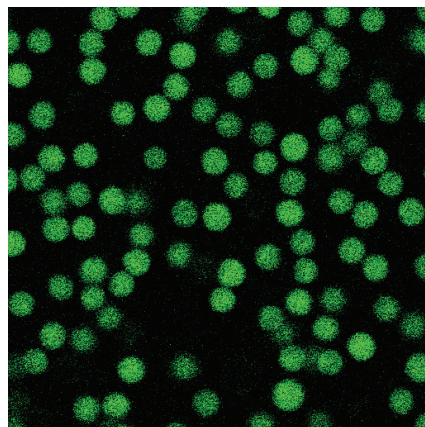


Figure 8.3: (a) Confocal microscopy image of RITC labeled emulsion droplets . Image size = $59.33\mu\text{m}\times 59.33\mu\text{m}$.

In time it is observed that the contrast between the water and oil phase first decreases and after a while becomes the reverse of the start of the experiment. Apparently, the coupling of RITC to APS makes it more favorable for the RITC molecules to diffuse into the emulsion droplet than to stay in the water phase. The confocal images were taken over 102 minutes, which is approximately the time the APS-RITC molecules took to completely diffuse to the emulsion droplets. It is likely that the poly-dimethylsilane (PDMS) nature of the emulsion droplets and APS has a similar structure and motivates the RITC diffusion into the droplets. After approximately 2 hours of diffusion time the particles became all labeled as shown in Fig. 8.3.

To see a difference in size we have performed SLS on the emulsion droplets before and after the addition of the APS-RITC. The SLS graph is given in Fig. 8.4 and shows the size growth of the droplets as the dye is added, which was also observed by the Vincent group [32]. Fig. 8.4 shows that the emulsion droplets with a diameter of 1740 nm with 5% polydispersity swelled into 2 μm size with the addition of APS-RITC. SLS curves of the droplets (symbols) were fitted to theoretical calculations of the full Mie solutions to the form factor (line) with the refractive index of the droplets 1.37 and 1.36 before and after addition of the dye, respectively. One other evidence that APS-RITC does not couple to the emulsion droplets was observed when TEOS was added to the medium, TEOS started

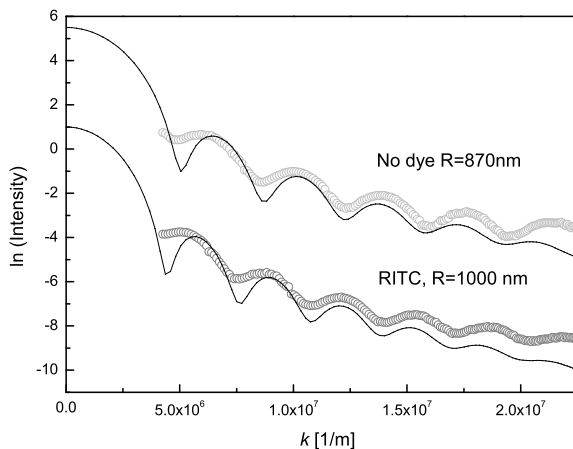


Figure 8.4: SLS experimental curves of the emulsion droplets (symbols) in water fitted to theoretical calculations of the full Mie solutions to the form factor (lines) for droplets before and after addition of the APS-RITC dye. The refractive index of the emulsion droplets was estimated to be 1.37 and 1.36 before and after dye incorporation.

to form a solid silica shell on the oil droplet together with the APS, as new APS molecules diffused towards the silica shell. We observed that as the silica shell formed, APS integrated into the silica shell and diffused back from the oil phase to the shell to incorporate with silica shell, resulting in fluorescent labeled shells.

Chain formation of emulsion droplets

According to the procedure of Zoldesi et al. [28], as TEOS is added into the dispersion of the emulsion droplets a silica shell grows on the droplets. We applied the same procedure in the presence of an electric field for producing permanent strings of emulsion droplets. The electric field arranges the emulsion droplets into strings and as the silica shell grows on the droplets the strings become permanent. In Fig. 8.5 reflection mode confocal microscopy images of the droplet strings are shown. In the panels of the figure different conformations of the same string in time can be observed from the images taken over 1 min. These different conformations in time clearly demonstrate the flexibility of the string. As found by Zoldesi et al. [30] silica shells formed around the PDMS droplets, which were elastic, could buckle inwards depending on the size and thickness of the shell. We think that with the strings formed by the method proposed here, it is possible to

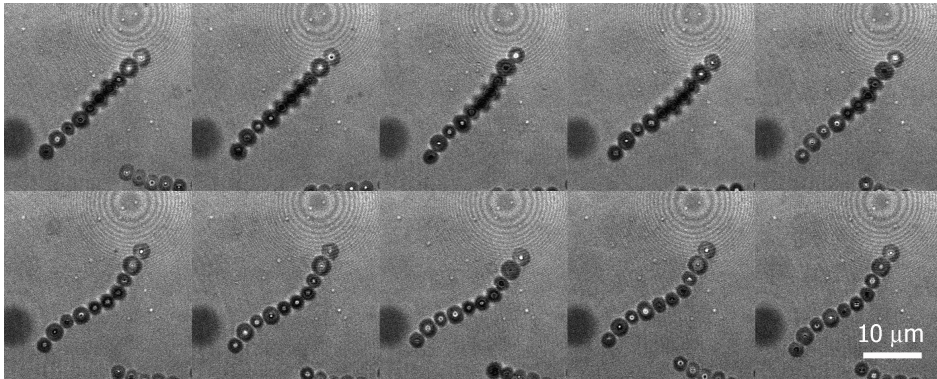


Figure 8.5: Reflection mode confocal microscopy images of flexible emulsion droplet strings the conformational differences in the images show the flexibility of the chain. Image size of a panel is $=32.89 \mu\text{m} \times 32.89 \mu\text{m}$. Images were taken at times t : 0 sec, 6.5 sec, 13 sec, 19.5 sec, 26 sec, 32.5 sec, 39 sec, 45.5 sec, 52 sec, 58.5 sec and 64 sec.

play also with these parameters to produce flexible or non-flexible strings of silica shells. Here we give an example of flexible strings as shown in the panels of Fig. 8.5 and work is in progress to analyze the results to obtain an estimate of the elastic modulus for the strings.

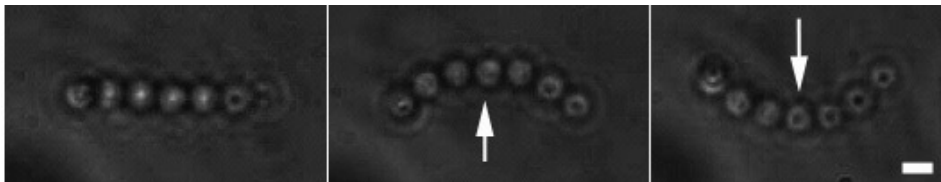


Figure 8.6: Bright field microscopy images of a flexible emulsion droplet string, which was trapped with 3 traps by using optical tweezers and the middle trap was moved up and down to bend the string. The panels show the 3 conformations of the string when traps were on a line (first panel), when the middle trap was moved up (second panel) and when the middle trap was moved down (third panel). Scale bar= $2 \mu\text{m}$.

To explicitly show the flexibility we used optical tweezers to hold the string with 3 traps on a line. Fig. 8.6 demonstrates three different conformations of the string. First, three traps were on a line and the string was linear. As the middle trap was moved upwards the string started to bend as shown in the second panel. It was also shown that by moving the middle trap in the opposite direction of the previous case the string could be bent downwards. Together with Fig. 8.5 this result proves the flexibility of these strings.

The emulsion droplets as mentioned before could be labeled with a fluorescent

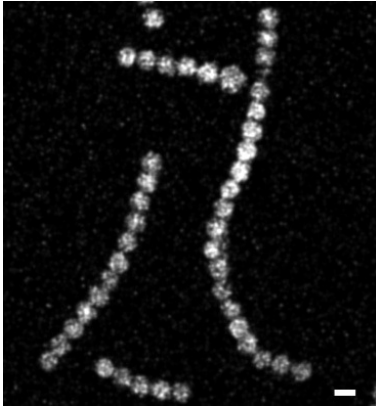


Figure 8.7: Confocal microscopy image of RITC labeled fluorescent emulsion droplet strings. Scale bar 5 μm .

dye by simply coupling this dye to APS and adding this to the dispersion of emulsion droplets. By using labeled droplets, labeled strings can easily be formed as shown in Fig. 8.7. The study and analysis of strings for estimating elastic modulus is easier and more accurate for the labeled strings with fluorescence images in comparison to the reflection images.

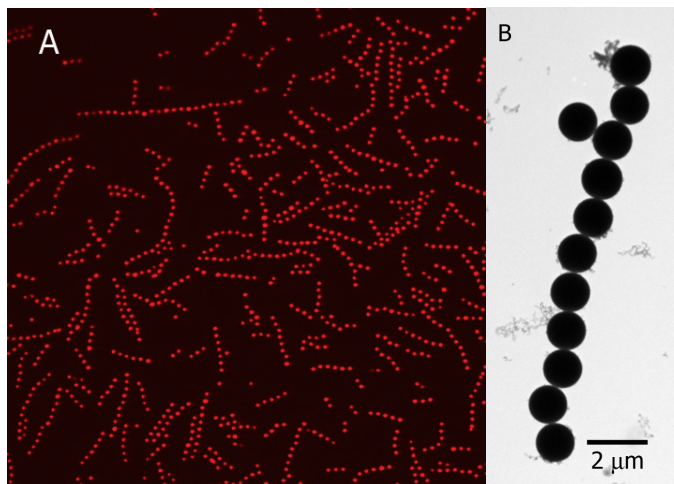


Figure 8.8: Chains of silica particles labeled with RITC with a size of 1.3 μm . (a) confocal microscopy fluorescence image of several chains, (b) TEM image of a chain of silica particles. Image size (a) 90.87 μm * 90.87 μm .

8.3.2 *Chains of Silica Particles*

It is well known [5–8] that silica particles dispersed in ethanol (or glycerol) will form strings if an external electric field on the order of $0.1 \text{ V}/\mu\text{m}$ and 1 MHz frequency is applied. Here we have demonstrated that if the field is applied in a Stöber solution with the silica precursor, particles can grow together to form strings. For this purpose we put a very dilute particles dispersion in ethanol (or glycerol) with ammonia and TEOS. When the field was applied for 2–10 hours depending on the ammonia concentration the silica growth on the particles was found to be enough to hold the particles together, which yields the silica chains shown in Fig. 8.8a. The silica growth on the particles should at least be 30 nm to keep the particles together. It should be kept in mind that while the string was formed by the electric field the Brownian motion drives fluctuations in the string shape so the field should be high enough to keep the particles in close contact against the double layer repulsion and high enough to arrive at strings that are more or less straight. Note that the glycerol medium for the string formation of silica particles gave better results because of the slower Brownian motion. With this technique it was also possible to take out these silica chains from the capillary into a dispersion and make TEM images of the strings, as shown in Fig. 8.8b where the silica growth is no more than few tens of nanometers.

In the strings that we synthesized the length distribution of the particles is broad. As an electric field is applied particles span the length between the two electrodes and as the field is turned off the particles randomly break down from the weakest point on the chain and this causes the polydispersity of the strings. In future work this can be easily improved upon by making the strings stronger (for long strings) with a thicker silica layer or by bringing down the distance between the electrodes.

8.3.3 *Chains of PS Particles*

The method we used for the string formation is a general method and can be used to make strings from any type of colloids if they can be coated with another material to keep them together. To prove the generality of the technique we tried to build strings from PS particles and coated these PS particles with titania as described in Chapter 5. We applied an AC electric field to a dispersion of PS particles dispersed in a medium including a titania precursor and the stabilizer Lutensol ON 50. Reflection mode confocal microscopy images of the PS chains produced from PS particles with a size of 870 nm and coated with titania in the presence of an electric field are shown in Fig. 8.9. The reflection mode image was taken after the electric field was switched off.

The strings formed by the PS particles by seeded growth of titania together with the seeded growth of silica on the emulsion droplets and silica particles proves that coating in the presence of an electric field is a general approach to produce chains of beads.

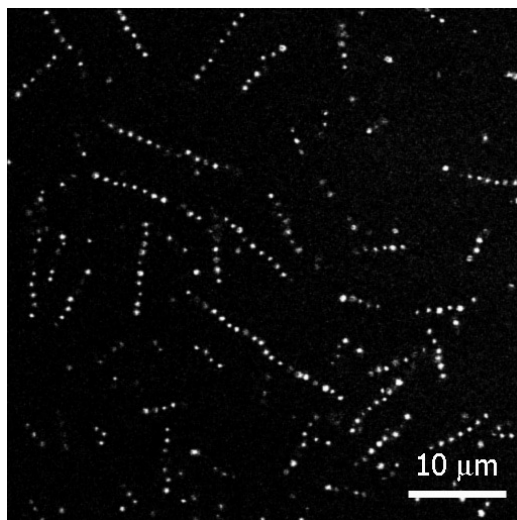


Figure 8.9: Reflection mode confocal microscopy images of chains of PS particles with a size of 870 nm and coated with titania in the presence of an electric field. Image size $54.13\mu\text{m} \times 54.13\mu\text{m}$.

8.4 Conclusions & outlook

We have described a general fabrication route for the 1D assembly of colloidal particles, which produces permanent strings of particles. We have demonstrated the procedure by performing seeded growth of silica and titania on silica, PS particles and emulsion droplets. Here the formation mechanism of the chains includes covalently connecting the particles to each other. This method offers a way of synthesizing anisotropic particles. Furthermore, permanent strings of colloids are interesting as a model system for studying anisotropic particles phase transitions and flexible strings can find use as simplified model system for (bio)polymers.

Acknowledgements

We thank Mirjam Leunissen for introducing us the fabrication of electric field cells and for useful discussions. Hanumantha Rao Vutukuri and Rob Kortschot are thanked for useful discussions. Peter van Oostrum is thanked for the optical tweezer experiments.

References

- [1] Gast, A.; Zukoski, C. *Adv. Colloid Interf. Sci.*, **1989**, *30*, 153.
- [2] Parthasarathy, M.; Klingenberg, D. *Mater. Sci. Eng.*, **1996**, *R17*, 57.
- [3] Kose, A.; Hachisu, S. *J. Colloid Interf. Sci.*, **1976**, *55*, 487.
- [4] Wen, W.; Weisbuch, C.; Phuong, D.; Lu, G.; Ge, W.; Chan, C.; Sheng, P. *Nanotechnology*, **2005**, *16*, 598.
- [5] Yethiraj, A.; van Blaaderen, A. *Nature*, **2003**, *421*, 513.
- [6] Dassanayake, U.; Fraden, S.; van Blaaderen, A. *J. Chem. Phys.*, **2000**, *112*, 3851.
- [7] Yethiraj, A.; Wouterse, A.; Groh, B.; van Blaaderen, A. *Phys. Rev. Lett.*, **2004**, *92*, 058301.
- [8] Yethiraj, A.; Thijssen, J.; Wouterse, A.; van Blaaderen, A. *Adv. Mater.*, **2004**, *16*, 596.
- [9] Tao, R.; Woestman, J.; Jaggi, N. *Appl. Phys. Lett.*, **1989**, *55*, 1844.
- [10] Tao, R.; Sun, J. *Phys. Rev. Lett.*, **1991**, *67*, 398.
- [11] Halsey, T.; Toor, W. *Phys. Rev. Lett.*, **1990**, *65*, 2820.
- [12] Toor, W.; Halsey, T. *Phys. Rev. A*, **1992**, *45*, 8617.
- [13] Klapp, S.; Forstmann, F. *Phys. Rev. E*, **1999**, *60*, 3183.
- [14] Tao, R.; Sun, J. *Phys. Rev. A*, **1991**, *44*, R6181 (1991).
- [15] Martin, J.; Anderson, R.; Tigges, C. *J. Chem. Phys.*, **1998**, *108*, 3765.
- [16] Martin, J.; Anderson, R.; Tigges, C. *J. Chem. Phys.*, **1999**, *110*, 4854.
- [17] Hynninen, A. P.; Dijkstra, M. *Phys. Rev. E*, **2005**, *72*, 051402.
- [18] B. Derjaguin, B.; Landau, L.; *Acta Physicochim. URRS*, **1941**, *14*, 633.
- [19] E. Verwey and J. Overbeek, *Theory of the Stability of Lyophobic Colloids*, Elsevier, New York, 1948.
- [20] J. Jackson, *Classical Electrodynamics*, Wiley, New York, third edition, 1999.
- [21] Hynninen, A. P.; Dijkstra, M. *Phys. Rev. E*, **2005**, *72*, 051402.
- [22] Cohen-Tannoudji, L.; Bertrand, E.; Bressy, L.; Goubault, C.; Baudry, J.; Klein, J.; Joanny, J. F.; Bibette, *Phys. Rev. Lett.*, **2005**, *94*, 038301.
- [23] Hermanson, K.D.; Lumsdon, S.O.; Williams, J. P.; Kaler, E.W.; Velev, O. D. *Science*, **2001**, *294*, 1082.
- [24] Salgueirino-Maceiraa, V.; Correa-Duarte, M. A.; Hucht, A.; Farle, M. *J. Magnetism and Magnetic Mater.*, **2006**, *303*, 163.
- [25] Tang, Z.; Kotov, N. A.; Giersig, M. *Science*, **2002**, *297*, 237.
- [26] Stöber, W.; Fink A.; Bohn, E. *J. Colloid Interface Sci.* **1968**, *26*, 62.
- [27] van Blaaderen, A.; Vrij, A. *Langmuir*, **1992**, *8*, 2921.
- [28] Zoldesi, C. I.; Imhof, A. *Adv. Mater.* **2005**, *17*, 924.
- [29] Zoldesi, C. I.; van Walree, C. A.; Imhof, A. *Langmuir*, **2006**, *22*, 4343.
- [30] Zoldesi, C. I.; Ivanovska, I. L.; Quilliet, C.; Wuite, G. J. L.; Imhof, A. *Phys. Rev. E*, **2008**, *78*, 051401.
- [31] Goodwin, J. W.; Ottewill, R. H.; Pelton, R. *Colloid Polym. Sci.* **1979**, *257*, 61.
- [32] Goller, M. I.; Obey, T. M.; Teare, D. O. H.; Vincent, B.; Wegener, M. R. *Colloids and Surfaces A*, **1997**, *123-124*, 183.

Selected Figures in Color

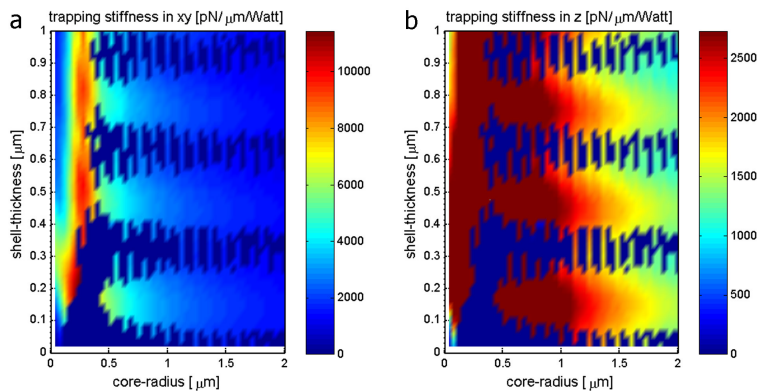


Figure 4.7 (a) Lateral trap stiffness and (b) axial trap stiffness as a function of particles diameter plotted against the diameter of the core diameter with an anatase-core, and an amorphous-titania-shell with the refractive indices of 2.3 and 1.8, respectively

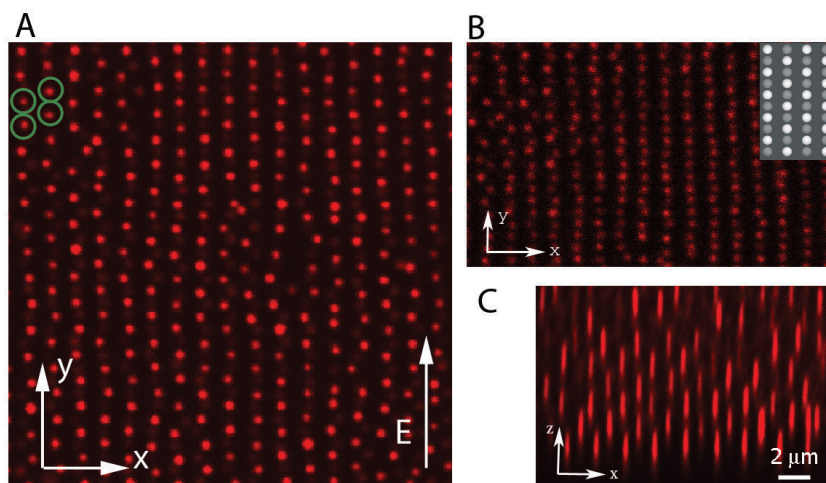


Figure 7.3 Confocal microscopy images of RITC labeled silica dumbbells in a crystal formed in an electric field of $177 \text{ V}_{\text{rms}}/\text{mm}$ with an aspect ratio of 0.9. (a) An image in the xy plane of the 3D stack, where dumbbells are oriented along the field and form a hexagonal pattern (110 plane), only fluorescent sphere centers of the dumbbells are visible. (b) An image of the same stack in the xy -plane clearly shows the bridge-site stacking of the crystal structure. Here 4 layers of the stack were superimposed and the inset shows two hexagonal planes of dumbbells that were overlaid, where white and gray spheres corresponds to dumbbell spheres of different hexagonal layers. (c) An image of the xz -plane where **aba** stacking is observed (001 plane). Image size (a) = $23.78 \mu\text{m} \times 23.78 \mu\text{m}$, (b) = $21.6 \mu\text{m} \times 13.2 \mu\text{m}$, (c) = $25.5 \mu\text{m} \times 8.5 \mu\text{m}$.

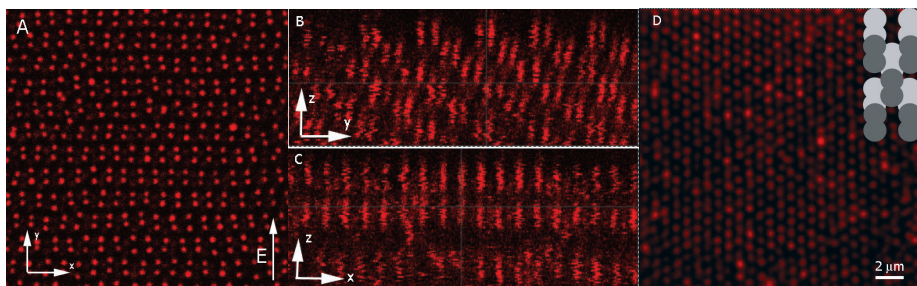


Figure 7.5 Confocal microscopy images of RITC labeled silica dumbbells with an aspect ratio of 0.7 in a 3D crystal formed with an electric field of $147 \text{ V}_{\text{rms}}/\text{mm}$. (a) An image of an xy plane out of the z -stack, where the dumbbells are oriented along the field and form a hexagonal pattern. (b) An image reconstructed from the same stack in the zy plane where the $abcdea$ stacking is visible. (c) A reconstructed image out of the same 3D stack in the xz plane where only the ada layers are visible, (d) an image made by projecting 8 layers in the xy plane, which is evidence for close-packing and the regularity of the crystal. The inset is the stacking of the hexagonal layers, where white and gray dumbbells show different layers. Image size (a) = $27.09 \mu\text{m} \times 27.09 \mu\text{m}$.

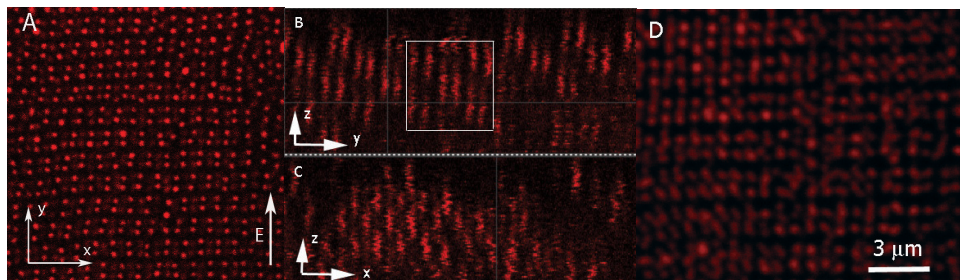


Figure 7.7 Confocal microscopy images of RITC labeled silica dumbbells with an aspect ratio of 0.7 in a crystal formed with an electric field of $234 \text{ V}_{\text{rms}}/\text{mm}$. (a) An image in the xy -plane of the 3D stack, where hexagonally ordered dumbbells oriented along the field are observed. (b) An image of the same stack in the yz -plane where the aba stacking is visible. (c) An image of in the xz -plane where aba layers are visible. (d) The 6 layers of the z -stack are superimposed on each other, implies that all the layers were on top of each other. Image size (a) = $25.05 \mu\text{m} \times 25.05 \mu\text{m}$.

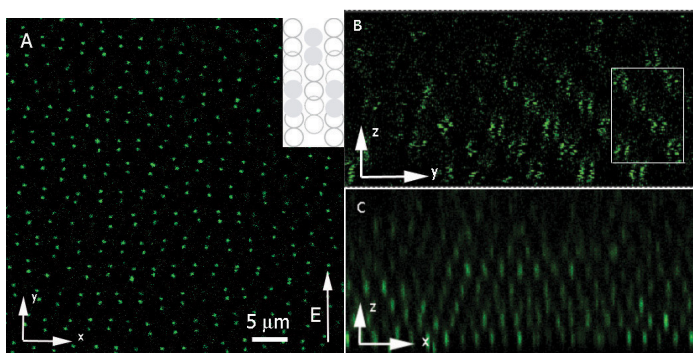


Figure 7.8 Confocal microscopy images of soft dumbbells, which formed a base-centered monoclinic crystal with $C2/m$ symmetry when an electric field of $106 \text{ V}_{\text{rms}}/\text{mm}$ (prefactor γ was 12 for a half of the dumbbell) was applied. (a) An image in the xy -plane scanned in sequence to build up a 3D stack. (b) An image in yz -plane

reconstructed from the 3D stack, the rectangular region outlines **abca** stacking of the crystal. (c) An image in xz -plane superimposed over 3 layers in this plane that shows the hexagonal order of the fluorescent cores of the dumbbells aligned along the field, which agrees with the proposed $C2/m$ symmetry of phase. Image size (a) = $46.80\mu\text{m} \times 46.80\mu\text{m}$

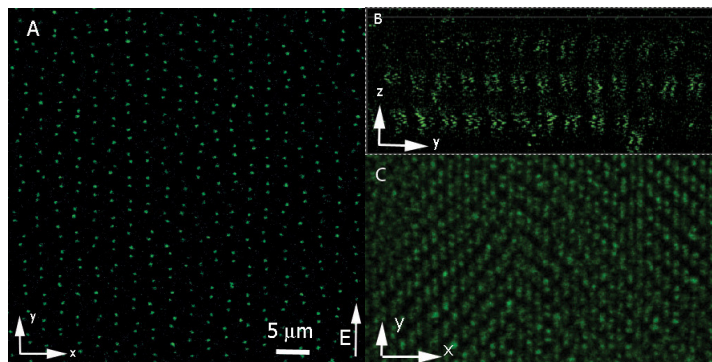


Figure 7.9 Confocal microscopy images of soft dumbbells, which form a base-centered monoclinic crystal phase with $C2/m$ symmetry when an electric field of $106 \text{ V}_{\text{rms}}/\text{mm}$ ($\gamma \approx 12$) was applied. (a) Image of an xy -plane scanned in sequence to build up a 3D stack, (b) an image in yz -plane reconstructed from the 3D stack, the square region outlines the **aa** stacking of the crystal, where **b** is not visible from this view, (c) an overlay of 5 xy layers, this image shows the stacking of the phase clearly. Image size (a) = $55.28\mu\text{m} \times 55.28\mu\text{m}$.

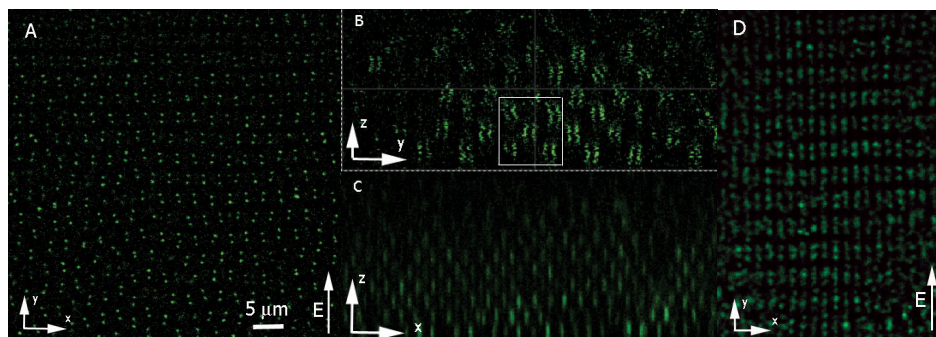


Figure 7.11 Confocal microscopy images of soft dumbbells, which form a bct crystal when an electric field of $200 \text{ V}_{\text{rms}}/\text{mm}$ ($\gamma \approx 45$) was applied. (a) Image of an xy -plane scanned in sequence to build up a 3D stack, (b) Image of an yz -plane reconstructed from the 3D stack, the square region outlines the **aba** stacking of the crystal. (c) An image of an xz -plane of the stack showing the hexagonal order of the dumbbells aligned along the field, which agrees with the proposed bct phase, (d) a projection of 6 layers in the xy -plane, this image shows the bridge-site stacking of a bct phase clearly. Image size (a) = $59.12\mu\text{m} \times 59.12\mu\text{m}$

Summary

In this thesis, we have presented the results of our synthesis and experimental investigations of a variety of colloidal systems. Colloidal particles are a hundred or thousand times larger than atoms or molecules, but suspended in a liquid they display the same phase behavior, including fluid, crystalline and glassy phases. This makes them excellent condensed matter model systems. In addition to this colloids as being building blocks of many objects in macro- world they are perfect to study the insights of matter. Besides the use of spherical colloids in today's technology and science anisotropic colloids are also increasing their importance and use in current scientific research. Several anisotropic particles systems are described here from synthesis to applications and phase behavior.

As a start, we highlighted in Chapter 2 the synthesis of eccentric titania core, silica shell particles. We showed that core-shell particles of titania with a silica shell yielded eccentric particles by extensive shrinkage of the core compared to the silica shell when calcined in an oven. on the way to synthesize the core-shell titania-silica particles we have also found that drying of the titania particles was crucial and not frying the particles left them porous, which gave us the possibility of synthesizing composite titania-silica particles. In the composite titania-silica particles we have found that silica was dispersed homogeneously in the particle, which shows the highly porous structure of titania prior to drying.

In Chapter 3 by using the knowledge we learned from Chapter 2 we showed a general method to synthesize perovskite particles based on titania. Porous titania particles prior to drying could adsorb the metal salts by simply sonicating these salts in a dispersion. We showed that stoichiometric addition of the metal salts followed by a calcination step resulted in monodisperse perovskite colloids of micrometer size, where the titania particles behave like a template for the colloidal perovskites. We also showed synthesis of metal core, perovskite shell particles, which could find applications in capacitors and finally we have shown the ease to manipulate these particles by addition of Pr salt for luminescence of the colloids.

In Chapter 4, we described the first seeded growth of titania particles starting with an anatase-titania core. Amorphous titania was coated on these crystalline spheres. We also described ways of tuning the refractive index of the amorphous titania shell by adding silica and calcination, which gave different refractive indices for different ways of manipulation. The actual aim of synthesizing these particles; their stiffer optical tweezing properties were also investigated and it was found that the core shell titania particles can be trapped twice stiffer than conventional same size polystyrene particles. We expect that these particles will find use for biophysical experiments where stiffer trapping is necessary.

Based on what we learned from Chapter 4 we managed to coat several other colloids with a titania shell. In Chapter 5 we describe a general method to coat sub-micron colloidal particles with titania as shown for silver, polystyrene, gibbsite and silica. Thickness of the titania coating with our method is easy to change

by changing the amount of the seeds and the titania precursor. We could tune the thickness from 15 nm to 250 nm for the polystyrene example, which is rare in literature. We also show ways for fabrication of titania shells by dissolving or burning the core.

In Chapter 6 & 7 phase behavior of silica dumbbells is explored. By dispersing the silica dumbbells in an organic solvent it is possible to change the particles interaction from hard to soft. Bringing in the soft interactions also enables us to explore the low aspect ratio region of dumbbells effectively, which is hard to produce synthetically. In Chapter 6 crystals of soft dumbbells are investigated with and without an external electric field. Effectively decreasing the aspect ratio of the dumbbells with soft interactions makes it possible to observe the plastic crystal of dumbbells predicted for aspect ratios lower than 0.4 by computation. In a plastic crystal of dumbbells particles are freely rotating whereas an external electric field aligns all the particles and brings orientational order along with positional order. Laser diffraction of these to systems with and without an electric field (crystalline with field and fluid-like with no field) shows that this soft dumbbells can find applications as a photonic switch, which turns on & off the photonic band gap with switching the electric field.

In Chapter 7 phase behavior of hard dumbbells are explored for two aspect ratios of 0.9 and 0.7 in the presence of an varying external electric field that aligns the particles and stimulates the crystallization. In addition to this phase behavior of soft dumbbells in an electric field was investigated and compared with the hard dumbbells system. Possible photonic properties of these crystal types are also discussed.

Finally in Chapter 8 synthesis of a new type of anisotropic particles was launched. In the presence of an electric field low volume fraction dispersions are known to form strings. Here we show the preliminary examples of permanently sticking these string particles to each other forming "chains of beads". The strings of silica particles was permanently stuck to each other by coating extra silica on them and similarly emulsion droplets were also coated with silica, which yielded a soft string of silica shells with elastic properties. Strings of polystyrene particles coated with titania was studied to extend the method.

Samenvatting

In dit proefschrift presenteren we de resultaten van onze syntheses en het experimentele onderzoek aan diverse colloïdale systemen. Colloïdale deeltjes zijn honderd tot duizend keer groter dan atomen of moleculen, maar gesuspenderd in een vloeistof vertonen ze toch hetzelfde fasegedrag. Zo vormen ze bijvoorbeeld vloeistoffen, kristallen en glazen. Ook zijn colloïden bouwstenen van vele objecten in de macro-wereld en daarom perfect geschikt om meer inzicht in de materie te verkrijgen. Naast het gebruik van bolvormige colloïden in de huidige technologie en wetenschap, worden anisotrope colloïden ook steeds belangrijker en meer gebruikt in het huidig wetenschappelijk onderzoek. Hier worden verschillende anisotrope deeltjes systemen beschreven van synthese tot toepassingen en fase gedrag.

We starten in Hoofdstuk 2 met de synthese van deeltjes met een excentrische titania kern en een silica schil. We tonen aan dat deze titania deeltjes met een silica schil excentrische deeltjes opleveren wanneer ze gecalcineerd worden in een oven; de kern krimpt dan sterk ten opzichte van de silica schil. Tijdens het werken aan de synthese van de kern-schil titania-silica deeltjes hebben we geconstateerd dat het drogen van de titania deeltjes cruciaal was: door ze niet te verhitten bleven de deeltjes poreus, wat ons de mogelijkheid gaf tot de synthese van composiet titania-silica deeltjes. Voor deze composiet titania-silica deeltjes hebben we geconstateerd dat silica homogeen in het deeltje verspreid was, waaruit de zeer poreuze structuur van titania voorafgaand aan het drogen blijkt.

In Hoofdstuk 3 beschrijven we een algemene methode voor de synthese van perovskiet deeltjes, gebaseerd op de kennis die we in Hoofdstuk 2 over titania verkregen hebben. Poreuze titania deeltjes kunnen metaalzouten adsorberen voordat ze gedroogd worden door simpelweg een dispersie met deze zouten te sonificeren. We tonen aan dat stoichiometrische toevoeging van metaalzouten, gevolgd door een calcinatiestap, resulteert in monodisperse perovskiet colloïden van micrometer grootte. Hierbij dienen de titania deeltjes als template voor de colloïdale perovskieten. We beschrijven ook de synthese van deeltjes met een metalen kern en een perovskiet schil, met toepassingen in condensatoren. Tot slot laten we zien hoe gemakkelijk deze deeltjes te manipuleren zijn door toevoeging van Pr zout voor luminescentie van de colloïden.

In Hoofdstuk 4 beschrijven we de eerste 'seeded growth' van titania deeltjes waarbij we met een anastase titania kern beginnen. Deze kristallijne titania kernen werden bedekt met amorf titania. We beschrijven ook manieren om de brekingsindex van de amorfe titania schil te beïnvloeden door silica toe te voegen en te calcineren, wat verschillende brekingsindices gaf voor verschillende manieren van manipulatie. Het doel van de synthese van deze deeltjes is de mogelijkheid ze vaster te klemmen met een optisch pincet. Het bleek dat de kern-schil titania deeltjes tweemaal vaster kunnen worden geklemd dan conventionele polystyreen deeltjes van dezelfde grootte. We verwachten dat deze deeltjes gebruikt zullen

worden in biofysische experimenten waar vaster klemmen met een optisch pincet nodig is.

Gebaseerd op wat we in Hoofdstuk 4 geleerd hebben zijn we erin geslaagd verschillende andere colloïden te bedekken met een titania schil. In Hoofdstuk 5 beschrijven we een algemene methode om sub-micron colloïdale deeltjes met titania te bedekken, zoals zilver, polystyreen, gibbsiet en silica deeltjes. De dikte van de titania laag in onze methode is gemakkelijk te in te stellen door de hoeveelheid kernen en de titania precursor nauwkeurig te kiezen. We kunnen de dikte van de schil variëren van 15 nm tot 250 nm voor polystyreen kernen, wat zeldzaam is in de literatuur. We laten ook manieren zien voor de fabricatie van titania schillen door de kern van de deeltjes op te lossen of te verbranden.

In Hoofdstuk 6 & 7 wordt het fasegedrag van silica dumbbells verkend. Door de silica dumbbells in een organisch oplosmiddel te suspenderen is het mogelijk om de interactie tussen de deeltjes te variëren van hard tot zacht. Het op deze manier induceren van zachte interacties geeft ons de mogelijkheid om de aspect ratio van de dumbbells te verkleinen, dergelijke deeltjes zijn moeilijk anders te produceren. In Hoofdstuk 6 zijn kristallen van zachte dumbbells onderzocht met en zonder een extern elektrisch veld. De effectieve verlaging van de aspect ratio van de dubbells door middel van zachte interacties maakte het mogelijk een plastisch kristal van dumbbells te observeren. Het plastisch kristal was door berekeningen voorspeld voor deeltjes met een aspect ratio lager dan 0.4. In een plastisch kristal van dumbbells draaien deeltjes vrij rond terwijl een extern elektrisch veld de deeltjes oplijnt en oriëntationele en positionele orde brengt. Laser diffractie aan deze systemen met en zonder elektrisch veld (kristallijn met veld en vloeïstofachtig zonder veld) laat zien dat deze zachte dumbbells toepassingen kunnen vinden als een fotonische schakelaar, die de fotonische band gap aan en uitzet door het elektrisch veld te schakelen.

In Hoofdstuk 7 wordt het fasegedrag van harde dumbbells verkend voor twee aspect ratio's, 0.9 en 0.7, in de aanwezigheid van een extern elektrisch veld dat de deeltjes oplijnt en kristalvorming stimuleert. Ook wordt het fasegedrag van zachte dumbbells in een elektrisch veld onderzocht en vergeleken met het harde dumbbells systeem. Mogelijke fotonische eigenschappen van deze kristaltypes worden ook behandeld.

Tot slot wordt in Hoofdstuk 8 de synthese van een nieuw type anisotrope deeltjes gelanceerd. In de aanwezigheid van een elektrisch veld vormen deeltjes in dispersies met lage volumefractie rijen. Hier tonen we de eerste voorbeelden van het permanent aan elkaar plakken van de deeltjes in deze rijen om "kralenkettingen" te vormen. De rijen van silica deeltjes werden permanent aan elkaar geplakt door een extra laagje silica om ze heen te groeien. Op dezelfde manier werden ook emulsiedruppels met silica bedekt, wat een zachte slinger van silica schilletjes met elastische eigenschappen opleverde. Om de methode uit te breiden zijn ook rijen van polystyreen deeltjes bedekt met titania bestudeerd.

Acknowledgement

There are many people who contributed directly or indirectly, to the work described in this thesis. I am grateful to all!

First of all, I want to thank my supervisor Arnout Imhof for offering me the opportunity to pursue my PhD degree, and giving me support and freedom in my research. Arnout, you were always ready for a discussion, thanks for many fruitful discussions, for your patience and guidance. My gratitude also goes to my promotor, Alfons van Blaaderen, for giving me the opportunity of working in a very stimulating atmosphere. Alfons, your support, suggestions and interest was one of the biggest drives of this thesis, thanks.

I would like to thank my nearby colleagues with whom I shared the room. Mirjam and Didi, from introducing a new land (life & scientific) to the discussions and chat, many thanks for everything that was a warm welcome for a new-comer out from the Mediterranean. Mirjam, thanks a lot also for introducing me the "confocal world" together with many others. Anke and Rao, thanks a lot for all the discussions and cosy environment that makes me a fan of 'OL018'. Rao, thanks for the support and suggestions that you made to my research. Anke, thanks for the corrections on the Dutch summary (or should I have said rewriting?)

During my PhD I have collaborated with people both form and outside of the SCM group. Especially I would like to thank Carlos van Kats for introducing me the synthesis of silica colloids and dumbbells. I would like to also thank Patrick Johnson for useful discussions on dumbbells. Our work together with Anita Jannasch came out to be a nice one, which I enjoyed a lot and this work also initiated an extra chapter than planned. Anita, dank für die nette Idee. I would like to thank all the present and former SCM members for making a pleasant environment at work, in conferences and at schools. Johan, thank you for your company in Florida. Stephane, Jamal, Alessandro, Linh, Peter, Matthieu, Gülşen, Peter, Esther, Michiel, Teun, Laura, Jacob, Eduardo, Chantal, Alejandro, Carmen, Christina, Slava, Andrea, Marjolein, Jos, Rene, Eelco, Bo, Frank, Ran, Joost, Jissy, Bart, Kristina thank you all for conversations, for breaks, cakes, cookies and everything else. Special thanks to Joost for his descriptive messages on the ingredients of the cakes, although this frequently kept me away from it.

Başlarken, desteğini bir an olsun bizden esirgemeyen aileme teşekkür bir borç. Öncelikle anneme ve babama bütün öncelikleri çocukları olduğu için ve yaptıkları sayısız fedakarlıklar için sonsuz teşekkürler ve minnet! Hakınız ödenmez ve bu satırlar size teşekkür etmeğe gerçekten yetmez. Hakan abime, Gülay ablama ve Gökhan'a da hayatımın her aşamasındaki sevgi ve destekleri için sonsuz teşekkürler. Yeğenlerim *Hasan Kemal*, *Gözde*, *Sümeyye* ve *Kemal'e* de bize neşe ve mutluluk getirdikleri için candan sevgiler ve teşekkürler.

Utrecht'teki son bir kaç senemizi güzelleştiren ve kolaylaştıran her konuda bize destek olan bütün herkese de sonsuz teşekkür. *Dank je wel allemal!*

Last but not least, I thank Nesibe for her endless support, understanding, pa-

tience, advice and for everything she has done and will do. Nesibe, you know it is hard to describe my gratitude to you...
Ahmet.

Curriculum Vitae

The author of this thesis was born on the 20th of May 1981 in Konya, Turkey. During his high school years he received a silver medal in national chemistry olympiads organized by National Science Foundation of Turkey. After finishing high school in 1999 (at Samanyolu Science High School, Ankara), he started his chemistry studies in September of that year at Bilkent University. In May 2003 he earned a Bachelor of Science degree and in August 2005 he received his Master of Science with distinction. Specialism for the master thesis was inorganic chemistry and materials science, with a thesis title of "Effects of Transition Metal Salts on the Synthesis of Mesoporous Silica". During master research he was supervised by Dr. Ömer Dağ. In October 2005, he joined the "Soft Condensed Matter" group of Prof. Alfons van Blaaderen at Utrecht University as a graduate student under the supervision of Arnout Imhof. Here, he investigated the applications and phase behavior of colloidal dumbbells and worked on synthesis of new functional colloidal particles, the results of which have been described in this thesis and in international peer-reviewed journals. He attended numerous schools and presented his results at international conferences. After finishing his PhD study he is going to stay in the "Soft Condensed Matter" group for a short post-doctoral study.

List of Publications

This thesis is partly based on the following publications:

- A.F. Demirörs, A. van Blaaderen & A. Imhof, Synthesis of Eccentric Titania-Silica Core-Shell and Composite Particles, *Chem. Mater.* 21,6, 979 (2009) - Chapter 2
- A.F. Demirörs & A. Imhof, BaTiO₃, SrTiO₃, CaTiO₃ and Ba_xSr_{1-x}TiO₃ particles: A General Approach for Colloidal Perovskites, *Chem. Mater.* 21, 13, 3002 (2009) - Chapter 3
- A. Jannasch, A.F. Demirörs, P.D.J. van Oostrum, A. van Blaaderen, A. Imhof & E. Schäffer, Anatase Core, Titania Shell Colloidal Particles for Optical Tweezing, in preparation - Chapter 4
- A.F. Demirörs, A. van Blaaderen & A. Imhof, A General Method to Coat Colloidal Particles with Titania, submitted - Chapter 5
- A.F. Demirörs, A. van Blaaderen & A. Imhof, Soft Colloidal Dumbbells and Realization of Plastic Crystals, in preparation - Chapter 6
- A.F. Demirörs, P. Johnsson, C. van Kats, A. van Blaaderen & A. Imhof, Phase Behavior of Colloidal Dumbbells in an Electric Field, in preparation - Chapter 7
- H.R. Vutukuri, A.F. Demirörs, A. Imhof & A. van Blaaderen, Chains of Colloidal Beads, in preparation - Chapter 8

Other publications:

- A.F. Demirörs, M. Arslan, Ö. Dağ, "The effect of anions of transition metal salts on the structure of modified mesostructured silica films" **Microporous and Mesoporous Materials**, 2007, 98, 249-257.
- F. Allegretti, M. Polcik, D. Sayago, F. Demirörs, S. O'Brien, G. Nisbet, C.L.A. Lamont and D.P. Woodruff, "Can circular dichroism in core level photoemission provide a spectral fingerprint of adsorbed chiral molecules?", **New Journal of Physics**, 2005, 7, 109.
- A.F. Demirörs, B.E. Eser and Ö. Dağ, "Liquid Crystalline Mesophases of Pluronic (L64, P65 and P123) and Transition Metal Salts", **Langmuir**, 2005, 21, 4156-4162.